Mechanics of Cellular Packing of Flexible Nanomaterials

by

Guijin Zou

B.Sc., Peking University; Beijing, P. R. China, 2013

A dissertation submitted in partial fulfillment of the

requirements for the Degree of Doctor of Philosophy

in the School of Engineering at Brown University

Providence, Rhode Island

February 2020

© Copyright 2020 by Guijin Zou

This dissertation by Guijin Zou is accepted in its present form

by the School of Engineering as satisfying the

dissertation requirement for the degree of Doctor of Philosophy.

Date_____ _____

Prof. Huajian Gao, Advisor

Recommended to the Graduate Council

Date_____ _____

Prof. Kyung-Suk Kim, Reader

Date_____ _____

Prof. Robert H. Hurt, Reader

Approved by the Graduate Council

Date_____ _____

Prof. Peter M. Weber

Dean of the Graduate School

Vita

Guijin Zou was born August, 1990 lunar calendar, in Yancheng, Jiangsu Province, P. R. China. He attended Peking University in 2009, and received the B.Sc. in Theoretical and Applied Mechanics from College of Engineering in 2013. Subsequently, he started his graduate study in the Solid Mechanics group at Brown University in the fall of 2013.

Acknowledgments

First of all, I would like to thank my advisor, Prof. Huajian Gao for his guidance and mentoring throughout all my years at Brown University. His support and patience made this wonderful journey possible, and his incredible passion in research, extensive knowledge, and deep physical insights have influenced me all the way from an undergraduate student to a researcher and will be beneficial to my entire future life. It's the best thing for me to be one of his students.

I am very grateful to the members of the dissertation committee, Prof. Kim and Prof. Hurt, for their valuable time to read my thesis. Prof. Kim is also a committee member of my preliminary examination and progress review. I learned a lot from his courses such as "*Linear elasticity*"; he has the magic to make things interesting, and it's always a pleasure to listen to his talks and courses. My sincere thanks also go to Prof. Hurt who has been a great collaborator of our group for the last decade. Part of my research in this thesis originates from the studies and discoveries which Prof. Hurt supervised. I am very honored and grateful to having him assess my Ph.D. thesis.

My research has benefited greatly from collaborations and conversations with many group members, post-docs and graduate students at Brown. Many thanks go to them, especially Dr. Xin Yi, Dr. Wenpeng Zhu, Dr. Woosoeng Kim and Dr. Fatemeh Ahmadpoor, who are now all professors around the world. I hope I will join them in the future.

I would also like to thank all of my friends at Brown, not only for their valuable advices and discussions on my research and study but also for being supportive all the time. They make me feel Brown is the home I belong to. Furthermore, I would like to express my thanks to all the faculty and staff at Brown, in particular the Solid Mechanics group.

Lastly, I want to thank my family, accomplishment of this thesis would not be possible without their support and encouragement.

Contents

List of Tables

List of Figures

Chapter 1

Introduction

1.1. Brief overview of cellular packing of nanomaterials

Decades of research have resulted in an ever increasing variety of engineering nanomaterials, such as one-dimensional nanotubes, nanofibers, nanowires and asbestos [1-3] and two-dimensional graphene, hexagonal boron nitride (h-BN), graphitic carbon nitride, and transition metal dichalcogenides (e.g., MoS_2 and WS_2) [3-5]. As nanomaterials are being actively explored in nanotechnology, biomedical applications and drug development, a fundamental understanding of cell-nanomaterial interactions is of essential importance to their potential toxicity and health risks [1, 6].

Packing of flexible fibrous nanomaterials within soft confinement such as vesicles and vesicular compartments is ubiquitous in biology, and an increasing number of studies have shown that cellular and intracellular packaging of nanomaterials play fundamental roles in many cellular functions and biological processes, including cell shape control [7-11], filopodial protrusion during cell movement [12] , mitotic cell division [13-15], frustrated phagocytosis [16], and cytotoxicity [2, 17, 18]. Experimental results indicate that length [1] and elasticity [17, 18] are important features that modulate the pathogenicity of encapsulated nanotubes or nanofibers. More specifically, exposing the mesothelial lining of the chest cavity to long multiwalled carbon nanotubes induces asbestos-like and length-dependent pathogenic behaviors, including frustrated phagocytosis and giant cell formation [16]. Sufficiently long and stiff carbon nanotubes within lysosomes cause sustained tip

contact with the inner lysosomal membrane, leading to lipid extraction, permeabilization, and eventually cell death, while biologically soft carbon nanotubes buckle within liposomes, consequently losing persistent tip contact and maintaining low pathogenicity [17]. Thin silver nanowires crumpled by endolysosomes have much lower toxicity, while thicker nanowires puncture the enclosing membrane and release silver ions and lysosome contents into the cytoplasm, thereby initiating oxidative stress [18].

As extensively demonstrated in one-dimensional carbon nanotube and silver nanowires, following uptake, nanomaterial behavior under confinement in intracellular vesicles plays a critical role in cytotoxicity [16-18]. For 2D materials, new packing morphologies and fundamentally different modes of interaction with intracellular vesicles are expected. Acquiring knowledge about these modes is an important step towards understanding specific biological responses to 2D materials [6]; however, only a few experiments and no systematic simulations or theoretical work, have been performed on this topic thus far. Experiments have shown that GO sheets of small lateral size (350 nm) remain in their initial flat shapes, while large lateral sized GO sheets (2 μm) form wrinkles and tend to fold in lysosomes [19].

Nanomaterials can directly interact with cell membranes and have the potential to be effective as novel antibiotics if they are capable of damaging the integrity of bacterial cell membranes [20-23]. Depending on their dimensionality, shape, size and polarity, reports have shown that packing or embedding of nanomaterials in cell membranes correlates with their lipid bilayer disruption and bactericidal abilities [23-25]. For example, experiments and molecular dynamics (MD) simulations have demonstrated that graphene and graphene oxide (GO) sheets can spontaneously pierce into cell membranes at sharp corners or edge

asperities [26], resulting in destructive lipid extraction and loss of membrane viability [23], which is the mechanism for graphene's cytotoxicity and antibacterial activity [20-22, 27] towards *Escherichia coli* (E. *coli*) [20-23]. All-atom simulations and experiments have described a class of synthetic retinoids with polar branch groups that prefer to enter and pack inside the bacterial lipid bilayers, thus leading to rapid killing of bacteria, even the non-growing, dormant "persister" subpopulations that exhibit high tolerance to antibiotics [28-30], by disrupting cell membranes [25]. The discoveries of membrane-active antibiotics have shed light on the treatment of challenging *Staphylococcus aureus* infections [24, 25]: however, in terms of therapeutic antimicrobial potential, the ability of nanomaterials to selectively target bacterial membranes is critical, and human or other mammalian cells have evolved to possess significantly different membrane compositions compared to bacterial cells [31, 32]; their different responses to nanomaterials make the selectivity theoretically possible, although it has been underexploited.

1.2. Thesis organization

In this thesis, we investigate the interactions between cell membranes and nanomaterials using multiscale (i.e., cellular-, membrane-, and molecular-scale) modeling and simulations, specifically focusing on the packaging problems of flexible nanomaterials in different biological environments, such as vesicles and lipid bilayers. This thesis consists of six chapters and is organized as follows.

Chapter 1 is an overview introduction about the interactions between cell membranes and nanomaterials; packing of flexible nanomaterials in vesicles and cell membranes is considered to have important biological implications for cytotoxicity and antimicrobial activity.

In chapter 2, we study how the geometrical and mechanical properties of a flexible nanofiber influence its encapsulation within a lipid vesicle. Molecular dynamics simulations and theoretical analysis indicate that packing morphology depends on the length and stiffness of the nanofibers, the initial configuration of the nanofiber-vesicle system and the pressure difference across the vesicle membrane. We establish a packing phase diagram based on three distinct vesicle morphologies.

In chapter 3, we focus on geometrical effects of rigid nanorods with finite and nonuniform diameters, including a cylindrical rod, a rod with widened ends, a cone-shaped rod and a screwdriver-shaped rod. We investigate the contact between the vesicle protrusion and the resulting axial contact force on the rod and find that they play important roles in regulating the vesicle tubulation and packing morphology.

In chapter 4, we consider cellular packing of flexible two-dimensional materials. We perform systematic molecular dynamics simulations and analysis to understand the packing of a flexible circular sheet in a spherical vesicle and the two-dimensional packing problem of a strip in a cylindrical vesicle. Phase diagrams of packing morphologies of encapsulated sheets are constructed based on a set of buckling analyses.

In chapter 5, we move to the molecular and membrane scale and investigate packing of a synthetic nanoagent in the lipid bilayers of different cell membranes. We perform all-atom molecular dynamics simulations and demonstrate that the selectivity of membrane-active nanoagents for bacterial membranes correlates with their abilities to penetrate and embed within bacterial-mimic lipid bilayers, but not within cholesterol-rich mammalian-mimic lipid bilayers.

Chapter 6 concludes the entire thesis with major scientific findings and future

perspectives.

Chapter 2

Packing of flexible nanofibers in vesicles

2.1 Introduction

Packing of flexible fibrous nanomaterials in a soft confinement such as vesicles and vesicular compartments is ubiquitous in biology and plays fundamental roles in many cellular functions. For example, the packing of cytoskeletal microtubules and actin filaments provides mechanical support and driving forces for cell movement, regulates cell shape and facilitates chromosome segregation in cell division [10, 33-36]. Packing of synthetic one-dimensional nanomaterials like carbon nanotubes in cells or subcellular organelles is found to be crucial to their cytotoxicity [16-18].

Experimental studies such as morphological transformation or evolution of liposomes [8-10, 36] and active nematic vesicles [37] induced by microtubules have demonstrated that the bending stiffness [36-38] and length [8, 9, 37, 39, 40] of an encapsulated nanofiber are two essential properties that regulate its packing within a vesicle. Representative morphologies of the nanofiber-vesicle system from these experiments can be categorized into four distinct groups based on the vesicle morphologies shown in the top row of Fig. 2.1. For example, the packing of a long and stiff nanofiber within a vesicle could give rise to a vesicle morphology resembling the Greek letter ϕ with a pair of tubular membrane protrusions (Fig. 2.1a) or to a cherry-shaped vesicle with a single tubular protrusion (Fig. 2.1b) [9]. For a nanofiber of length slightly larger than the diameter of a host vesicle, the vesicle assumes an axisymmetric lemon-like shape with a pair of protruding tips, where

the nanofiber makes almost no contact with the vesicle except at the two tips (Fig. 2.1c). In the case of a long and more flexible nanofiber, the vesicle could exhibit a non-axisymmetric dumpling-like shape with the nanofiber curved against the vesicle membrane (Fig. 2.1d,e) [38]. Morphologies similar to those in Fig. 2.1 have also been observed in the case of multiple flexible nanofibers within a vesicle [5, 6], and stiff nanofibers could in some rare cases lead to a coexistence of star-shaped vesicles with multiple tubular membrane protrusions [10, 11, 41].

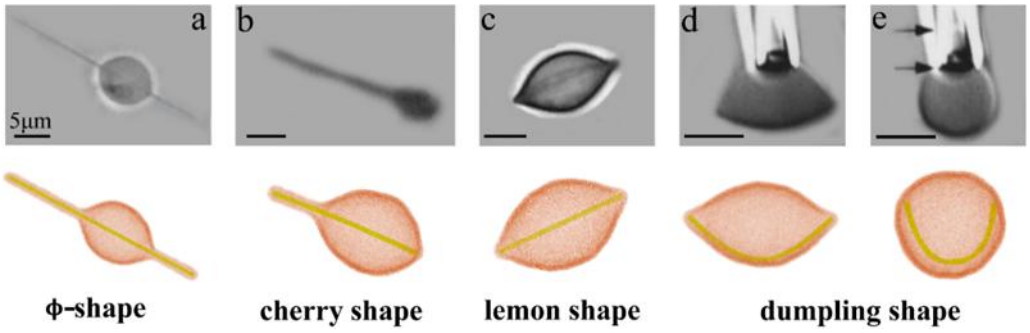

Figure 2.1. Experimental observation (upper row [9, 38]) and molecular dynamics simulation (lower row; the present work) of typical morphologies of a flexible nanofiber encapsulated within a vesicle: (a) a ϕ-shaped vesicle with a pair of tubular membrane protrusions enclosing a stiff nanofiber; (b) a cherry-shaped vesicle with a single tubular protrusion; (c) an axisymmetric lemon-shaped vesicle with a pair of protruding tips; (d) a protruding non-axisymmetric dumpling-shaped vesicle; (e) a non-protruding non-axisymmetric dumpling-shaped vesicle. In (d) and (e), the encapsulated nanofiber curves inside the vesicle against the membrane. Experimental pictures (scale bars = 5 μm) in (a-c) are reprinted with permission from [9] Copyright 1998 by the American Physical Society, and those in (d, e) reprinted with permission from [38] Copyright 1997 by the American Physical Society.

In spite of the mounting experimental observations on packing of nanofibers in vesicles, most theoretical models on this topic to date have been limited to axisymmetric configurations [42, 43] and scaling analysis [44], except for membrane wrapping of a rigid nanofiber at different entry angles [45, 46]. To elucidate the collective roles of nanofiber length and elasticity in the vesicle-nanofiber interaction, in this chapter, we report the first

and systematic coarse-grained molecular dynamics (CGMD) simulations and an extended theoretical analysis on the mechanical interplay between a spherical vesicle (with radius R and bending rigidity κ) and an encapsulated flexible nanofiber of length L and bending stiffness YI varying in a wide range of parameter values. At a given pressure difference Δp across the vesicle membrane, it is shown that the packing morphogenesis is governed by two dimensionless parameters: the length ratio L/R and normalized bending stiffness $YI/(\kappa R)$, if there is no adhesive interaction between the nanofiber and vesicle. It will also be shown that the initial configuration of the nanofiber-vesicle system and the pressure difference across the membrane play important roles in regulating the packing morphology.

2.2 Model and methods

2.2.1 Modeling of lipids

In our CGMD simulations, the lipid bilayer of the vesicle is composed of solvent-free lipid molecules [47, 48], each modeled as three connected beads, one bead representing the hydrophilic head and two the hydrophobic tail (see Fig. 2.2). The bead-bead interactions are described by the following potentials:

$$U_{\mathrm{WCA}}(r) = 4\varepsilon\left[\left(\frac{\sigma'}{r}\right)^{12} - \left(\frac{\sigma'}{r}\right)^{6} + \frac{1}{4}\right] \ (0 < r < r_{\mathrm{cut}}),$$

$$U_{\mathrm{COS}}(r) = \begin{cases} -\varepsilon + U_{\mathrm{WCA}}(r) \ \ (0 < r < r_{\mathrm{cut}}) \\ -\varepsilon \cos^2\left[\dfrac{\pi(r - r_{\mathrm{cut}})}{2w}\right] \ (r_{\mathrm{cut}} < r < r_{\mathrm{cut}} + w) \end{cases},$$

$$U_{\mathrm{FENE}}(r) = -\frac{1}{2} k_{\mathrm{FENE}} r_{\infty}^2 \ln\left(1 - \frac{r^2}{r_{\infty}^2}\right) \ (0 < r < r_{\infty}),$$

$$U_{\mathrm{harmonic}}(r) = \frac{1}{2} k_{\mathrm{harmonic}} \left(r - r_0\right)^2,$$

where $r_{cut}=2^{1/6}\sigma$', ε and σ (σ'=$\alpha\sigma$) are the energy well depth and bead diameter, respectively. The bead diameter σ is set at 1 nm, in order to construct a lipid bilayer with an appropriate membrane thickness and areal density (area per lipid).

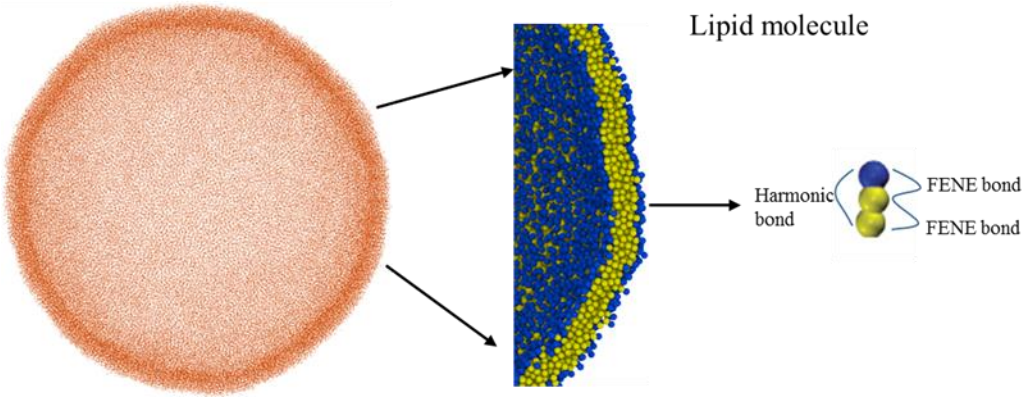

Figure. 2.2. Structure of lipid molecules in the bilayer membrane with their inter-particle bonding topology.

To ensure the mechanical properties of the lipid membrane falling in a range measured experimentally [49, 50], we chose ε as 0.56 kcal mol^{-1}, and the unit thermal energy is k_BT=1.1ε (T=310 K) [17, 45, 47, 48]. The nearest neighbor beads in each lipid molecule are connected by FENE bonds with k_{FENE} = 30ε = 16.8 kcal mol^{-1}nm^{-2} and r_∞=1.5σ=1.5 nm. The head bead is also connected to the second tail bead by a harmonic bond with a rest length r_0 =4σ=4 nm and force constant $k_{harmonic}$=10ε=5.6 kcal mol^{-1} nm^{-2} (see Fig. 2.2). The non-bonded interaction parameters between two beads of the nanofiber, lipid heads and tails are detailed in Table 2.1.

Table 2.1 Parameters of non-bonded interactions

bead type	bead type	interaction	parameters
lipid head	lipid head	WCA	α=0.95
lipid head	lipid tail	WCA	α=0.95
lipid tail	lipid tail	COS	α=0.95, w=1.6σ
nanofiber	lipid head/tail	WCA	α=0.95
nanofiber	nanofiber	WCA	α=0.95

2.2.2 Modeling of a flexible nanofiber

Flexible nanofibers were constructed by folding a two-dimensional triangular lattice (Fig. 2.3a) into a tubular structure. The nearest and second nearest neighbor beads are connected by harmonic bonds with stiffness k_{harmonic}, with the rest length between two nearest beads of 1.3σ, and that between second nearest beads of 2.2σ. The constructed nanofibers have different lengths (110 nm-220 nm) but the same radius 2.2 nm, as shown in Fig. 2.3b for a selected length of L=155 nm. CGMD simulations were performed to compress a selected nanofiber, and the measured force-displacement relation, as shown in Fig. 1.3d for L=155 nm, gives the critical buckling force F_c, from which the bending stiffness can be calculated as

$$YI = \frac{F_c L^2}{4\pi^2} \ .$$

The dimensionless bending stiffness of the nanofiber $YI/\kappa R$ is determined from

$$\frac{YI}{\kappa R} = \frac{F_c L^2}{4\pi^2 \kappa R} \ ,$$

where R is the vesicle radius, κ is the bending rigidity of the membrane. As shown in Fig. 2.3e, our simulations at different fiber lengths (L=155 nm, 175 nm, 195 nm) indicate that the dimensionless bending stiffness $YI/(\kappa R)$ and bond stiffness of the nanofiber $k_{\text{harmonic}}/\varepsilon$ obey an approximately linear relationship as

$$\frac{YI}{\kappa R} = 0.25 \frac{k_{\text{harmonic}}}{\varepsilon} \ .$$

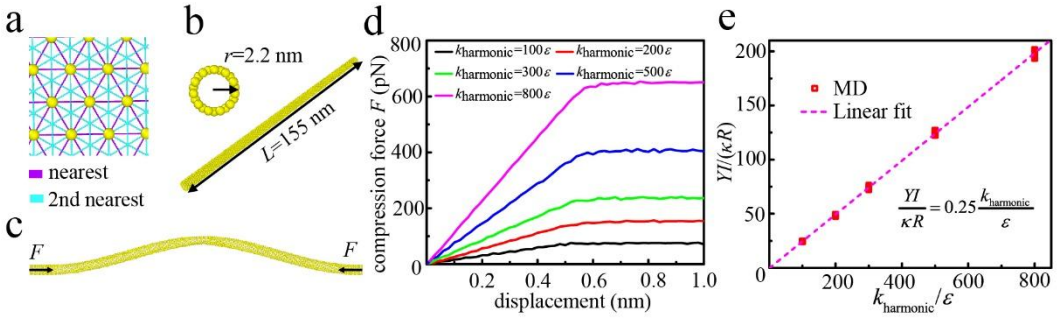

Figure. 2.3. Modeling of a flexible nanofiber in CGMD simulations. (a) A two-dimensional triangular lattice structure with nearest and second nearest beads connected by harmonic bonds. (b) The nanofiber formed by folding the triangular lattice. (c) Schematic of a selected nanofiber under compression. (d) Force-displacement curves obtained from the compression test at different bond stiffness k_{harmonic}. (e) Relation between $YI/(\kappa R)$ and $k_{\text{harmonic}}/\varepsilon$.

The bending energy of a uniformly curved nanofiber in CGMD simulations is proportional to the square of its curvature as shown in Fig. 2.4.

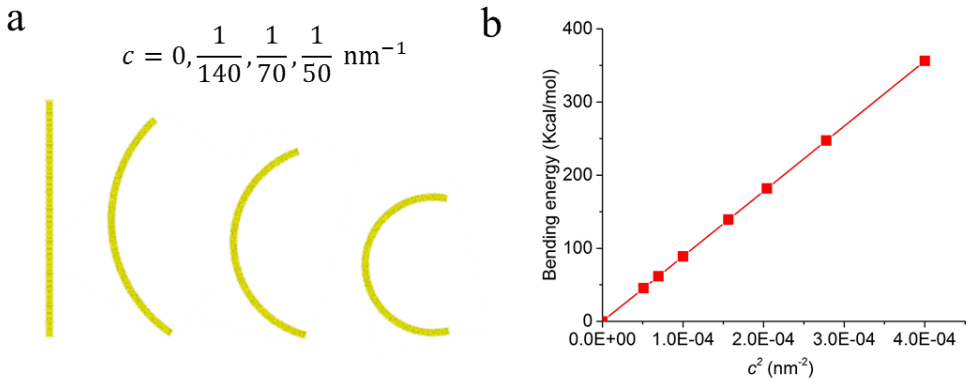

Figure 2.4. (a) Representative configurations of a nanofiber with constant curvature. (b) Bending energy of the curved nanofiber is linearly proportional on the square of its curvature c. The nanofiber length is L = 200 nm, and the harmonic force constant is k_{harmonic} = 100ε.

2.2.3 Modeling of vesicle-nanofiber system

The vesicle is initially a sphere of radius R=50 nm (Fig. 2.2), consisting of around 5×10^4 lipid molecules. A pressure difference across the lipid membrane is maintained by imposing outward forces on lipid heads in the bilayer along the director of the lipid

molecules [17]. Other simulation setups are similar to other studies in reference [17, 45].

The free energy of the system is written as

$$E = \frac{\kappa}{2}\int (c_1 + c_2)^2 \, \mathrm{d}A + \frac{YI}{2}\int_0^L \left|\partial^2 \mathbf{r} / \partial s^2\right|^2 \mathrm{d}s - \Delta p(V - V_0) \ ,$$

where the first term represents the bending energy of the membrane according to the Helfrich membrane theory, κ being the bending rigidity of the membrane, and c_1, c_2, and dA the two principal curvatures and surface element of the membrane surface, respectively; the second term is the bending energy of the flexible nanofiber parameterized as an inextensible curve $r=r(s)$ with Y, I, s, and L being the Young's modulus, moment of inertia, arclength, and total contour length of the nanofiber, respectively; the third term corresponds to the work associated with a pressure difference Δp between the interior and exterior of the vesicle due to osmolarity change or aspiration, V and V_0 denoting the volume of the vesicle in the current and initial states. Previous theoretical analysis and MD simulations of this coarse-grained lipid model indicate that the Helfrich membrane theory is applicable for the bending deformation of the lipid membrane down to a radius of curvature comparable to the bilayer thickness [51]. In this study, we neglect the stretching of the membrane and nanofiber as well as the associated stretching energies. Accordingly, in our theoretical analysis, we assume area conservation of the vesicle membrane by introducing a Lagrange multiplier conjugated to the vesicle area. Expressing the free energy function in the following dimensionless form

$$\frac{E}{\kappa} = f\left(\frac{L}{R}, \frac{YI}{\kappa R}, \frac{\Delta p R^3}{\kappa}\right)$$

suggests that the problem under consideration is governed by three dimensionless parameters, the length ratio L/R, the normalized fiber stiffness $YI/(\kappa R)$, and the normalized

pressure $\Delta pR^3/\kappa$. The bending stiffness YI measures the flexibility of the nanofiber.

Our CGMD simulations were performed at a pressure difference of $\Delta p=100\kappa/R^3\approx 40$ kPa unless specified otherwise. The membrane bending rigidity was taken as $\kappa=11.7\ k_BT$ [51] ($1\ k_BT=4.3\times10^{-21}$ J). This setup corresponds to a lysosome of diameter 0.5 μm under an osmotic pressure of 300 Pa according to a theoretical analysis [17]. A constant ambient temperature of 310 K was maintained via the Nose-Hoover thermostat [52, 53], and the time step was fixed at 100 fs. The simulations were carried out based on the software package LAMMPS [54].

2.3 Results

2.3.1 Morphological evolution of an encapsulated flexible nanofiber inside a vesicle

We first simulated a rigid nanofiber of length L inside a vesicle of radius R, with L/R varying from 2.2 to 5.1 to get equilibrium vesicle morphologies. After equilibrium, a 100 ns simulation for each length was performed to obtain the average confinement force. The simulation results showed that the confinement force at the two ends of the nanofiber and the packing morphologies are consistent with a recent theoretical study [17] on a rigid nanofiber inside an axisymmetric vesicle shown in Fig. 2.5a. At a given L, the minimum energy state of the vesicle, the confinement force F conjugated to the nanofiber length, and the membrane tension Σ conjugated to the fixed vesicle area can be obtained following a numerical optimization technique [17, 43]. The theoretical analysis revealed that the confinement force F first increases almost linearly as L increases, peaks at certain L/R, and then levels off to a constant upon the formation of a tubular membrane protrusion, resembling a similar structure called membrane tether [55, 56]. Near the peak value of F, the vesicle adopts a lemon-like shape with two protruding tips (Fig. 2.5a). The peak

confinement force from the simulations occurs at L/R = 3.2, with a value around F_{max} = 96κ/R (Fig. 2.5a), higher than the theoretical prediction. This difference could be due to the effect of thermal fluctuations that are not included in the theoretical analysis.

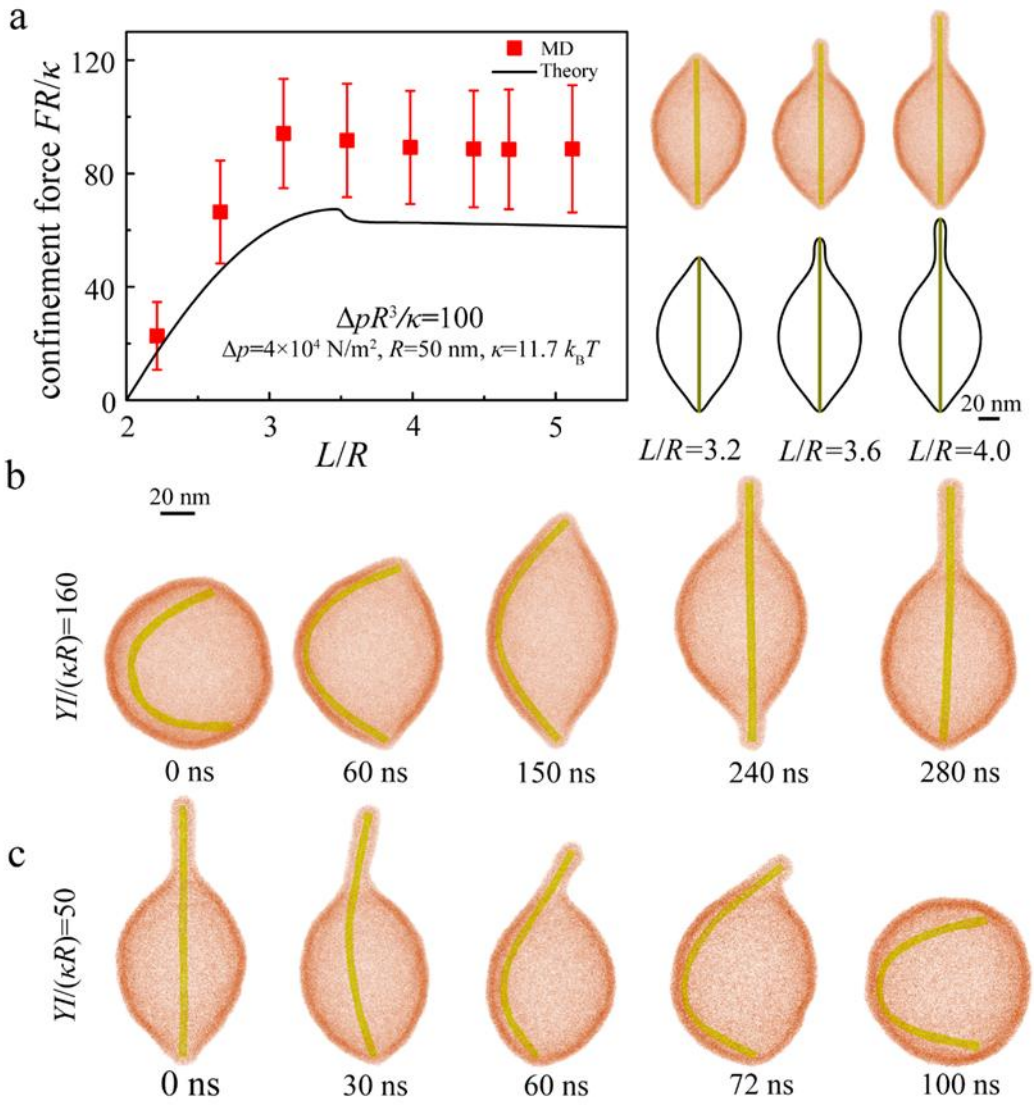

Figure. 2.5. (a) Confinement force and vesicle morphology induced by an encapsulated rigid nanofiber of length L. Error bars of the MD simulation results are standard deviations of 100 ns average of the calculated confinement force. (b,c) Time sequences of CGMD simulations showing morphological evolution of the nanofiber-vesicle system. (b) Straightening of an initially curved nanofiber of bending stiffness YI = 160κR, and (c) buckling of an initially straight nanofiber of YI = 50κR inside their confining vesicles. The nanofiber length in both cases is L = 4R.

For an encapsulated nanofiber with length $L = 4R$ and bending stiffness $YI = 160\kappa R$, both ends are free to move and rotate, as indicated in Fig. 2.5b. Therefore, the critical force for Euler buckling satisfying the simply supported boundary conditions is

$$F_c = \pi^2 YI/L^2 = 98.7\kappa/R,$$

which is larger than the peak confinement force ($F_{max} = 96\kappa/R$). Therefore, this nanofiber should prefer to be straight and the vesicle would adopt a cherry-like shape in equilibrium. This is confirmed by our CGMD simulation that an initially curved nanofiber with these properties will return to the straight configuration (Fig. 2.5b). During the simulation, the vesicle evolves from its initial spherical shape first to a protruding non-axisymmetric dumpling-like shape with nanofiber gradually straightening out, then to a ϕ shape of up-down symmetry with two short tubular protrusions wrapping around the straightened nanofiber, and finally to a cherry-like shape with only one longer tubular protrusion wrapping around one tip of the nanofiber. In this process, the release of elastic bending energy in the nanofiber is compensated by the deformation of the vesicle. The vesicle shape transition from ϕ to cherry-like is consistent with numerical analysis and experimental observations, indicating that the ϕ-shaped vesicle is of slightly higher elastic energy compared to the cherry-shaped vesicle [7, 9, 17]. Experiments also showed that adhesive binding between nanofiber and membrane could stabilize a ϕ-shaped vesicle [8].

Next we consider a more flexible nanofiber with length $L = 4R$ and bending stiffness $YI = 50\kappa R$, in which case $F_c = 30.8\kappa/R$ is significantly lower than the peak confinement force $F_{max} = 96\kappa/R$. At the beginning of the simulation, an initially straight nanofiber with these properties is confined in a cherry-shaped vesicle (Fig. 2.5c). As expected, the nanofiber is buckled by the confinement force and the vesicle evolves towards a sphere

with gradually diminishing protrusion. Eventually, the vesicle adopts the spherical shape and the nanofiber becomes curved and fully packed inside the spherical vesicle (Fig. 2.5c). In this process, we note that the portion of the nanofiber within the shrinking membrane protrusion remains nearly straight and the curved nanofiber in tight contact with the vesicle membrane.

2.3.2. Effects of initial configuration on packing

The sequences of morphological evolution from two different initial configurations described above suggest that the nanofiber packing may depend on the initial system configuration. To understand this, we performed additional CGMD simulations on vesicular packing of nanofibers with lengths and bending stiffnesses varying over a wide range of parameter values, starting at two initial configurations: (1) an initially strongly curved nanofiber packed in a spherical vesicle (Fig. 2.6), and (2) an initially straight nanofiber in a cherry-shaped vesicle (Fig. 2.7). We do not consider nanofibers with length smaller than $2R$ as they simply undergo random Brownian motion inside the vesicle.

2.3.2.1. Packing phase diagram of an initially curved nanofiber

For packing of an initially curved nanofiber (Fig. 2.5b), our CGMD simulations revealed three types of equilibrium packing morphologies shown in Fig. 2.6a. Fig. 2.5a indicates that a vesicle encapsulating a rigid nanofiber would adopt a lemon-like shape before the confinement force F peaks around L/R=3.2, suggesting that L/R=3.2 represents an upper limit for the morphological phase of a lemon-shaped vesicle even for a flexible nanofiber as long as it is not pressed against the vesicle membrane along its length (Fig. 2.7). As shown in Figs. 2.6b and 2.7, packing of a nanofiber with length larger than $2R$ and smaller than $3.2R$ leads to a lemon-shaped vesicle. The same conclusion is valid for packing

of an initially straight nanofiber (Fig. 2.8b). In other words, the lemon-shape region of the phase diagram is independent of the initial geometry of the nanofiber (Fig. 2.7). For a nanofiber of length larger than 3.2*R*, the vesicle would adopt either a dumpling-like shape or cherry-like shape. A longer nanofiber requires a larger bending stiffness to be able to deform the vesicle into a cherry-like shape (Fig. 2.6b). As shown in Fig. 2.5a, the peak confinement force on the nanofiber is around $96\kappa/R$ at $\Delta p = 100\kappa/R^3$. It is found that the simulated phase boundary between the dumpling and cherry configurations is in good agreement with Euler's theory which predicts buckling occurs when (dashed line in Fig. 2.6b).

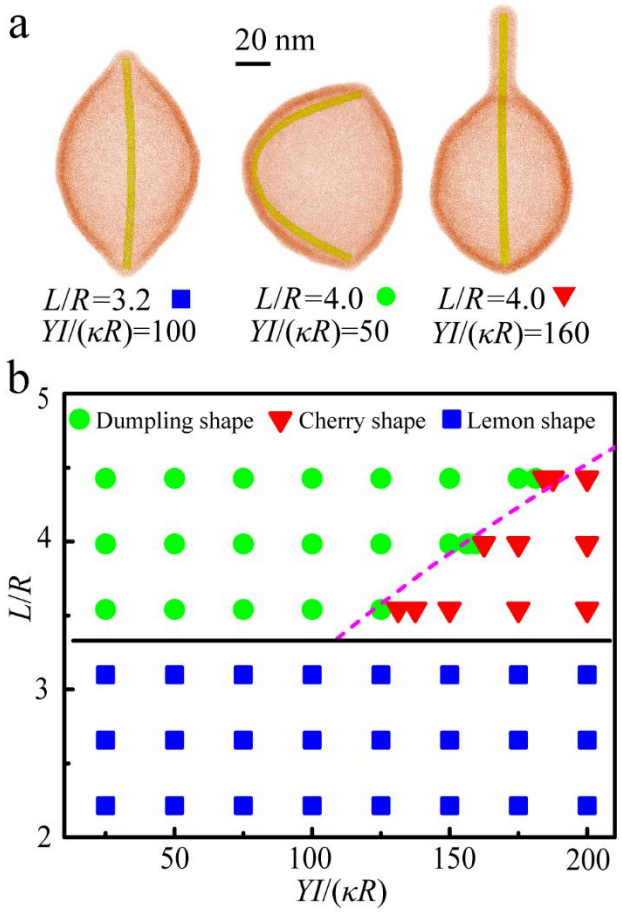

Figure 2.6. Packing phase diagram for an initially curved flexible nanofiber inside a spherical vesicle. (a) The equilibrium packing morphologies and (b) packing phase diagram in terms of nanofiber length

and bending stiffness. The dashed line is the predicted phase boundary from the classical Euler's buckling theory.

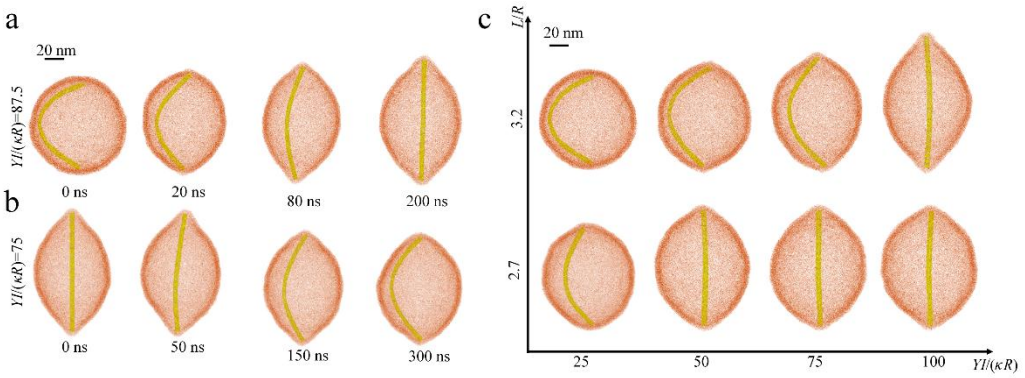

Figure 2.7. Morphologies of lemon-shaped vesicles. Time sequences of CGMD simulations showing the morphological evolution of a vesicle encapsulating a flexible nanofiber of $L = 3.2R$. (a) An initially curved, relatively stiff nanofiber (YI=87.5κR), and (b) an initially straight more flexible (YI=75κR) nanofiber within a vesicle. (c) Representative packing morphologies of a vesicle encapsulating a flexible nanofiber of length $L = 2.7R$ and $3.2R$ and stiffness YI=25κR, 50κR, 75κR, and 100κR.

2.3.2.2. Packing phase diagram of an initially straight nanofiber

For packing of an initially straight nanofiber within a cherry-shaped vesicle, we expect that a sufficiently soft and long nanofiber would buckle under the confinement force from the vesicle. For a nanofiber with length larger than $3.2R$, the vesicle could buckle the nanofiber into a curved shape, with itself evolving to a dumpling-like shape (Fig. 2.8a). The packing phase diagram (Fig. 2.8b) looks quite different from that for an initially curved nanofiber (Fig. 2.6). The difference could be attributed to the stabilizing effect of the initial tubular membrane protrusion against buckling [57]. Our CGMD simulations generally show that the portion of nanofiber enclosed by the tubular membrane protrusion tends to stay straight. This confinement makes the effective length of the nanofiber for buckling less than its total length. In the case of an extremely long fiber, the effective length for buckling is only on the order of the free portion of the nanofiber not covered by membrane

[38]. An interesting biological phenomenon that can be related to this finding is that the filopodia could display a length on the order of tens of μm [58], which is much larger than the predicted limiting length of 1 μm - 2 μm from the Euler theory [59, 60].

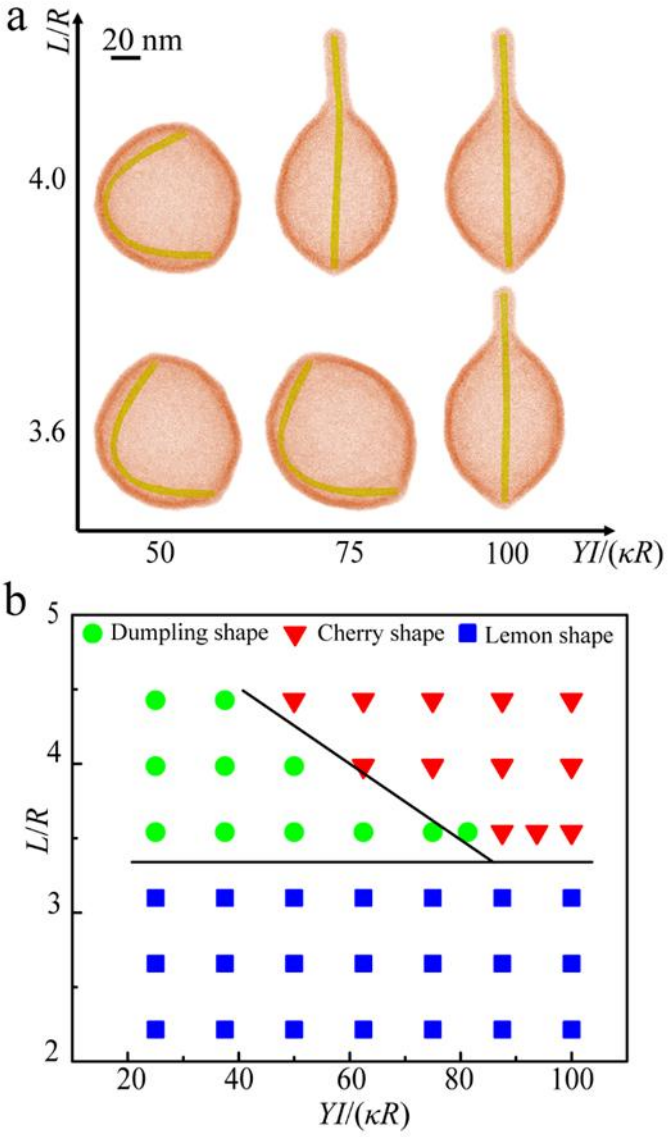

Figure 2.8. Packing phase diagram for an initially straight flexible nanofiber inside a cherry-shaped vesicle. (a) Representative packing morphologies and (b) packing phase diagram in terms of nanofiber length and bending stiffness.

2.3.3. Effects of pressure on packing morphology

In the above analysis, the pressure difference between the interior and exterior of the vesicle was taken to be $\Delta p = 100\kappa/R^3$. To investigate how the pressure difference affects nanofiber packing, we performed a theoretical analysis on the packing of a rigid nanofiber and some case studies of MD simulations on the vesicle-nanofiber interaction with nanofiber of fixed length $L=4R$ and stiffness $YI=130\kappa R$ at $\Delta p = 100\kappa/R^3$, $130\kappa/R^3$ and $156\kappa/R^3$ (Fig. 2.9). The theoretical results in Fig. 2.9a indicate that both the confinement force F and the membrane tension Σ increase as Δp increases. Note that the peak values of F and Σ are not located at the same L/R at a given Δp. The monotonically increasing relationship between Δp and F is reflected in our MD simulations. As Δp increases, the vesicular confinement force F increases, which results in the buckling and folding of an initially straight encapsulated nanofiber inside the vesicle; meanwhile, the vesicle evolves from a cherry-like shape to a dumpling-like shape (Fig. 2.9b). A similar phenomenon has been observed in experiments where a long straight microtubule encapsulated in a vesicle subject to increasing suction from a micropipette undergoes buckling and snaps into a curved shape within the vesicle [38]. From a localized point of view, the above phenomenon can be described in other words as follows. At a low Δp or equivalent low membrane tension, the microtubule within the vesicle pushes the vesicle membrane vertically and induces a tubular membrane protrusion; while at a high Δp or large membrane tension, the microtubule buckles into a strongly curved structure attaching parallel to the membrane. This tension-regulated interaction behavior is consistent with our previous theoretical work on the membrane wrapping of one-dimensional nanotubes, in which we found that the nanotube adopts a near-perpendicular mode of cell entry at a small membrane tension; while at a sufficiently large membrane tension, the nanotube exhibits a

near-parallel configuration with respect to the cell membrane [46].

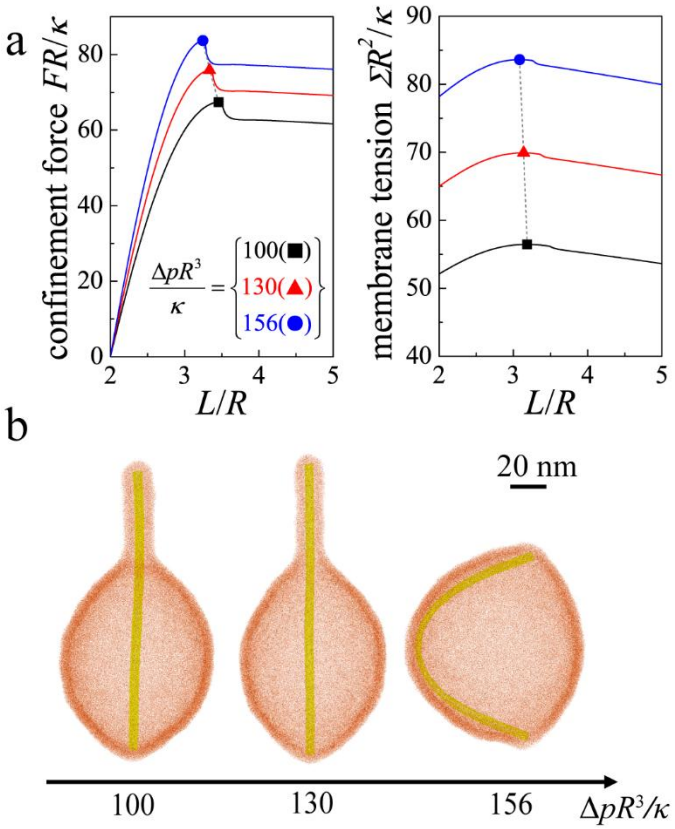

Figure 2.9. Buckling of an encapsulated nanofiber at increasing pressure difference across the vesicle membrane. (a) Confinement force F and membrane tension Σ as functions of L/R at different Δp. The (grey) dashed lines indicate the relationship between the peak values (symbols) of F and Σ and the corresponding length ratio L/R. (b) Packing morphologies for an encapsulated flexible nanofiber of $L=4R$ and $YI=130\kappa R$ at different pressure differences $\Delta p = 100\kappa/R^3$, $130\kappa/R^3$ and $156\kappa/R^3$.

2.4 Discussion

A single microtubule has a persistence length of several millimeters (~6 mm) [38], much larger than the typical diameter of biomimetic liposomes (1 μm-10 μm), corresponding to the dimensionless stiffness $YI/(\kappa R)$=120-1200 with YI=6 mm· k_BT, R=0.5 μm-5 μm and κ =11.7 k_BT. According to our phase diagrams (Figs. 2.6b and 2.8b), we could anticipate the lemon-, cherry- or ϕ-like shape for encapsulated microtubule bundles

in liposomes, consistent with experimental observation [9]. Actin filaments, which are more flexible than microtubules, have a persistence length of 9 μm-18 μm [61, 62], corresponding to $YI/(\kappa R)$=0.1-3. From our CGMD simulations, a single actin filament is insufficient to overcome the membrane elastic resistance, and only actin bundles might be able to cause membrane protrusion resembling filopodia, as indicated in experiments [63]. Experiments on the organization of microtubules within vesicles show that increasing the bending rigidity κ of the vesicle membrane could drive the vesicle to transform from a cherry-like shape to a dumpling-like shape [36], which is consistent with our phase diagrams as $YI/(\kappa R)$ decreases with an increasing κ.

Besides the ϕ- and cherry-like shapes, a vesicle encapsulating a long rigid nanofiber could also display dumbbell- or pearl-like shapes, though they are extremely rare due to their high deformation energy [9]. In the present work, we focus on the case of $YI/(Rk_BT)>>1$ and L/R on the order of 1, in which the nanofiber within the vesicle behaves like an elastic rod and the entropic contribution to the nanofiber flexibility can be ignored. At $YI/(Rk_BT)>1$, the nanofiber within the vesicle would behave like a semiflexible polymer such as DNA strands, and a careful investigation on its mechanical interaction with the vesicle should take account the interplay of the elastic energy and thermal fluctuation of the system [64]. In the case of an encapsulated worm-like polymer chain with a contour length several times the circumference of the spherical vesicle ($L>>R$), the polymer chain undergoes a transition from an isotropic disordered random conformation to an ordered toroidal coil as its bending stiffness increases [65]. The coiling of confined long nanofibers has been observed in both engineering and biological circumstances including controllable coiling of gold nanowires within polymer capsules [66], filamentous morphology in

bacteria [67], actin polymerization inside cell-sized droplets [68]. It is of significance to take a comprehensive study on packing of nanofibers with length varying in a wide range from L/R=2 to L/R on an order of 10 and rigidity from a persistence length on the order of tens of nanometers to several millimeters.

In this study we assume that the adhesive interaction between the nanofiber and vesicle membrane is negligible. In this case the cherry-like shape for the vesicle encapsulating a long stiff microtubule is slightly energetically favorable compared to the ϕ shape [7, 9, 17], and the energy difference is on the order of tens of k_BT [17]. As the energy difference is not significant, the binding or the friction between the bounding lipid membrane and the enclosed portion of the nanofiber could facilitate the ϕ shape though it might be an energetically metastable state. Introduction of microtubule-associated proteins (MAPs) could establish direct links or increase friction between the microtubule and vesicle membrane, and stabilize the ϕ shape, as indicated by experiments [8]. Moreover, it remains unveiled whether a vesicle of the cherry-like shape has a lower free energy than the ϕ shape in the presence of adhesion between the nanofiber and vesicle. Another intriguing phenomenon is the (super-) coiling and buckling of ring-like fibers or bundles confined in a vesicle [8, 11, 40, 68, 69]. Different from the coiling of open nanofibers, ring-like filaments could fold and coil but unlikely possess sharp ends that might induce membrane protrusion like stiff nanofibers do. Besides their (adhesive) interaction with the membrane, it would be challenging to explore how packing depends on the adhesion or friction between adjacent fibers in the bundle or adjacent segments in the coiling of ring-like structures.

In the three morphological phases considered in this work, the flexible nanofibers

display three distinct modes of mechanical interplay with the vesicle membrane, which are shallow punch against membrane in the lemon phase, nanofiber buckling and bending away along the vesicle surface in the dumpling phase, and formation of a long tubular membrane protrusion in the cherry phase. Similar interaction modes have also been observed in the interplay between a flexible nanofiber and a membrane patch [70]. Theoretical analysis on the dynamics of a growing flexible fiber approaching a fluctuating membrane indicates three regimes: fiber stalling when the fiber growth stops with a precursor structure of the membrane protrusion, fiber runaway in which the fiber bends away from the membrane, and formation of tubular membrane spicules [70].

A single long stiff nanofiber within the vesicle could results in a tubular membrane protrusion as indicated in experiments [9, 36, 38] and our theoretical analysis and CGMD simulations (Fig. 2.5). For a vesicle encapsulating multiple stiff nanofibers of a radial pattern, the vesicle could display a star-like shape with multiple tubular membrane protrusions [10, 11, 41]. The scaling dependence of $YI/\kappa R$ suggests that increasing the membrane bending rigidity κ is mechanically equivalent to decreasing the bending stiffness of the confined nanofiber and implies a vesicle shape transition from a cherry-like shape to a lemon- or dumpling-like shape based on our phase diagrams (Figs. 2.6 and 2.8). This argument is supported by the self-organization of microtubules within vesicles of tunable bending stiffness κ [36]. By increasing the cholesterol content from 5% to 50%, the membrane bending stiffness κ increases from around 25 k_BT to 150 k_BT [71]. In this process, the microtubule bundle upon the increasing confinement force splits and forms a racket-like structure consisting of multiple microtubules with partially buckled portions, and each microtubule gradually evolves to a more curved state bent against the vesicle membrane;

in the meantime, the vesicle transforms from an initially cherry-like shape, to a transitional lemon-like shape, and eventually to a dumpling-like shape [36].

2.5 Conclusion

Packing of a flexible nanofiber inside a vesicle is governed by the interplay between elastic deformation of the nanofiber and vesicle. In this study, we have performed the first coarse-grained molecular dynamics simulations to probe the phase diagram of packing in terms of the normalized nanofiber length and bending stiffness, as well as the effect of pressure difference between the interior and the exterior of the vesicle. It is found that the packing depends on not only the geometrical and material properties of the encapsulated nanofiber but also its initial configuration in the vesicle confinement. Based on the morphology of the vesicle in equilibrium, three distinct types of morphological packing phases (lemon, dumpling, and cherry) were found from the simulations, where the cherry-like vesicle shape exhibits a single tubular membrane protrusion. As the nanofiber length or bending stiffness decreases, the cherry-shaped vesicle tends to transform to an axisymmetric lemon shape or a protruding non-axisymmetric dumpling shape or a non-protruding non-axisymmetric dumpling shape. Packing phase diagrams with respect to the normalized nanofiber length and bending stiffness were determined. Further simulations demonstrated that increased pressure difference could buckle the nanofiber within the vesicle. Our results also shed lights on the importance of the mechanical interplay between the nanofiber and cell membrane to understand cell shape control.

Chapter 3

Packing of nanorods with finite and non-uniform diameters in vesicles

3.1 Introduction

Understanding the biophysical mechanisms for cellular and intracellular packaging of one-dimensional materials is of fundamental importance for many cellular functions and biological processes, including cell shape control [7-11], filopodial protrusion during cell movement [12], mitotic cell division [13-15], frustrated phagocytosis [16], and cytotoxicity [17, 18]. For example, long and stiff microtubule bundles within a vesicle could give rise to tubulation of the vesicle resembling the Greek letter ϕ with a pair of tubular membrane protrusions or a cherry-like shape with a single protrusion [7-10], while encapsulated long flexible filaments become curved against the vesicle membrane and the vesicle adopts a non-axisymmetric dumpling-like shape [39, 72]. Flexible ring-like filaments could fold into a (super-) coiled structure within a cell and lead to complex cell deformation [10, 11]. Elongation of spindle microtubules within cell nucleus due to gene overexpression could result in abnormal tubulation of the nuclear envelope during mitosis [13]. Sister chromatids which become separated at the cell poles during anaphase are connected by thin microtubule bundles, and together form a dumbbell-like structure in the cell [15].

In the field of pathogenicity, the need to assess the health safety of synthetic one-dimensional nanomaterials, such as carbon nanotubes, nanofibers, and asbestos, prior to widespread commercial use is calling for a systematic effort to understand the biophysical

mechanisms of their interactions with cells and intracellular organelles following cell uptake [1, 16-18]. Experimental results indicate that length [1] and elasticity[17] are important features that modulate the pathogenicity of encapsulated nanotubes. More specifically, long and stiff carbon nanotubes could induce lung injury, epithelioid granuloma, persistent interstitial inflammation and fibrosis, frustrated phagocytosis, and organelle damage [1, 16, 17, 73]. Exposing the mesothelial lining of the chest cavity to long multiwalled carbon nanotubes induces asbestos-like and length-dependent pathogenic behaviors, including frustrated phagocytosis and giant cell formation [16]. Sufficiently long and stiff carbon nanotubes within lysosomes cause sustained tip contact with the inner lysosomal membrane, leading to lipid extraction, permeabilization, cathepsin B release into the cytoplasm, and eventually cell death, while biologically soft carbon nanotubes buckle within liposomes, consequently losing persistent tip contact and staying nonpathogenic [17].

While a number of theoretical models have been established to understand and characterize the mechanical response of a vesicle to a confined rigid nanorod of different lengths [7, 9, 17, 43], two key parameters, nanorod diameter and shape, have been neglected in these previous studies, where the vesicle was oversimplified as having point contact with a nanorod that exerts a pair of localized outward pushing forces upon the vesicle poles. Similar approaches have been employed in modeling the formation of tubular membrane protrusions induced by external forces [74-77] induced by, for example, cooperative movement of motor proteins [78, 79] or optical/magnetic tweezers [75, 76], and introducing a spontaneous membrane curvature could also result in tubulation [80].

In view of the accumulating experimental observations on cellular packing of nanorods

with finite and non-uniform diameters, in this chapter, we study a more sophisticated model that explicitly accounts for contact between the membrane of a vesicle and side wall of an encapsulated nanorod with more complex and general geometries. Four different nanorod shapes are considered (Fig. 3.1): a cylindrical nanorod, a nanorod with two wide ends, a cone-shaped nanorod, and a screwdriver-shaped nanorod. Here the cylindrical nanorod serves as a representative for one-dimensional nanomaterials including (carbon) nanotubes, (gold) nanowires, (asbestos) nanofibers, microtubule bundles, and actin-based cellular protrusions of tubular shapes; the nanorod with two wide ends models dumbbell-like structures observed in mitotic cell division and engineered nanodumbbells used in biomedical imaging [81, 82] and photodynamic therapy [83]; the cone-shaped nanorod could be used to depict carbon nanohorns which exhibit potential applications in drug delivery [84, 85] and show low cytotoxicity at a low-uptake level [86] but at high doses induce lysosomal membrane permeabilization and subsequent release of lysosomal proteases, eventually leading to cell apoptosis [87, 88]; the screwdriver-shaped nanorod of a sharp diameter variation can be viewed as a modified hybrid of the cylindrical nanorod and cone-shaped nanorod. Molecular dynamics simulations and theoretical analysis are systematically performed to probe how the morphology and other mechanical behaviors of a vesicle are regulated by encapsulated rigid nanorods of different diameters and shapes. It will be shown that an initially spherical vesicle undergoes significant shape transformations that strongly depend on the nanorod length, shape, and diameter. Moreover, the effective axial contact force on the nanorod exerted by the confining vesicle exhibits rich features of nonlinearity and nonmonotonicity. Our results shed light on the biophysical mechanisms for the cellular or intracellular packaging of microtubule bundles, mitotic cell division, as

well as the pathogenicity of carbon nanotubes.

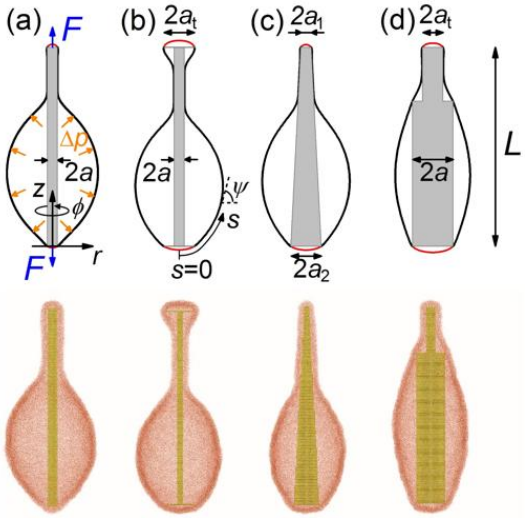

Figure 3.1. Schematics and snapshots from molecular dynamics simulations of the tubulation of a vesicle induced by an encapsulated rigid nanorod at a pressure difference Δp, (r, ϕ, z) being the adopted cylindrical coordinate system. The vesicle-nanorod morphologies for (a) a cylindrical nanorod of a uniform radius a, (b) a cylindrical nanorod with two widened tip ends of radii at, (c) a cone-shaped nanorod, and (d) a screwdriver-shaped nanorod. The encapsulated nanorod has length $L = 4R$.

3.2 Model and methods

CGMD simulations are performed to investigate the roles of nanorod size and shape on the vesicle-nanorod interaction. We use the same lipid bilayer model as described in Chapter 2. Different shapes of the nanorods were constructed by deleting the corresponding redundant beads from the cylindrical nanorods. Fig. 3.2a shows selected nanorods of different sizes and shapes. The vesicle in our MD simulations is chosen initially as a sphere of radius R=50 nm and the lateral dimensions of the simulation box are 160 nm×160 nm. To avoid membrane rupture due to membrane tension while still capturing the mechanical interplay between the nanorod and vesicle, the outward forces are taken as 1.95×10^{-3} kcal mol^{-1} nm^{-1} on each lipid in our CG model, which corresponds to a pressure difference Δp

around 40 kPa or a dimensionless pressure of $\Delta pR^3/\kappa = 100$, as opposed to $\Delta pR^3/\kappa = 400$ assumed in the following theoretical analysis. The canonical (NVT) ensemble is used in the simulations which are performed based on LAMMPS [54] at a constant temperature of 310 K under the Nose-Hoover thermostat [52, 53]. We focus on the equilibrium morphology and axial contact force of the vesicle-nanorod system.

To illustrate how the encapsulated nanorod is created in the modeling, here, we take the cylindrical nanorod as an example. A short nanorod consisting of two equal parts, each of length 20 nm, was first put at the center of a vesicle of radius 50 nm. Then these two parts were pulled slowly in opposite directions at a constant speed (1 m/s) in the simulations. Eventually the intermediate trajectory (Fig. 3.2b) was obtained and used to create the initial model of the encapsulated nanorod by replacing these two separated parts with a single nanorod (Fig. 3.2c). Encapsulated nanorods of non-uniform diameters are built following a similar scheme. With the initial system configurations shown in Fig. 3.2c for nanorods of different sizes, the CGMD simulations were performed under a constant ambient temperature with a time step fixed at 100 fs. The encapsulated nanorod was fixed while the vesicle membrane was allowed to move freely during simulations. After equilibrium is reached, a 100 ns simulation is performed and we split the nanorod into two parts (as demonstrated in Fig. 3.2d) to calculate the axial contact force. As the nanorod is fixed, the axial contact force on each nanorod part equals to the balancing force on the interface (dashed line in Fig. 3.2d) between the two nanorod regions which is determined and recorded by LAMMPS. Fig. 3.2e shows the time evolution of the axial contact force and the corresponding averaged value in the case of a uniform nanorod at $a/R = 0.2$ and $L/R = 4.2$ from MD simulations.

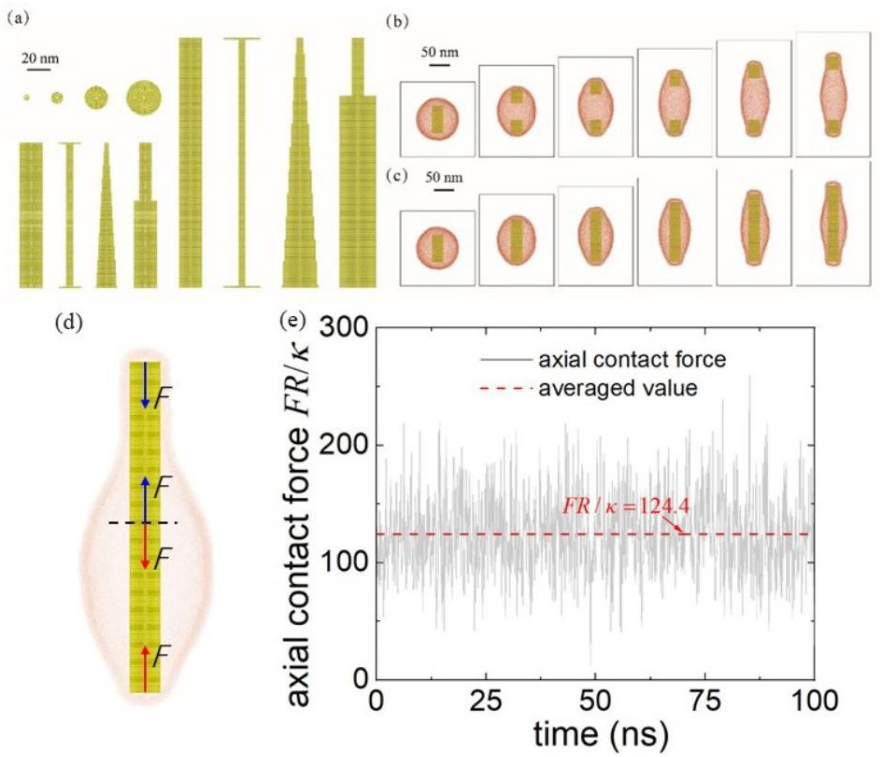

Figure 3.2 (a) Selected examples of coarse-grained model of nanorods of different sizes and shapes. (b) Time sequences of a pulling simulation scheme. (c) The initial system configurations of vesicles encapsulating cylindrical nanorods of different lengths. (d) The equilibrium configuration used to determine the axial contact force. (e) Time evolution of the axial contact force and the corresponding averaged value in the case of a uniform nanorod $a/R = 0.2$ and $L/R = 4.2$ from MD simulations.

We also consider a theoretical model in which the deformed vesicle is of a fixed surface area $A(=4\pi R^2)$ at a pressure difference Δp with a protrusion induced by the nanorod with length $L \geq 2R$ (Fig. 3.1). The deformed vesicle is assumed to retain an axisymmetric configuration according to our MD simulations. The free energy of the system is described by the Helfrich functional [89],

$$E = \pi\kappa \int_0^l \left(\frac{\mathrm{d}\psi}{\mathrm{d}s} + \frac{\sin\psi}{r} \right)^2 r\mathrm{d}s - \Delta p(V - V_0) ,$$

where the first term is the elastic deformation energy of the vesicle with ψ, s, and κ being the tangent angle, arclength, and bending rigidity of the vesicle membrane, respectively; l

denotes the undetermined total arclength of the vesicle; $V_0 = 4\pi R^3/3$ and $V = \pi\int_0^l r^2 ds$ are the original and deformed volume of the vesicle under Δp. It is assumed that the membrane has no spontaneous curvature. The membrane deformation energy associated with the Gaussian modulus is constant due to the Gauss-Bonnet theorem and hence ignored here. In addition to the free energy of the system, there are two other key quantities characterizing the mechanical state of the vesicle: the effective membrane tension σ as a Lagrange multiplier conjugated to the fixed vesicle area A, and the effective axial contact force F between the nanorod and vesicle membrane, stretching the vesicle along the z-axis in our adopted cylindrical coordinate system.

The minimum energy state of the vesicle at each given L is numerically determined through the interior-point method in constrained nonlinear optimization [90]. Once the state of the minimum energy E is obtained, the corresponding vesicle shape and effective membrane tension σ as a Lagrange multiplier are known. The effective axial contact force F as a conformational force arising from the vesicle deformation is determined numerically from $F = dE/dL$.

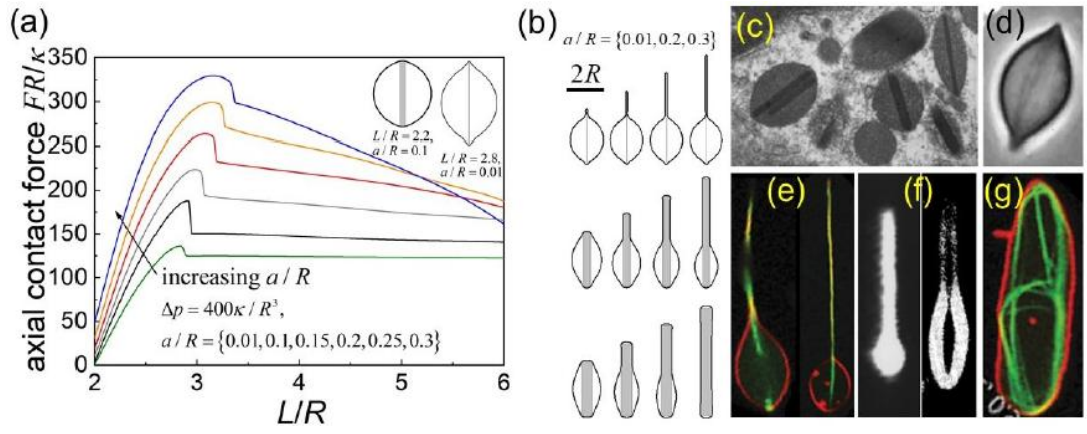

Figure 3.3. (a) Normalized tip contact force FR/κ as a function of the normalized nanorod length L/R at $\Delta pR^3/\kappa = 400$ and different values of the normalized nanorod radius a/R. At extremely small a/R (e.g.,

a/R=0.01), *F* saturates to a nearly constant value upon membrane protrusion formation. (b) Selected vesicle morphologies induced by the encapsulated rigid nanofiber of radius *a/R* = 0.01, 0.2 and 0.3, and length *L/R* =3, 4, 5 and 6. The scale bar is of length 2*R*. Inset in (a) showed the enlarged vesicle shape at *L/R* = 2.2, *a/R* = 0.1 and at *L/R* = 2.8, *a/R* = 0.01. (c-g) Experimental images of the observed vesicle morphologies induced by one-dimensional nanomaterials of different radii, lengths, and structures. (c) Lysosomes containing stiff single-walled carbon nanotubes in a cell from the mice ileum. Reprinted with permission from ref. [91]. Copyright 2010, Elsevier, Ltd. (d) A lemon-shaped vesicle with a pair of protruding tips. Reprinted with permission from ref. [9]. Copyright 1998, the American Physical Society. (e) Cherry-shaped vesicles, each with a single tubular membrane protrusion enclosing a stiff long microtubule. (f) A vesicle encapsulating a thick nanorod exhibiting a bowling pin-like shape. Left subfigure is reprinted with permission from ref. [7]. Copyright 1998, the Physical Society of Japan. Right subfigure is reprinted with permission from ref. [8]. Copyright 1998, Elsevier, Ltd. (g) A vesicle containing a cage-shaped actin network exhibits a thick, rod-like shape. Both (e) and (g) are reprinted with permission from ref. [10]. Copyright 2015, the Royal Society of Chemistry.

3.3 Results and discussion

We first investigate the case of a vesicle containing a straight, rigid, cylindrical rod of length $L/R > 2$. Figs. 3.3a and 3.4a show that the effective tip contact force F first increases almost linearly with the nanorod length L, rises to a peak value and then decreases upon the formation of a tubular membrane protrusion. The force variation is accompanied by a transformation of the vesicle shape (Figs. 3.3b and 3.4b). At extremely small a/R (e.g., $a/R = 0.01$), curve of F exhibits indistinguishable differences from those due to a pair of point forces on the vesicle poles, as expected, and the vesicle transforms from an initial sphere to a lemon-like shape with a pair of protruding tips, and to a cherry-like shape with a thin, long tubular membrane protrusion and a relatively large bulge (Figs. 3.3b and 3.4b). As a/R increases, the sizes of the two protruding tips and the tubular protrusion increase, the lemon-like shape gradually becomes a conga drum-like shape, and the cherry-like shape becomes a bowling pin-like shape with a tubular membrane protrusion with radial size

comparable to that of the bulge. For large *a/R* and *L/R* (e.g., *a/R* = 0.3 and *L/R* = 6), the vesicle exhibits a rod-like shape enclosing the nanorod (Figs. 3.3b and 3.4b). Due to the finite size of the nanorod, the vesicle is deformed at *L/R* = 2 with non-zero axial contact force *F* (Figs. 3.3a and 3.4a).

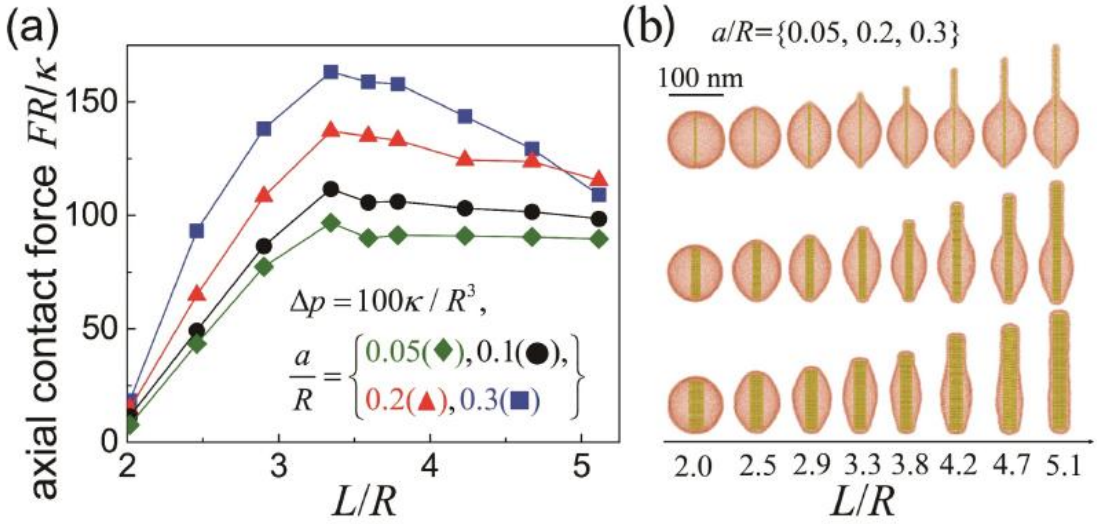

Figure 3.4. (a) Axial contact force and (b) vesicle morphology induced by a nanorod of length *L* and radius *a*, as determined from MD simulations.

The modeling predicted morphologies of vesicles containing nanorods of different sizes are consistent with experimental observations for a wide range of cell activities. In treating Alzheimer disease, single-walled carbon nanotubes (SWCNTs) with precisely controlled doses preferentially enter lysosomes as pharmacological targets in neurons and neurites, and serve as drug carriers to deliver preloaded acetylcholine [91]. It is demonstrated that lysosomes containing SWCNTs of intermediate lengths exhibit lemon-like shapes, as shown in Fig. 3.3c [91], though the mechanisms responsible for a SWCNT-based neuroprotective approach for Alzheimer disease remain elusive [91, 92]. Lemon-shaped vesicles with a pair of more evident protruding tips are observed as the microtubule polymerizes within a phospholipid vesicle (Fig. 3.3d) [9]. Our modeling analysis indicates

that a vesicle containing a stiff, thin, long nanorod exhibits a cherry-like shape, or a bowling pin-like shape for a thick, long nanorod. As shown in Fig. 3.3e, liposomes encapsulating thin, long actin-fascin bundles do exhibit cherry-like shapes [10], and liposomes encapsulating long, thick microtubule bundles of different *L/R* exhibit bowling pin-like shapes (Fig. 3.3f) [7, 8]. In the case of a cage-shaped actin network, which can be approximated as a thick rod (Fig. 3.3g), the confining liposome exhibits a rod-like shape. These experimental observations are all consistent with our theoretical results and MD simulations.

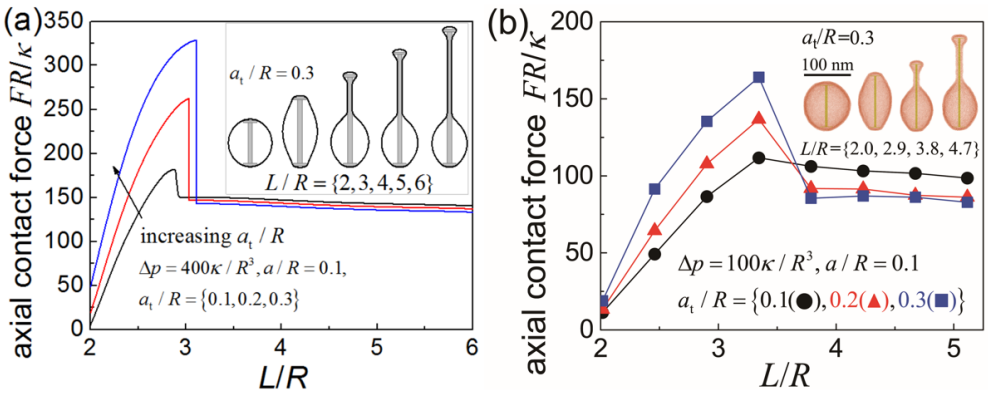

Figure 3.5 Normalized axial contact force FR/κ as a function of the normalized nanorod length L/R for a/R = 0.1 and different tip sizes a_t/R = 0.1, 0.2 and 0.3. (a) Theoretical results at $\Delta p = 400R^3/\kappa$; (b) MD simulations at $\Delta p = 100R^3/\kappa$. Insets plot vesicle morphologies induced by an encapsulated rigid nanorod with radius a_t/R = 0.3 at selected lengths.

To investigate whether and how the nanorod tip size affects the morphology of a confining vesicle, we perform a number of case studies with both theoretical analysis and MD simulations on the interaction between the vesicle and an encapsulated nanorod with two widened tips, as shown in the inset in Fig. 3.5. In our theoretical analysis, the tip thickness is assumed to be negligible, and in the MD simulations, the tip contains only one layer of coarse-grained beads. Fig. 3.5 shows that the axial contact force *F* increases as the

tip radius at increases before the formation of the tubular protrusion and then levels off to a constant. The nanorod with a wider tip requires a larger length L to overcome a larger axial contact force F for vesicle tubulation. The rising portions of the force curves for a_t/R = 0.1, 0.2, 0.3 in Fig. 3.5 overlap those for a/R = 0.1, 0.2, 0.3 in Figs. 3.3 and 3.4. This is because the vesicle before tubulation has no contact with the rod wall and only senses the tip size of the nanorod in the pre-tubulation stage. A key feature of Fig. 3.5 is that the peak force is proportional to the size of the nanorod tip. A similar size-dependent feature has been observed in membrane protrusions induced by an external pulling force, which is found to be proportional to the size of the region on which it is exerted [75, 77, 93].

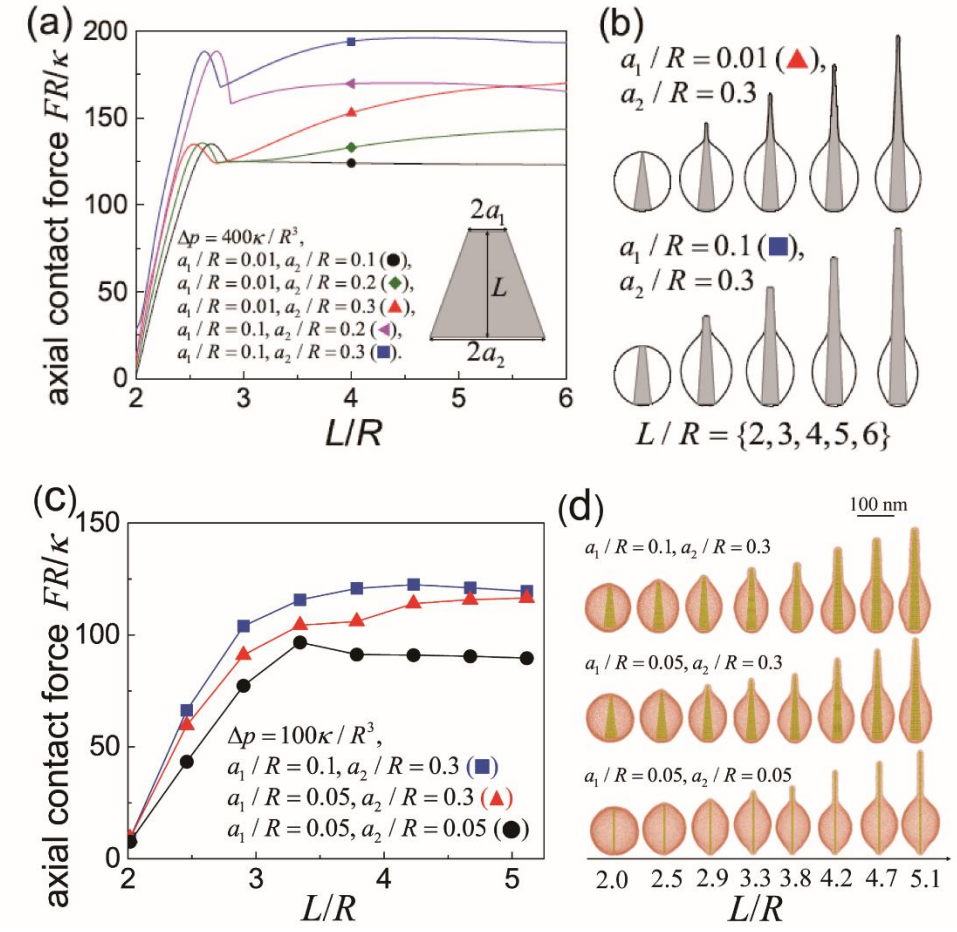

Figure 3.6. (a)Theoretical normalized axial contact force FR/κ as a function of the normalized nanorod length L/R and (b) vesicle morphologies induced by different geometries of the cone-shaped nanorods

at $\Delta p = 400R^3/\kappa$. Inset in (a) provides the nanorod geometry with $a_1 < a_2$. (c) MD simulated normalized axial contact force FR/κ as a function of the normalized nanorod length R/L and (b) vesicle morphologies induced by cone-shaped nanorods at $\Delta p = 100R^3/\kappa$.

In Figs. 3.3 and 3.4, the nanorods under consideration have uniform diameters. To investigate the effects of non-uniform cross-section of an encapsulated nanorod, we consider vesicle tubulation induced by cone- and screwdriver-shaped nanorods and determine the associated F. As shown in Fig. 3.6a for cone-shaped nanorods, the axial contact force increases to a peak value followed by a drop upon vesicle tubulation, similar to the results in Figs. 3.3, 3.4 and 3.5. It can be seen from Fig. 3.5 that the peak contact force is proportional to the size of the nanorod tip. Therefore, it is not surprising that vesicle tubulation occurs at the smaller end of the cone-shaped nanorod and at a smaller value of L/R compared to that in the case of a cylindrical nanorod. As shown in Fig. 3.6a, for a truncated cone of $a_1/R = 0.1$ and $a_2/R = 0.3$, the peak value of F is located around $L/R = 2.6$, which is smaller than the values of 2.9 or 3.2 for a uniform nanorod with $a_1/R = 0.1$ or 0.3 in Fig. 3.3. A similar conclusion is obtained at $a_1/R = 0.1$ and $a_2/R = 0.2$. Although the peak force (Fig. 3.6c) was not captured by our MD simulations due to the narrow range of parameter values within which it is located, as shown in Fig. 3.6a, we could observe similar behaviors from the simulated equilibrium morphologies. For example, the vesicle encapsulating a truncated cone of $a_1/R = 0.1$ and $a_2/R = 0.2$ forms a tubular membrane protrusion around $L/R = 3.3$, as shown in Fig. 3.6d; In contrast, it retains a lemon-like shape without tubular protrusions when encapsulating a uniform nanorod of the same L/R (Figs. 3.4 and 3.6d). Moreover, the peak force in Fig. 3.6a is slightly higher than the peak force in Fig. 3.3. A similar behavior is observed from MD simulations (comparing Fig. 3.6c with Fig. 3.4a). In the case of a large a_2 (e.g., $a_2/R = 0.3$), the force F could reach a higher level

than the first peak upon vesicle tubulation. This increase in force can be attributed to a gradual enlargement of membrane tubule in the radial direction (Fig. 3.6b), as also shown by our MD simulations in Figs. 3.6cd. In the case of small a_1 and a_2 (e.g., $a_1/R = 0.01$ and $a_2/R = 0.1$), the enlargement of membrane tubule in the radial direction is not evident (Fig. 3.6a). Therefore, upon vesicle tubulation, the axial contact force exhibits similar linear behaviors with respect to *L/R*, as in the case of an encapsulated cylindrical nanorod (comparing the black lines in Fig. 3.6a with the black lines in Fig. 3.3a).

The current results can be used to predict the buckling of a confined elastic rod. We exemplify the encapsulated rod of a uniform radius a as a bundle of weakly cross-linked actin filaments [59]. The critical buckling force for the bundle under simply supported boundary conditions is

$$f_{\mathrm{b}} = \pi^2 \frac{L_{\mathrm{p}} k_{\mathrm{B}} T}{L^2} N,$$

Where $L_{\mathrm{p}} = 18$ μm is the persistence length of a single filament [62], L is the overall length of the filament, and N is the filament number. Here we have assumed that the weakly bundled filaments buckle independently. Thus, f_{b} is linearly proportional to the filament number N. In the case of a hexagonal distribution of the filaments in the bundle of radius a, the filament number is around $N = \sqrt{2\pi/3}(3^{3/4} + \sqrt{2\pi}a/d)a/d + 1$, where the distance between neighboring filaments is taken as d = 20 nm [94]. The relation between the filament number N and the critical length *R/L*, at which the encapsulated bundle of actin filaments buckles, can be determined by comparing the critical buckling force f_{b} and the axial contact forces in Fig. 3.3.

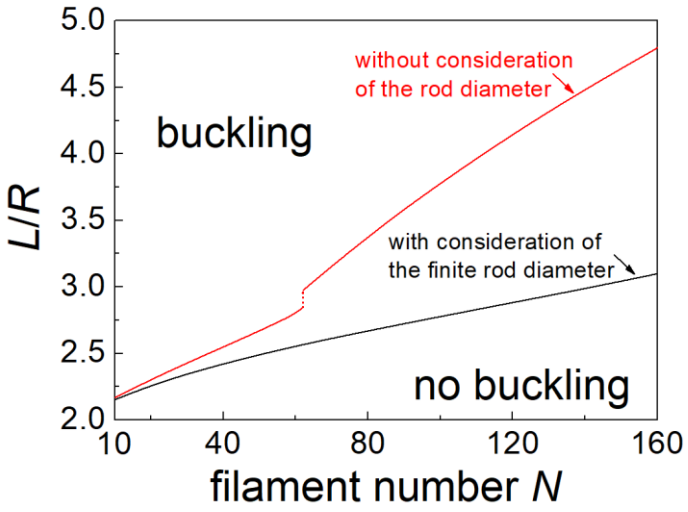

Figure 3.7. Buckling phase diagram in terms of the normalized rod length L/R and filament number N at R = 500 nm and $\Delta p = 400R^3/\kappa$. The filament bundle of L/R and N above the phase boundary would buckle due to the axial contact force.

For a vesicle of radius R = 500 nm at $\Delta p = 400R^3/\kappa$, a phase diagram on the buckling of an encapsulated cylindrical rod with and without consideration of the finite rod diameter is shown in Fig. 3.7. In the case where the effect of the rod diameter on the axial contact force is not considered, the vesicle is assumed to form point contact with the filament bundle of radius a and is subjected to a pair of outward point forces. As the force curve at $a/R = 0.01$ in Fig. 3.3a exhibits an indistinguishable difference from the point force case, it is compared with f_b and a discontinuous phase boundary is determined in which the discontinuity corresponds to the shape transformation of the vesicle before and after tubulation. At small N, no tubulation is formed. As N increases, the vesicle exhibits tubulation. In a more realistic case where the effect of the rod diameter on the force curve is not ignored, the critical length of the filament bundle becomes smaller and this trend becomes more striking as N increases. Moreover, the filament bundle cannot resist the axial force required for vesicle protrusion without buckling in our case study. Here we consider

the case $\Delta p = 400R^3/\kappa$. As Δp decreases, the phase boundaries before and after vesicle tubulation move upward and downward, respectively, as the axial contact force decreases at a lower Δp. As demonstrated in Fig. 3.7, the finite rod diameter is significantly important in regulating the buckling and protrusion of the confined filament bundle.

For a screwdriver-shaped nanorod with two cylindrical portions of different diameters, curve of F exhibits two local maxima from the theoretical analysis (Fig. 3.8a). The first local maximum located at a relatively small L/R is due to the formation of a tubular membrane protrusion enclosing the upper portion of the nanorod with a smaller diameter, and the second maximum located at a relatively large L/R is due to the growing protrusion enclosing the lower portion of the nanorod with a larger diameter (Fig. 3.8).

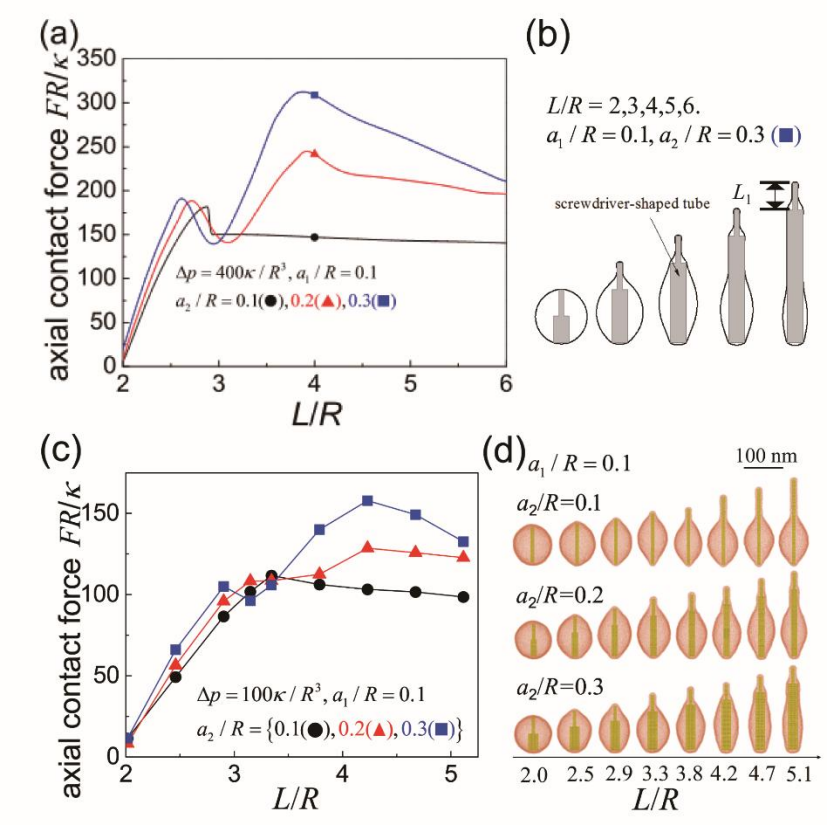

Figure 3.8. (a) Theoretical normalized axial contact force FR/κ as a function of the normalized length L/R of screwdriver-shaped nanorods of different radial sizes a_2 = 0.1, 0.2, and 0.3 and (b) vesicle

configurations at different lengths and $\Delta p = 400R^3/\kappa$. (c) MD simulated normalized axial contact force FR/κ as a function of the normalized nanorod length R/L and (b) vesicle morphologies induced by screwdriver-shaped nanorods at $\Delta p = 100R^3/\kappa$. Here a_1 and a_2 represent radii of the top and bottom parts of the screwdriver-shaped nanorods, and we take $a_1/R = 1$ and $L_1/R = 1$.

In addition to the cherry- or bowling pin-like shape, a vesicle encapsulating a long and rigid nanofiber could also resemble the Greek letter ϕ with a pair of tubular membrane protrusions [9]. Experiments, theoretical analysis, and MD simulations indicate that the ϕ-shaped vesicle with vertical symmetry has a slightly higher elastic energy than the cherry-shaped vesicle [7, 17, 72]. Further experimental studies show that the effective adhesive interaction, such as the binding or friction between the lipid membrane and the enclosed portion of the nanofiber, could facilitate the formation of a ϕ shaped vesicle [8]. In the current study, as the adhesive interaction between the nanofiber and vesicle membrane is neglected, the ϕ-shaped vesicle has not been observed. An interesting question worth further investigation is whether a cherry- or bowling pin-shaped vesicle encapsulating a nanorod is still in a more energetically stable state than a ϕ-shaped vesicle with two tubular protrusions in the presence of adhesive interaction between the nanorod and vesicle membrane. The adhesive interaction not only stabilizes the membrane protrusion but also plays a key role in cell spreading which is guided by the interfacial stiffness of the substrate surface [95].

The forms of vesicle tubulation analyzed here have also been observed in certain organelles subject to external forces arising from the collective motion of motor proteins along microtubules [78, 79]. For example, kinesin motors have been found to pull membrane tubular structures out of giant unilamellar lipid vesicles in vitro [78] and out of autophagosomes, a type of degradative compartment formed by the fusion of

autophagosomes and lysosomes during autophagy in vivo [96]. A key difference between the vesicle tubulation induced by a local pulling force and that induced by an encapsulated nanorod of a finite radius a is the presence of contact between the nanorod wall and vesicle membrane. A free tubular membrane structure with bending stiffness κ and membrane tension σ adopts a cylindrical structure of a uniform radius $r_0 = \sqrt{\kappa / (2\sigma)}$ based on the minimization of elastic energy $E = 2\pi rL[\kappa / (2r^2) + \sigma]$ with respect to *r* [56, 97]. In the case of a confined nanorod of radius $a > r_0$, contact between the nanorod wall and vesicle membrane serves as a physical constraint to prevent shrinking of the membrane tubular protrusion from radius *a* to r_0. From the point of view associated with membrane contact, another case similar to the vesicle tubulation induced by a thick encapsulated nanorod is the vesicle tubulation induced by an aspiration pipette at a large pipette aspiration pressure, where tight contact between the external surface of the vesicle tubule and the internal surface of the pipette could be formed.

From a mechanical point of view, a nuclear envelope can be modeled as a vesicle with a double lipid bilayer [15, 98]. In fission yeast cells, such as *Schizosaccharomyces pombe*, the elongation of spindle microtubules inside a nucleus lacking spindle pole bodies could lead to an abnormal transformation in the shape of the nuclear envelope from a spherical shape to a cherry- or ϕ-like shape [13-15, 98, 99]. For example, the overexpression of the Mia1p [14] or ned1 gene [13] leads to the formation of acentrosomal microtubule bundles within the nucleus, whose elongation further results in tubulation of the nuclear envelope during mitosis or interphase, a stage before mitosis in which cells replicate their chromosomes and synthesize substances for cell division. Similar protrusions of nuclear envelopes have been observed in msd1-null mutant cells, in which anchoring of the

microtubules to the spindle pole bodies is impaired [99]. Moreover, the use of microtubule-depolymerizing agents could suppress nuclear protrusions [98]. During anaphase in normal mitotic cell division, sister chromatids separate and move to opposite poles of the cell. The sister chromatids at the cell poles connected by microtubule bundles could be approximated as wide elastic tips to characterize the transformation of the shape of the nuclear envelope. Considering the force distribution on the chromatids [15] and their elastic deformation, our model on the interaction between the vesicle and a nanorod with two wide tips could be generalized to analyze the division of the nuclear envelope.

Our previous work on the pathogenicity of carbon nanotubes within lysosomes indicates that the lysosomal confinement on long and stiff carbon nanotubes leads to local membrane damage due to persistent axial contact between the nanotube and the inner membrane leaflet, causing lipid extraction, lysosomal permeabilization, cathepsin B release into the cytoplasm, and cell death [17]. Moreover, MD simulations show that the critical condition for inducing lysosomal permeabilization can be expressed as a power-law relation between the axial contact force and critical damage time; the lower the contact force, the longer it takes for the membrane damage to occur [17]. Our present work shows that the axial contact force depends not only on the nanotube length but also on its diameter. The larger the nanotube diameter or tip, the higher the maximum axial contact force. Based on our previous analysis [17], it can be predicted that at the same length, thicker nanorods and nanorods with wider tips could induce membrane damage in a shorter time and thus lysosomal membrane permeabilization, leading to pathogenicity. In the case of a screwdriver-shaped nanorod within a vesicle, the axial contact force curve exhibits two local maxima, and there are more edges of tight contact than in the case of a cylindrical

nanorod (Fig. 3.8). As membrane damage due to lipid extraction occurs more easily at edges of contact between the carbon nanotube and intracellular membrane [17], we expect that encapsulated screwdriver-shaped nanotubes with more sharp edges might induce more severe lysosomal damage and consequently more cathepsin B release, initiating a proteolytic cascade culminating in the activation of caspases and leading to cell death by apoptosis [100].

3.4 Conclusions

In summary, we presented in this chapter MD simulations and theoretical study to probe the mechanical interplay between a vesicle and an encapsulated rigid nanorod of finite and non-uniform diameter. Four distinct nanorod shapes are considered: a cylindrical nanorod, a nanorod with two wide ends, a cone-shaped nanorod, and a screwdriver-shaped nanorod. As the nanorod length increases, the vesicle encapsulating a uniform cylindrical nanorod transforms from an initial sphere to a lemon- or conga drum-like shape with vertical symmetry, and then to a cherry- or bowling pin-like shape with a single long, tubular membrane protrusion and a bulge. For a thick and long nanorod, the vesicle evolves from a bowling pin-like shape to a rod-like shape with vertical symmetry. Accompanying the vesicle shape transformation, the axial contact force exerted by the confining vesicle gradually rises to a peak as the nanorod length increases, and then decreases almost linearly with respect to the nanorod length upon vesicle tubulation. The thicker the nanorod, the higher the force peak. Similar features are present in the membrane tension curves. In the case of a cylindrical nanorod with two widened ends, the axial contact force peak becomes proportional to the size of the nanorod tip and is followed by a sharp, discontinuous drop to a constant upon a discontinuous vesicle tubulation evolving from a conga drum-like

shape. For a cone-shaped nanorod, vesicle tubulation occurs at the end of the nanorod with a smaller size, with which a smaller axial contact force is associated. After an immediate force drop upon vesicle tubulation, the axial contact force exerted on the cone-shaped nanorod could increase again as the nanorod length increases. The vesicle encapsulating a screwdriver-shaped nanorod is subjected to two peaks of axial contact force due to the formation of a tubular membrane protrusion enclosing the upper and lower nanorod portions of different diameters. Our analysis provides mechanistic insights into the importance of nanorod size and shape for regulating the mechanical interplay between cellular vesicles and encapsulated nanorods, which can serve as a theoretical basis to understand the cellular packing of actin or microtubule bundles [10, 96], filopodial protrusions [12], and mitotic cell division involving microtubule rearrangement [13-15, 98, 99]. Recalling that the enforced mechanical contact between carbon nanotubes and intracellular vesicles plays a key role in identifying the membrane damage and pathogenicity of one-dimensional carbon-based materials [17], our results predict that stiff carbon nanotubes with larger diameters, wider tips, or more edges could aggravate pathogenicity.

Chapter 4

Packing of flexible 2D materials in vesicles

4.1 Introduction

More than a decade of research has resulted in an ever increasing variety of engineered two-dimensional (2D) materials, such as graphene, hexagonal boron nitride (h-BN), graphitic carbon nitride, and transition metal dichalcogenides (e.g., MoS_2 and WS_2) [4, 5]. As 2D materials are being actively explored for applications in nanotechnology, their potential toxicity and health risks have become an urgent issue and are calling for more thorough understanding of their interactions with living cells and intracellular organelles [6]. Knowledge about the modes of packing of flexible sheets in vesicles is an important step towards understanding specific biological responses to 2D materials.

Depending on their mechanical, geometrical and surface properties, 2D materials exhibit a variety of modes of interaction with cell membranes [6]. For example, experiments and MD simulations have demonstrated that graphene and graphene oxide (GO) sheets can spontaneously pierce into cell membrane at sharp corner or edge asperities [26], resulting in destructive lipid extraction and loss of membrane viability [23]. With coating proteins, nanosheets show a variety of size-dependent cell internalization pathways. For example, large (micron-sized lateral dimension) protein-coated GO sheets, following initial attachment to the membrane of PLHC-1 cells, enter cells predominantly through phagocytosis, while small (500 nm) protein-coated GO sheets are internalized through clathrin-mediated endocytosis [101]. Pristine or lightly functionalized graphene nanoflakes

can either cut across a bilayer membrane as a transmembrane object or align along the interface between the monolayers when their lateral sizes are comparable to the membrane thickness [102-105]. The extent of hydrophilicity arising from oxidized edges and membrane microstructures play important roles in regulating these different interaction modes.

Following cell uptake, nanomaterials might accumulate in intracellular organelles like endosomes and lysosomes, and as indicated through experimental studies, their behavior under confinement in intracellular vesicles plays a critical role in their cytotoxicity [17, 106, 107]. It is found that long and stiff carbon nanotubes within lysosomes cause persistent tip contact with the inner lysosomal membrane, leading to lipid extraction, membrane permeabilization, and eventually cell death; while biologically soft carbon nanotubes become curved in lysosomes with low pathogenicity, without activating this nanomechanical toxicity pathway [17]. For 2D materials, new packing morphologies and fundamentally different modes of interaction with vesicles are expected. However, so far only a few experiments and no systematic simulations and theoretical work have been performed on this topic. Experiments have shown that GO sheets of small lateral size (350 nm) remain in their initial flat shapes, while large lateral sized GO sheets (2 μm) form wrinkles and tend to fold into lysosomes [19].

In this chapter, with an aim to reveal the mechanical behaviors of flexible sheets of 2D materials within (intracellular) vesicles, we consider the packing of a circular sheet in a spherical vesicle and the two-dimensional packing problem of a strip in a cylindrical vesicle CGMD simulations and theoretical analysis. It is shown that the packing morphologies and modes of interaction of the vesicle-sheet system strongly depend on the

bending rigidity ratio between the encapsulated sheet and the vesicle membrane. Phase diagrams of the packing morphologies will be determined based on a buckling analysis, and discussions will be made on differences between the cellular packing of flexible one- and two-dimensional materials. Our results indicate that both the elasticity and geometry of nanomaterials play important roles in regulating their mechanical behaviors under confinement in vesicles. Our findings may help develop a theoretical foundation to understand intracellular toxicity of 2D materials.

4.2 Model and methods

To elucidate the modes of mechanical interaction between a vesicle and an encapsulated flexible sheet of 2D material, we perform systematic CGMD simulations combined with theoretical modeling to demonstrate and analyze how the rigidity and geometrical factors regulate the morphology of the vesicle-sheet system. We adopt the same vesicle membrane model used in previous chapters. In this chapter, both spherical and cylindrical vesicles are simulated, the initial radius are set to be a = 50 nm. The CGMD simulations were performed at a constant pressure difference of $\Delta p \approx 40$ kPa, corresponding to a normalized value of $\Delta p\kappa/R^3 = 100$.

The encapsulated sheet is modeled as a 2D triangular lattice of CG beads, whose bending rigidity is determined by the stiffnesses of the connected bonds, angles, and dihedrals between the CG beads. Similar schemes have been used to model graphene nanosheets [108]. Specifically, the CG beads of two-dimensional triangular lattice have a nearest neighbor distance of 1.3 nm and internal angle θ of π/3. The nearest beads are connected by harmonic bonds with stiffness k_{harmonic}=200.0 kcal mol^{-1} rad^{-2}, and the rest

length between two nearest beads is r_1=1.3 nm. The internal angle θ of each triangle is maintained by the harmonic potential $U_{angle}(\theta)=k_{angle}(\theta-\pi/3)^2$ with spring constant k_{angle}=1.0 kcal mol^{-1} rad^{-2}, the planar dihedral angle φ of every two connected triangles is maintained by potential $\underline{U}_{dihedral}(\varphi)=k_{dihedral}(1+\cos\varphi)^2$, where $k_{dihedral}$ is used to tune the bending rigidity of the nanosheet. To measure the rigidity of the nanosheet, a triangular lattice of area A is folded into a cylinder of radius R_p as shown in Fig. 4.1. The elastic energy of a curved nanosheet is $\Delta E = \kappa_p A R_p^{-2}/2$ with κ_p as the bending rigidity of the nanosheet. Cylinders of different radius are constructed at each $k_{dihedral}$, and κ_p is calculated by the linear fitting between $2\Delta E/A$ and R_p^{-2} as shown in Fig. 4.1b. Fig. 4.1c shows that the nanosheet bending rigidity κ_p linearly depends on $k_{dihedral}$ with a relation $\kappa_p \approx 0.8\ k_{dihedral}$.

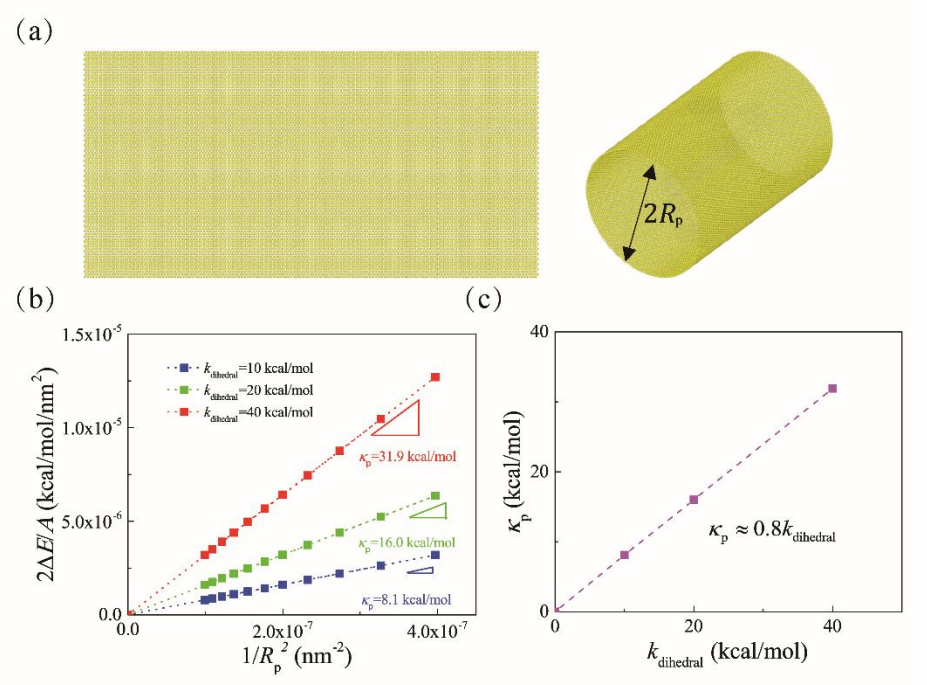

Figure 4.1. Modeling of a flexible nanosheet in CGMD simulations. (a) A two-dimensional triangular lattice structure is folded to a cylinder of radius R_p. (b) The relationship between $2\Delta E/A$ and R_p^{-2} at $k_{dihedral}$=10 kcal/mol, 20 kcal/mol, and 40 kcal/mol. The corresponding fitted bending rigidity of the nanosheets are 8.1 kcal/mol, 16.0 kcal/mol, 31.9 kcal/mol, respectively. (c) The relationship between the nanosheet bending rigidity and dihedral stiffness is fitted as $\kappa_p \approx 0.8k_{dihedral}$.

The MD simulations were performed under a constant ambient temperature 310 K with a time step fixed at 100 fs. In the study of rigid nanosheets, the encapsulated nanosheet was fixed while the vesicle membrane could move freely during the simulations. After equilibrium, another 100 ns simulation was performed for each case to get the average compression force due to the contact between the vesicle membrane and nanosheet. In the cases of flexible nanosheets, both the nanosheets and vesicle were allowed to relax to obtain the equilibrium morphologies.

4.3 Results

MD simulations can be employed to study mechanical interactions in a general vesicle-sheet system. To validate the simulation results, we focus on a combined MD and theoretical analysis of a couple of benchmark cases with axisymmetry or plane symmetry. The Canham-Helfrich model [22] is employed to characterize the vesicle deformation and the classical buckling analysis is adopted to evaluate the mechanical instability of the confined sheet.

4.3.1 Packing of a flexible sheet in a spherical vesicle

We first consider the packing of a rigid circular sheet of diameter L_p in a spherical vesicle of a fixed surface area $A_0 = 4\pi a^2$, a being the effective vesicle radius (see the inset in Fig. 4.2a). In the theoretical analysis, we assume that the axisymmetric vesicle adopts a configuration of upside-down symmetry as shown in the inset in Fig. 4.2 with the arclength s starting from the south pole of the vesicle and reaching $s = l$ at the edge of contact between the vesicle and the encapsulated sheet. The total energy of the system is expressed as [89]

$$E_{\text{tot}} = 2\pi\kappa\int_0^l r\left(\dot{\psi} + \frac{\sin\psi}{r}\right)^2 \mathrm{d}s - \Delta p(V - V_0) + \sigma(A - A_0) + 2\pi\int_0^l \mu(\dot{r} - \cos\psi)\mathrm{d}s, \quad (4.1)$$

where ψ, s and κ are the tangent angle, arclength, and bending rigidity of the vesicle membrane, and the dot denotes derivative with respect to the arclength s; Δp represents the pressure difference between the interior and exterior of the vesicle, V and A are the volume and surface area of the deformed vesicle, respectively; $V_0 = 4\pi a^3/3$ and $A_0 = 4\pi a^2$ are the initial volume and surface area of the spherical vesicle. The effective membrane tension σ is introduced as a Lagrange multiplier to enforce the constraint of the vesicle area; and $\mu(s)$ serves as a Lagrange multiplier function to impose the geometric relation $\dot{r} = \cos\psi$.

Introducing

$$\mathcal{L} = \kappa r\left(\dot{\psi} + \frac{\sin\psi}{r}\right)^2 - \Delta p r^2 \sin\psi + 2\sigma r + \mu(\dot{r} - \cos\psi)$$

allows us to rewrite $E_{\text{tot}} = 2\pi\int_0^l \mathcal{L}\mathrm{d}s + \Delta p V_0 - \sigma A_0$. Variation of E_{tot} leads to a set of Euler-Lagrange equations that govern the vesicle shape

$$\begin{cases} 2\kappa r\ddot{\psi} = -2\kappa\left(\dot{\psi} - \dfrac{\sin\psi}{r}\right)\cos\psi - \Delta p r^2\cos\psi + \mu\sin\psi, \\ \dot{\mu} = \kappa\left(\dot{\psi} + \dfrac{\sin\psi}{r}\right)\left(\dot{\psi} - \dfrac{\sin\psi}{r}\right) - 2\Delta p r\sin\psi + 2\sigma, \\ \dot{r} = \cos\psi. \end{cases} \quad (4.2)$$

Geometrical boundary conditions for the Euler-Lagrange equations (4.2) are $\psi(0) = 0$ and $r(0) = 0$ at the south pole of the vesicle ($s = 0$), and $\psi(l) = \pi/2$, $r(l) = L_p/2$. The conditions for the area constraint of the vesicle are $A(0) = 0$ and $A(l) = 2\pi a^2$. To determine the unknown l, we employ the method from ref. [109] and introduce a new

independent variable t such that t=0 at the south pole (s=0) and t=1 at s=l. The governing equations are then reparametrized by replacing ds with ldt. The conservation of the Hamiltonian function $H = -\mathcal{L} + \dot{\psi}\partial\mathcal{L}/\partial\dot{\psi} + \dot{r}\partial\mathcal{L}/\partial\dot{r}$ results in $\mu(0) = 0$ as discussed in refs. [109, 110]. With the knowledge of the boundary conditions, the governing equations could be solved numerically for the energy and configuration of the system, as well as the membrane tension $\sigma(=-\partial E_{\text{tot}}/\partial A > 0)$. The contact force per unit length f upon the closed contact edge is determined as $f = \partial E_{\text{tot}}/\partial[\pi(L_{\text{p}}/2)^2]$ or $f = 2\mu(l)/L_{\text{p}}$. In parallel to the theoretical model, we perform MD simulations for $\Delta p a^3/\kappa$=100 and different $L_{\text{p}}/(2a)$.

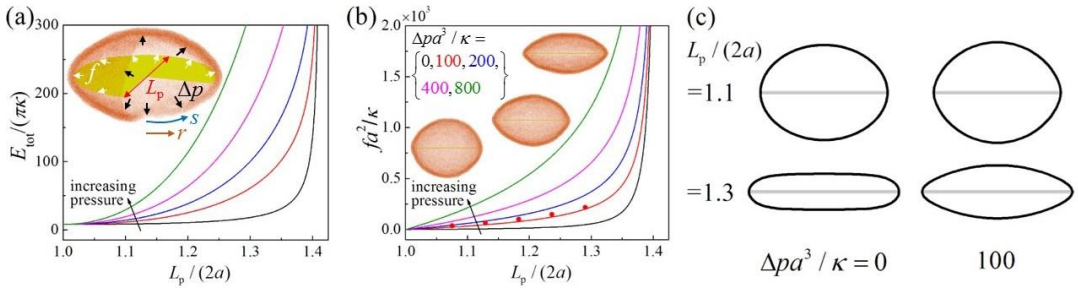

Figure 4.2. Variations of (a) the total free energy E_{tot} and (b) compressive contact force per unit length f of a rigid sheet confined in a spherical vesicle as functions of the sheet-vesicle size ratio $L_{\text{p}}/(2a)$ at different values of pressure difference Δp. (c) Selected shapes of the vesicle-sheet system with $L_{\text{p}}/(2a)$ = 1.1, 1.3 and $\Delta p\kappa/R^3$ = 0, 100 from theoretical modeling. The inset in (a) is the MD simulation model. White and black arrows represent the contact force f and pressure difference Δp, respectively. In (b), red dots are results from the MD simulations, and the insets show equilibrium vesicle morphologies at $\Delta p\kappa/R^3$ = 100 and $L_{\text{p}}/(2a)$ = 1.08, 1.18 and 1.29.

As indicated in Fig. 4.2a,b, both the total free energy E_{tot} and the contact force f increase at increasing rates with the sheet diameter L_{p} or pressure difference Δp. Fig. 4.2c plots the theoretical prediction of selected vesicle configurations at different L_{p} and Δp. As L_{p} increases, the vesicle becomes inflated and the central region of the vesicle bulges. Similar behaviors are observed in MD simulations (insets in Fig 4.2b).

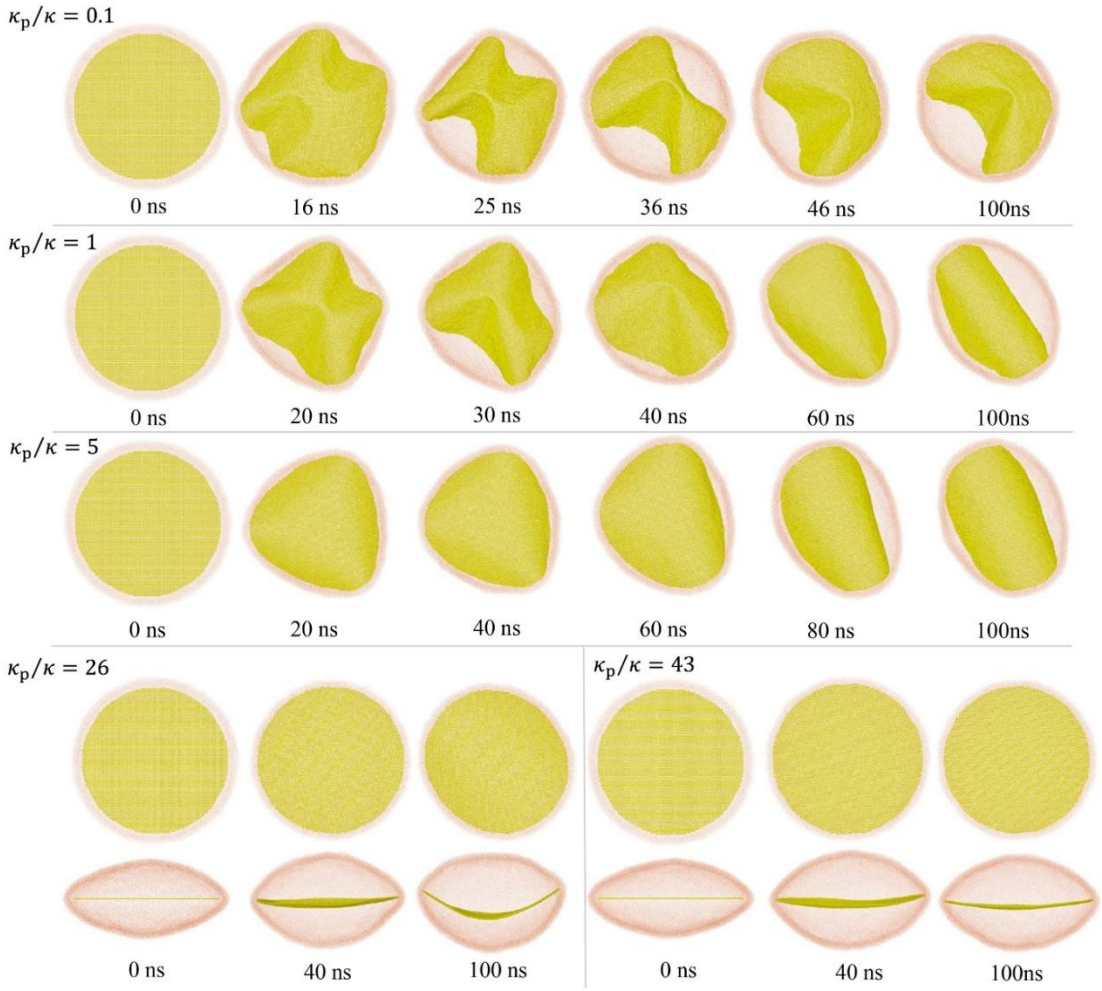

Figure 4.3. Temporal evolution of the packing morphology of an initially spherical vesicle encapsulating a flexible circular sheet of normalized diameter $L_p/(2a) = 1.24$ under normalized pressure $\Delta p\kappa/R^3 = 100$. The bottom row displays the side view of the system whose corresponding top view is provided in the fourth row.

Next we consider the packing of a flexible circular nanosheet in a spherical vesicle. As the compressive contact force on the sheet edge is proportional to its size, it is anticipated that an encapsulated sheet of sufficiently large size and small bending rigidity will undergo buckling instability. Fig. 4.3 shows typical time sequenced snapshots of system morphologies at $L_p/(2a) = 1.24$ and for different $\kappa_p/\kappa = 0.1$, 1, 5, 26 and 43. At

κ_p/κ = 0.1, a very soft and flexible sheet becomes crumpled into a structure with two developable cone vertices [111] and eventually evolves to a conical structure with no stretching, and the vesicle maintains a nearly spherical shape. In this case, the relatively strong vesicle confinement induces large and complex deformation of the soft nanosheet, with partial edge contact between the crumpled nanosheet and vesicle membrane. This is similar to a flat elastic thin sheet packed in a rigid hollow cylinder exhibiting a conical structure described by the equation of an elastica [112-114]. In the case of κ_p/κ = 1, the nanosheet with bending rigidity comparable to that of the vesicle membrane adopts a configuration of mirror symmetry, undergoing significant cylindrical bending (generalized plane strain bending) deformation while the vesicle adopts a dumpling-like shape. As the nanosheet becomes stiffer (e.g., κ_p/κ = 5), it evolves first to a shape of three-fold symmetry with a nearly flat region at the center, then undergoes cylindrical bending deformation with elastic energy released from these three curved regions. In comparison, very stiff nanosheets (e.g., κ_p/κ = 26 and 43 here) display no significant deformation in the vesicle. As the side views in the bottom row of Fig. 4.3 indicate, the nanosheet of κ_p/κ = 26 adopts a cylindrical mode of bending deformation and maintains a configuration of mirror symmetry; while the nanosheet of κ_p/κ = 43 undergoes slight axisymmetric bending. This rigidity-dependent shape transformation of the encapsulated nanosheet can be understood as follows. As long as the elastic deformation of the nanosheet is within its linear range, the sheet maintains an essentially axisymmetric shape. When the nanosheet becomes more flexible, its deformation falls into a geometrically nonlinear range, in which maintaining an asymmetrical deformation mode requires both bending and in-plane stretching. In this case, a cylindrical bending mode could occur with minimal in-plane stretching. Therefore,

below a critical ratio of bending rigidity, the encapsulated nanosheet adopts a cylindrical mode of bending deformation. Similar deformation mode transition has been predicted theoretically in the bifurcation study of a thin film-substrate system subject to a mismatch strain [115]. In addition to MD simulations which is capable of characterizing the complex packing configurations, significant efforts are required to build a complete theoretical model on packing of a flexible nanosheet in a spherical vesicle. This challenging task calls for fundamental studies aimed at understanding the mechanics of crumpled thin sheets [116] and deserves further dedicated investigations in the future.

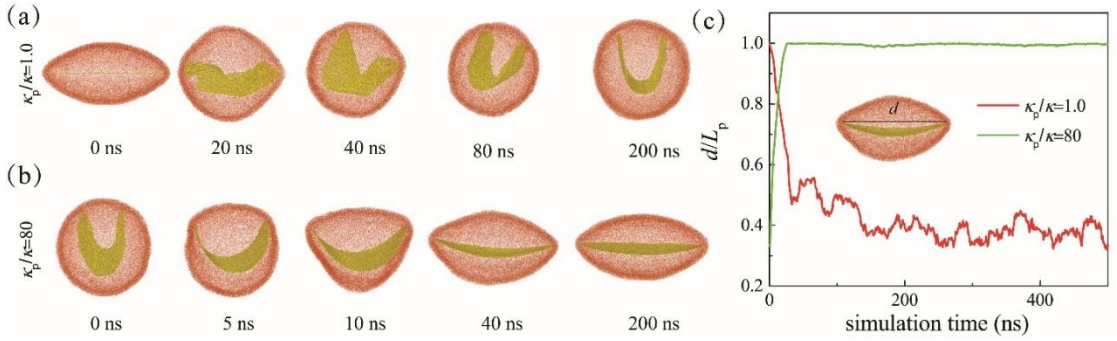

Figure 4.4. Time sequences of MD simulations showing morphological evolutions of the vesicle-sheet system. (a) Buckling of an initially flat nanosheet of bending rigidity $\kappa_p/\kappa = 1$ in a spherical vesicle. (b) Flattening of an initially curved nanosheet of bending rigidity $\kappa_p/\kappa = 80$. The nanosheets in both cases have the normalized diameter of $L_p/(2a)$=1.29. (c) Variations of distance d between two edges of the nanosheets during the morphological evolutions shown in (a) and (b). Inset in (c) illustrates the definition of the edge distance *d*.

For an encapsulated sheet of bending rigidity comparable to or larger than that of the vesicle membrane, further simulations indicate that the equilibrium states of the vesicle-sheet system are insensitive to the initial packing configurations (Fig. 4.4a,b). An initially flat nanosheet of relatively small bending rigidity (e.g., $\kappa_p/\kappa = 1$) buckles in a short period of time under the compressive force from the vesicle confinement. After long time simulations, the system reaches an equilibrium state in which the nanosheet is strongly

curved in the cylindrical bending mode and the vesicle adopts a dumpling-like shape with two mirror symmetry planes (Fig. 4.4a,c). The confined nanosheet undergoes shape fluctuations (characterized by the edge distance d) due to thermal undulation. For an initially curved nanosheet of large bending rigidity (e.g., $\kappa_p/\kappa = 80$), the sheet returns to the flat configuration with released bending energy compensated by the deformation of the vesicle (Fig. 4.4b,c). At the same time, the vesicle evolves from an initial dumpling-like shape to a lens-like shape. Note that the nanosheet with large bending rigidity exhibits very small shape fluctuations at equilibrium (Fig. 4.4c).

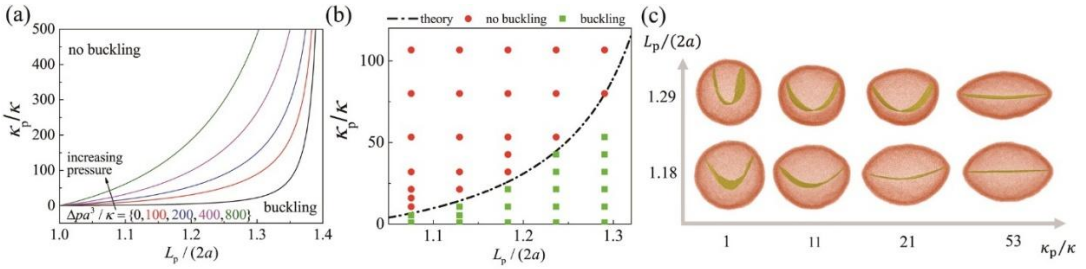

Figure 4.5. (a) Phase diagram on the packing instability of the encapsulated flexible circular sheet with respect to the bending rigidity ratio κ_p/κ and size ratio $L_p/(2a)$ at different pressures. (b) MD simulations showing the buckling instability at $\Delta p\kappa/R^3 = 100$. The dashed line corresponds to the red curve in (a). (c) Representative equilibrium morphologies of the vesicle-sheet system at selected κ_p/κ and $L_p/(2a)$ from MD simulations.

As demonstrated in MD simulations, an encapsulated flexible nanosheet of sufficiently large size and small bending rigidity could buckle under the compressive contact force f along the edge. Based on the Euler buckling criterion under the assumption that the maximal deflection of the nanosheet is small compared to its length, the critical buckling force per unit contact length is $f_c = 16.79\kappa_p / L_p^2$, where the bending rigidity $\kappa_p = E_p h_p^3/[12(1-\nu_p^2)]$ depends on the Young's modulus E_p, thickness h_p, and Poisson ratio

ν_p of the nanosheet [117]. Substituting f_c into f, we can determine a buckling phase diagram for the encapsulated nanosheet inside a vesicle with respect to the sheet-vesicle size ratio $L_p/(2a)$ and bending rigidity ratio κ_p/κ (see Fig. 4.5a). As shown in Fig. 4.5a, larger and softer encapsulated nanosheets are easier to buckle. The theoretical prediction of buckling at $\Delta p\kappa/R^3 = 100$ is confirmed by our MD simulations (Fig. 4.5b) with selected sheet-vesicle system morphologies demonstrated in Fig. 4.5c. Generally, larger and softer nanosheets are curved more significantly inside their confining vesicles (Fig. 4.5c).

4.3.2 Two-dimensional packing of a flexible strip in a cylindrical vesicle

In a two-dimensional configuration, we limit our attention to the packing of a flexible strip in a cylindrical vesicle with a constant contour length $2\pi a$, a being the effective radius of the vesicle (see the inset in Fig. 4.6a). The total energy of the system per unit length in the out-of-plane direction is [118, 119]

$$\begin{aligned} E_{\text{tot}} &= \frac{\kappa}{2}\int c^2 \mathrm{d}s + \frac{\kappa_p}{2}\int c_p^2 \mathrm{d}s_p - \Delta p(A-\pi a^2) + \sigma\left(\int \mathrm{d}s - 2\pi a\right) \\ &+ \int\left[\mu(\dot{r}-\cos\psi) + \eta(\dot{z}-\sin\psi)\right]\mathrm{d}s, \end{aligned} \tag{4.3}$$

where $c(=\dot{\psi})$, $\psi(s)$, s, and κ are the curvature, tangent angle, arclength and bending rigidity of the vesicle membrane, respectively, and the dot denotes derivative with respect to the arclength s starting from the left contact edge. For the encapsulated strip, the corresponding quantities are denoted with subscript 'p'; The first and second terms correspond to the bending energy of the vesicle and strip, respectively; Δp represents the pressure difference between the interior and exterior of the vesicle, and A is the enclosed area of the deformed vesicle in two dimensions. The fourth term is introduced to enforce the constraint that the vesicle circumference L is fixed at $2\pi a$, where the effective

membrane tension σ serves as the Lagrange multiplier. In the last term, $\mu(s)$ and $\eta(s)$ are the Lagrange multipliers to enforce geometric relations $\dot{r} = \cos\psi$ and $\dot{z} = \sin\psi$.

In the case of encapsulating a rigid flat strip of a uniform width L_p, we assume that the vesicle adopts a configuration of upside-down symmetry as shown in the inset in Fig. 4.6a. Variation of E_{tot} leads to the following Euler-Lagrange equations that govern the vesicle shape

$$\begin{cases} \ddot{\psi} = (\mu \sin\psi - \eta \cos\psi - \Delta p r \cos\psi)/\kappa, \\ \dot{\mu} = -\Delta p \sin\psi, \\ \dot{\eta} = 0, \\ \dot{r} = \cos\psi, \\ \dot{z} = \sin\psi. \end{cases} \tag{4.4}$$

Six boundary conditions corresponding to equations (4) are $\psi(0) = -\pi/2$, $r(0) = -L_p/2$ and $z(0) = 0$ at $s = 0$ (left contact edge), and $\psi(\pi a) = \pi/2$, $r(\pi a) = L_p/2$, and $z(\pi a) = 0$ at $s = \pi a$ (right contact edge). By using the shooting method, the governing equations could be solved numerically for the elastic energy and configuration of the system. The edge contact force f per unit length of the encapsulated strip is determined as [120]

$$f = \partial E_{tot} / \partial L_p \text{ or } f = 2\mu(0)$$

and the effective membrane tension σ is [119, 121, 122]

$$\sigma = -\partial E_{tot} / \partial L \text{ or } \sigma = (\ddot{c}\kappa + c^3\kappa/2 + \Delta p)/c.$$

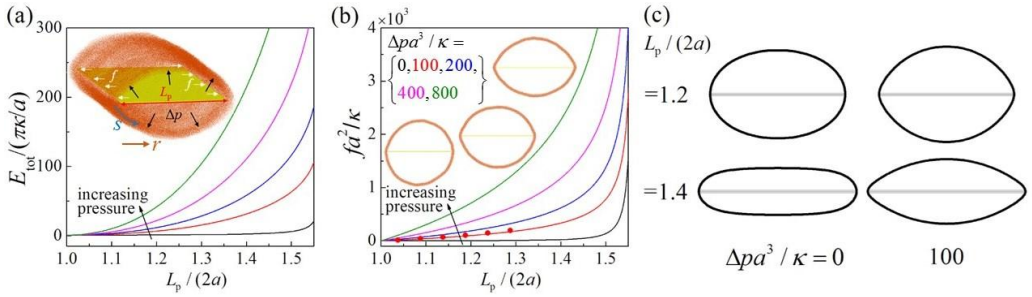

Figure 4.6. Variations of (a) the total free energy E_{tot} and (b) edge contact force of an encapsulated rigid strip in a cylindrical vesicle as functions of the strip-vesicle size ratio $L_p/(2a)$ at different Δp. (c) Selected shapes of a cylindrical vesicle encapsulating a rigid strip of widths $L_p/(2a)$ = 1.2 and 1.4 at $\Delta p\kappa/R^3$ = 0 and 100 from theoretical modeling. The inset in (a) is the MD simulation model. White and black arrows represent the contact force f and pressure difference Δp, respectively. In (b), red dots represent results from the MD simulations, and insets show equilibrium vesicle morphologies at $\Delta p\kappa/R^3$ = 100 and $L_p/(2a)$ = 1.09, 1.19 and 1.29.

Fig. 4.6a,b shows the total energy E_{tot} and edge contact force f at different Δp in the two-dimensional packing of a rigid strip in a cylindrical vesicle. Similar to the packing of a rigid circular sheet in a spherical vesicle, both E_{tot} and f increase at increasing rates with the strip size L_p. A higher Δp induces higher E_{tot} and f. Theoretical prediction of selected vesicle configurations at different L_p and Δp are shown in Fig. 4.6c. In the presence of a pressure difference, the vesicle is inflated and its central region bulges. The contact force and equilibrium vesicle morphologies at $\Delta p\kappa/R^3$ = 100 have also been obtained from MD simulations (see the red dots and insets in Fig. 4.6c) and are consistent with the theoretical predictions.

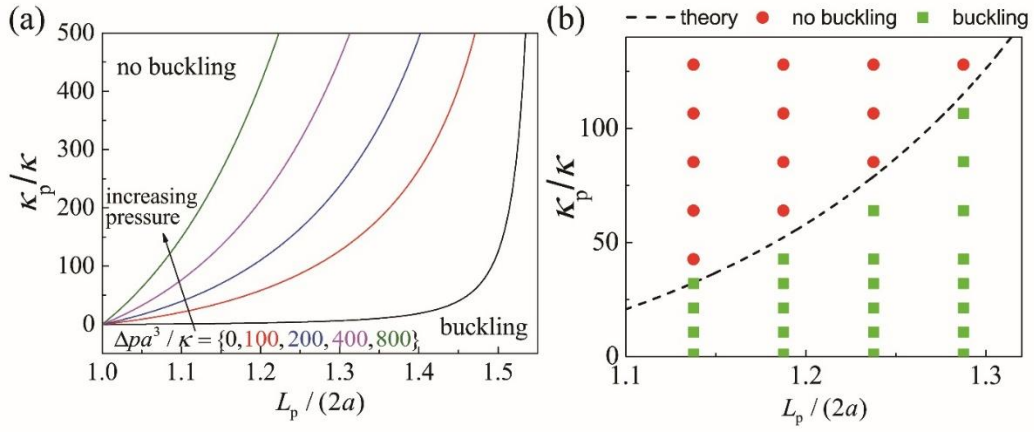

Figure 4.7. Phase diagram for the two-dimensional packing of an encapsulated flexible strip in a cylindrical vesicle with respect to the strip-vesicle bending rigidity ratio κ_p/κ and size ratio $L_p/(2a)$ from the theoretical analysis at different values of the pressure difference Δp (a), and from MD simulations at $\Delta p\kappa/R^3 = 100$ (b). The dashed line in (b) corresponds to the red curve in (a).

An encapsulated flexible strip of sufficiently large size and small bending rigidity will buckle into a curved shape due to the compressive edge contact force by the vesicle confinement. Based on the Euler buckling criterion, the critical buckling force per unit contact length is $f_c = \pi^2 \kappa_p / L_p^2$. Comparing the edge contact force f to the critical buckling force f_c, we can theoretically determine a buckling phase diagram for the encapsulated strip (Fig. 4.7a) with respect to the bending rigidity ratio and size ratio. As L_p and Δp increase, so does the critical bending rigidity of the encapsulated strip. The theoretical prediction at $\Delta p\kappa/R^3 = 100$ is confirmed by our MD simulations (Fig. 4.7b).

Considering large deflections of a bent strip, the deformed shape subject to a pair of edge contact forces f is locally governed by $\kappa_p \mathrm{d}^2\psi_p / \mathrm{d}s_p^2 + f \sin\psi_p = 0$, which can be integrated as [123]

$$\left(\frac{\mathrm{d}\psi_p}{\mathrm{d}s_p}\right)^2 = \frac{2f}{\kappa_p}(\cos\psi_p - \cos\psi_0),$$

where $\psi_0 = \psi_p(0)$ is the tangential angle of the strip at the left contact edge. Here we have treated the encapsulated strip as an inextensible planar elastica. Assuming that the strip buckles downwards ($\psi_0 \le 0$), the contact force f at a certain ψ_0 can be expressed as an elliptic integral,

$$L_p = \sqrt{\frac{\kappa_p}{f}} \int_{\psi_0}^{\psi_p} \frac{d\psi'}{\sqrt{2(\cos\psi' - \cos\psi_0)}}, \tag{4.5}$$

and the bending energy of the strip can be determined as [123]

$$\begin{aligned} E_p &= \frac{1}{2}\kappa_p \int \left(\frac{d\psi_p}{ds_p}\right)^2 ds_p = f\int(\cos\psi - \cos\psi_0)ds_p \\ &= \sqrt{\frac{f\kappa_p}{2}} \int_{\psi_0}^{\psi_p} \sqrt{(\cos\psi' - \cos\psi_0)}\, d\psi'. \end{aligned} \tag{4.6}$$

With geometric relations $dr_p / ds_p = \cos\psi_p$ and $dz_p / ds_p = \sin\psi_p$, the shape of the deformed strip is [123]

$$r = -\sqrt{\frac{\kappa_p}{f}} \int_{\psi_0}^{\psi_p} \frac{\cos\psi' d\psi'}{\sqrt{2(\cos\psi' - \cos\psi_0)}} \text{ and } z = -\sqrt{\frac{\kappa_p}{f}} \sqrt{2(\cos\psi_p - \cos\psi_0)}. \tag{4.7}$$

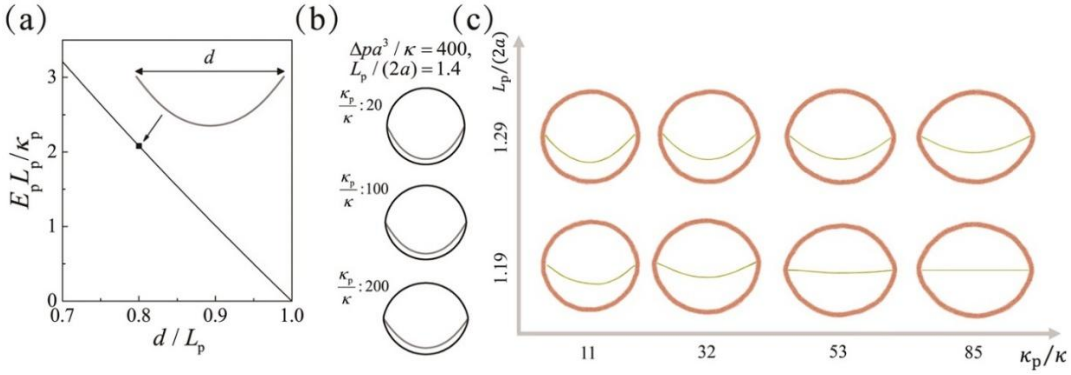

Figure 4.8. (a) Bending energy of an inextensible strip with finite deflection. (b) The strip-vesicle configurations for selected bending rigidity ratios at $\Delta p\kappa/R^3 = 400$ and $L_p/(2a) = 1.4$ from theoretical modeling. (c) Representative equilibrium system morphologies of selected size ratio and bending rigidity ratio at $\Delta p\kappa/R^3 = 100$ from MD simulations. Inset in (a) plots the strip configuration at

$d/L_p = 0.8$ with d as the edge distance.

According to equations (4.5-7), we can obtain the bending energy and the corresponding configuration of the strip at different bending levels. For example, Fig. 4.8a plots the strip bending energy E_p as a function of the edge distance d, and $E_p(d)$ exhibits an approximately linear relation with d. In the two-dimensional problem of encapsulating a flexible strip inside a cylindrical vesicle, substantial mechanical deformation can take place. The summation of E_p in Fig. 4.8a and E_{tot} in Fig. 4.6a enables us to determine the energetically favorable system configurations as illustrated in Fig. 4.8b. As κ_p/κ decreases, the encapsulated strip is more significantly curved, which is also seen in MD simulations (see Fig. 4.8c). As shown in Fig. 4.9a, a relatively flexible flat strip of a width larger than the vesicle diameter ($\kappa_p/\kappa = 11$ and $L_p/(2a) = 1.24$) buckles upon the compressive force on the contact edge; while for a relatively stiff strip ($\kappa_p/\kappa = 85$) of the same L_p in an initial curved configuration, it gradually becomes flattened as shown in Fig. 4.9b. Further analysis on the temporal evolution of the edge distance d of the strip indicates that the strip undergoes shape fluctuations with a reducing amplitude as the system evolves to an equilibrium state upon thermal undulation (Fig. 4.9c). These results suggest that the equilibrium state of the vesicle-strip system is insensitive to the initial system configuration, similar to the three-dimensional packing of a flexible circular sheet in a vesicle (Fig. 4.4). In this section, we limit our studies to the cases in which only the edge contact is fully formed. For more flexible strips or those of much larger widths, the surface contact between the vesicle and strip could be modeled by, for example, the Lennard-Jones interaction potential [124].

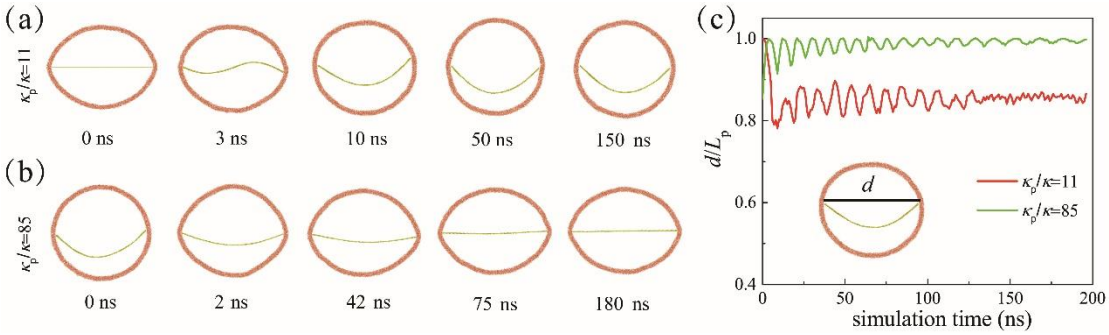

Figure 4.9. Time sequences of MD simulations showing morphological evolution of the vesicle-strip system in two dimensions. (a) Buckling of an initially flat strip of bending rigidity κ_p/κ = 11. (b) Flattening of an initially curved strip of bending rigidity κ_p/κ = 85. (c) Time evolution of the distance d between the two contact edges. Inset in (c) illustrates the definition of the edge distance d.

4.4 Discussion

Packing of flexible sheets in vesicles serves as a model to understand cellular interaction with 2D materials. Through endocytosis, nanosheets engulfed by cells might undergo intracellular transport into and become encapsulated by subcellular vesicles such as endosomes and lysosomes. Though the bending rigidity of lipid bilayers could vary in a wide range from 20 k_BT to 150 k_BT, depending on the membrane composition [71], a value on the order of 20 k_BT can be taken as a typical bending rigidity for the lipid membrane of a subcellular vesicle [17, 125], in which the most abundant phospholipids are phosphatidylcholine, phosphatidylethanolamine and sphingomyelin [126]. Depending on the number of atomic layers and chemical composition, the bending rigidity κ_p of engulfed 2D nanosheets could be comparable to, or significantly larger than, that of the biomembrane. For example, MD simulations indicate that κ_p is about 56 k_BT for single-layered graphene [127], 700 k_BT for MoS_2 bilayer [127], and 375 k_BT for MoS_2 monolayer [128]. In experiments, the bending rigidity of a monolayered GO nanosheet with a carbon-

to-oxygen ratio (4:1) is measured around 180 k_BT [129]. A typical radius of lysosome is about a = 0.5 μm, and the pressure difference due to osmolarity change is about 300 Pa [17]. According to the buckling analysis in Fig. 4.5a, the critical bending rigidity of an encapsulated sheet at bucking is on the order of few hundred k_BT. Therefore, for packing in intracellular vesicles, the MoS_2 bilayer can be regarded as rigid, while single-layered graphene, GO, and MoS_2 monolayer might be considered flexible.

Experiments and MD simulations indicate that the packing of one-dimensional nanofibers in vesicles strongly depends on the nanofiber-membrane bending stiffness ratio and size ratio [9, 38, 72]. For example, an encapsulated long and stiff nanofiber could give rise to a cherry-shaped vesicle with a single tubular protrusion or a ϕ-shaped vesicle with a pair of tubular protrusions [9, 72]; while an encapsulated flexible nanofiber could exhibit, depending on the nanofiber length, an axisymmetric lemon-like vesicle shape with a pair of protruding tips or a non-axisymmetric dumpling-like shape with the nanofiber curved against the vesicle membrane [38, 72]. In comparison with the packing morphology of nanofibers in vesicles, our present study shows that the packing of 2D sheets without edge asperities typically involves milder deformation and no (planar) protrusions. The packing morphology of a one-dimensional nanofiber in a vesicle typically depends on the initial configuration of the vesicle-nanofiber system [72]. For the packing of an initially curved long nanofiber inside a spherical vesicle, the vesicle could exhibit, depending on the nanofiber stiffness, a non-axisymmetric dumpling-like shape without tubular protrusions or a cherry-like shape with a single tubular protrusion, and the boundary between these two packing morphological phases is well characterized by the classical Euler buckling theory [72]. If the nanofiber is initially straight in the vesicle, the same morphological phases exist

but the phase boundary does not obey the Euler buckling criterion [72]. In contrast, the packing of 2D sheets in vesicles under consideration appears to be insensitive to the initial vesicle-sheet configurations, as shown in Figs. 4.4 and 4.9. The reason for this is that the packing process of a nanofiber involves a significant barrier associated with vesicle tubulation [72, 77], while that of a 2D sheet involves no such barrier. An interesting open question is under what conditions an energy barrier would emerge as the encapsulated nanomaterial varies from a one-dimensional fiber to a 2D sheet.

In this chapter we have assumed that there is no (evident) adhesive interaction between the encapsulated sheet and vesicle. It is not clear whether such adhesion could lead to two-dimensional membrane protrusions. Experimental and theoretical studies reveal that a linear aggregation of adhesive nanoparticles within a vesicle could give rise to vesicle tubulation [130, 131], and binding between microtubule and vesicle membrane through certain proteins could stabilize a ϕ-shaped vesicle [8]. However, relatively little is known about the packing of adhesive sheets in a vesicle.

The encapsulated sheets considered here are assumed to have smooth edges without edge asperities or sharp corners. Previous theoretical modeling and MD simulations have shown that edge asperities could significantly influence the manner by which membrane interacts with nanosheets [23, 26, 103-105, 132]. For example, edge asperities of graphene nanosheets can reduce the energy barrier of membrane penetration to only a few k_BT, enabling spontaneous penetration [26]. Theoretical analysis accounting for the bilayer microstructure of the lipid membrane indicates that transmembrane nanosheets exhibit a near-perpendicular configuration with respect to the membrane surface, driven by membrane splay and tension energies [105]. Once membrane penetration by graphene

takes place, lipid molecules could be extracted out of the membrane due to strong interactions between the hydrophobic lipid hydrocarbon chains and graphene surface [17, 23], and lipid extraction could result in membrane permeabilization, membrane damage and cell death [17, 23]. These phenomena suggest that nanosheets such as graphene with edge asperities or sharp corners might pierce through a confining vesicle or even escape from it; In these cases, the buckling of a nanosheet under strong confinement might not be applicable. For sheets free of edge asperities or those polar 2D materials like highly oxidized graphene oxide, h-BN, and MoS_2, direct piercing of membrane requires overcoming a large energy barrier or is energetically unfavorable. Barring direct penetration, the mechanical interaction modes discussed in our study should be applicable. Recent experimental studies of intracellular trafficking of nanoparticles report that nanoparticles with low sharpness could stably reside in the intracellular vesicles such as endosomes or lysosomes, while those sharp-shaped nanoparticles could escape from the vesicles and accumulate in the cytosol [107]. Further simulations and theoretical studies will be required to fully understand the coupling between elastic deformation and geometrical effect in the packing of 2D materials in cells or vesicles.

4.5 Conclusions

MD simulations and theoretical analysis have been performed to explore the packing of flexible sheets in vesicles. In particular, we have studied the packing of a flexible circular sheet in a spherical vesicle and two-dimensional packing of a strip in a cylindrical vesicle. It is shown that the sheet-vesicle size and rigidity ratios play important roles in regulating the packing morphologies of the vesicle-sheet system. As the sheet rigidity increases, it undergoes complex shape transformations to a rich variety of morphologies including a

conical shape, a shape of three-fold symmetry with a nearly flat central region and three curved marginal regions, a generalized cylindrically curved shape, an axisymmetrically buckled shape, and the initial circular shape. Phase diagrams of the packing morphology have been established based on the critical conditions for buckling instability. In comparison to cellular packing of long and stiff one-dimensional materials with tubular membrane protrusions, no membrane protrusion has been observed for a vesicle encapsulating a 2D sheet. This study shows how size and elasticity of 2D materials could regulate their packing morphology in vesicles. Our findings may have important biological implications on the cytotoxicity of 2D materials and may help provide a theoretical foundation to understand biological and environmental interactions of 2D materials.

Chapter 5

Mechanics of selective membrane-targeting antibiotics

5.1 Introduction

Staphylococcus aureus is a Gram-positive opportunistic human pathogen carried by approximately one third of the human population. Despite antibiotic availability, *S. aureus* infections are often hard-to-cure and remain one of the major causes of death [133], in part due to the ability of *S. aureus* to enter into a non-growing antibiotic-tolerant state, referred to as persisters [133, 134]. Persisters exhibit significantly reduced biosynthetic processes, which are the major targets for most antibiotics [134]. Persisters also exist in a metabolically low-energy state [135] that prevents the energy-dependent uptake of antibiotics such as aminoglycosides [28]. *S. aureus* persisters are present in high numbers in stationary-phase suspension cultures and biofilms [25, 28, 29] and are responsible for chronic and relapsing infections such as endocarditis, osteomyelitis, and prosthetic implant infections [135].

Bacterial membranes are attractive anti-persister targets because they can be disrupted independently of growth. Although membrane-active agents are typically toxic to mammals due to low membrane selectivity [136], the clinical success of daptomycin has sparked new interest in membrane-active antimicrobial therapeutics [136]. The lipophilic tail of daptomycin, a natural cyclic lipopeptide synthesized by *Streptomyces roseosporus*, inserts into Gram-positive bacterial membranes forming oligomeric pores, causing

membrane depolarization, potassium ion efflux, and rapid cell death [137]. Despite strong antimicrobial potency against growing bacterial cells, daptomycin has not been reported to be effective against persisters [138, 139].

Recently, we described the identification of membrane-active synthetic retinoids that are efficacious in killing MRSA persisters [25]. They are also relatively non-toxic because they exhibit a significant amount of selectivity for Gram-positive bacterial membranes compared to mammalian membranes [25]. Like daptomycin, the antimicrobial retinoids also appear to insert into Gram-positive bacterial membranes causing rapid permeabilization and cell death. In contrast to daptomycin, however, a subset of the membrane-active synthetic retinoids also kill non-growing MRSA persister cells [25]. In addition to the synthetic retinoids, two additional membrane active compounds with anti-MRSA activity, NH125, a histidine-kinase inhibitor [140], and nTZDpa, a non-thiazolidinedione peroxisome proliferator-activated receptor gamma partial agonist have been described [24]. Although NH125 and nTZDpa have excellent anti-MRSA persister activity, they both cause substantial hemolysis of red blood cells at high concentrations (over 32 μg/mL) [24, 141], which is a drawback for further development as anti-MRSA therapeutics.

The membrane-active retinoids, NH125, and nTZDpa were identified by screening ~82,000 synthetic compounds using a high throughput *Caenorhabditis elegans*-MRSA infection screening assay for compounds that block the ability of MRSA to kill the nematodes [24, 25, 140], 185 "hit" compounds were screened for the additional ability to permeabilize MRSA persisters using a SYTOX Green membrane permeability assay [140]. Another putative membrane-active antimicrobial identified in this screen was the FDA-

approved anthelminthic drug bithionol, which was chosen for additional studies due to its well-established pharmacokinetics, toxicity, and safety profiles [142].

In this chapter, we describe the therapeutic potential of bithionol as an anti-MRSA persister antibiotic agent, and using molecular dynamics simulations, we provide a putative mode of action that explains the ability of bithionol to selectively disrupt bacterial membranes compared to mammalian membranes. Moreover, by simulating a panel of bithionol, retinoids and nTZDpa analogs, we demonstrate the potential of *in silico* simulations to evaluate the selectivity of compounds for bacterial membrane versus mammalian membrane, which could be used for rationally designing high potent membrane-active antimicrobial with high selectivity and overcoming the current obstacle of membrane selectivity issues.

5.2 Simulation model and methodology

All-atom MD simulations based on the GROMACS package [143] were performed to investigate the interactions between nanoagents and a simulated bacterial or mammalian plasma membrane. Automated Topology Builder [144] was employed to generate the topologies and parameters of nanoagents that were compatible with the GROMOS54a7 force field [145]. Specifically, atomic charges of compounds were fitted to quantum mechanical electrostatic potentials at B3LYP/6-31G* level of theory; non-bonded parameters were refined against experimental solvation properties; bonded parameters were assigned using force constants estimated from Hessian (B3LYP/6-31G*) [144]. All of the topologies and parameters can be downloaded freely on the website (https://atb.uq.edu.au/index.py). The plasma membrane of *S. aureus* was represented by a

mixed lipid bilayer composed of 88 neutral-charged DOPC and 40 negatively-charged DOPG lipids (~7:3 ratio) with dimensions of 5.96 nm × 5.96 nm. This mixture of lipids is widely used to mimic anionic Gram-positive bacterial membranes and to investigate the mechanisms of action of membrane-active antimicrobials, such as daptomycin and antimicrobial peptides on *S. aureus* membranes [24, 25, 146-149]. The mammalian plasma membrane was made up of POPC lipids with 30 molar-% cholesterol [150, 151] with dimensions of 5.51 nm × 5.51 nm. The POPC lipid bilayers with different molar percentages of cholesterol (0%, 10%, 20%, and 30%) were also constructed to study the effects of cholesterol on the membrane selectivity of bithionol. The DOPC, DOPG, POPC lipids and cholesterol were modeled with Berger's lipid force field [152], which is an extensively validated all-atom lipid model for membrane-related simulations [17, 23]. Repetitions of simulations for different membrane compositions were performed to verify the robustness of results and mechanisms. Sodium ions were added into the simulation system to neutralize the negative charge of membranes. To visualize membrane attachment and penetration, nanoagents and sodium ions are depicted as large spheres, phospholipids are represented as chains, and bonds in cholesterols are highlighted by thickened tubes. The atoms in nanoagents, phospholipids, cholesterols and sodium ions are colored as follows: hydrogen, white; oxygen, red; nitrogen, blue; sulfur, yellow; chlorine, green; carbon, cyan; phosphorus, orange; sodium, purple. Water molecules are not shown for clarity.

For enhanced computational efficiency, water molecules were represented by a polarization corrected simple point-charge SPC/E model [153]. A geometric combining rule of Lennard-Jones potential was adopted for non-bonded interactions of nanoagents

and its analogs with lipids, ions and water. The fast smooth particle-mesh Ewald [154] was used to calculate the long-rang electrostatic interactions. The system was modeled as an NPT ensemble, with periodic boundary conditions in all directions under constant pressure *P* (1 atm) and constant temperature *T* (300 K). The simulation box had an initial height of 12.3 nm, which was large enough to prevent the membrane and antibiotic molecules from interacting with their periodic images. The time step was fixed at 2 fs. After a 500 ns initial equilibration of solvated lipid systems, nanoagent was introduced into the water phase above the membrane. After 100 ns of re-equilibration, the molecules were released and their interactions with the membrane including attachment, penetration and equilibrium configurations were further simulated for 500 ns. The free energy profiles for the translocations of nanoagents were calculated by steered molecular dynamics [155] umbrella sampling, and the weighted histogram analysis methods [156, 157], with the output giving the transfer energies and energy barriers that describe the feasibility (favorability and rate, respectively) of membrane penetration. The energy profile of penetration is a theoretical representation of an energetic pathway, as nanoagents are translocated into a membrane, with two independent parameters: transfer energy and energy barrier. The transfer energy of penetration, which is defined as the energy conversion from outside solution to the equilibrium state inside membrane, describes the direction of translocation. The negative value of transfer energy that represents the energy decrease for penetration indicates that the embedment of nanoagents inside the membrane is energetically favorable. The energy barrier is calculated as the height of the peak along the pathway relative to the equilibrium state outside the membrane surface. The energy barrier is the least energy the nanoagent must possess to cross over the membrane surface,

which governs the rate of penetration. A lower energy barrier corresponds to a faster and easier penetration. In equilibrium, the probability of a system being in a state with energy E is proportional to $e^{-E/k_{\mathrm{B}}T}$. By using the $k_{\mathrm{B}}T$ as the measurement, the system stability could be explicitly compared at different equilibrium states. GridMAT-MD [158] was used to calculate the thickness of bilayer membrane. With a grid of 20×20, thickness distributions of the bacterial membrane with or without embedment of bithionol were measured by a time average of 50 ns (500 frames). Configurational and thermodynamic analyses, including mass density profile of hydrophobic member interior and deuterium order parameters of lipid acyl chains, were performed to study the effects of the embedment of cholesterol in lipid bilayers.

5.3 Results

Bithionol shows bactericidal activity against both antibiotic-resistant *S. aureus* and *S. aureus* persister cells. Bithionol (Fig. 5.1a) was previously described as an antimicrobial agent with a minimal inhibitory concentration (MIC) of approximately 8 to 15 μg/mL against Gram-positive bacteria including *S. aureus* [159]. We confirmed that bithionol exhibits antimicrobial activity against a variety of Gram-positive pathogens, including vancomycin-resistant *S. aureus* (VRSA) and vancomycin- and daptomycin-resistant Enterococcal strains. In our hands, however, bithionol was more potent than previously reported with MICs of 0.5 to 2 μg/mL, comparable to daptomycin. We also confirmed that bithionol exhibits relatively weak antimicrobial activity against Gram-negative pathogens (MICs of 16 to >64 μg/mL) [160].

In contrast to a previous study that described bithionol as bacteriostatic [161], we

found that bithionol eradicated ~10^7 CFU/mL exponential-phase *S. aureus* strain MW2 within 3 h at 10 μg/mL (10× MIC). The rate of killing was comparable to daptomycin (at 10× MIC) and significantly faster than the killing kinetics of vancomycin (at 10× MIC). Consistent with its bactericidal activity, 10 μg/mL bithionol caused a time-dependent decrease in optical density of *S. aureus* cells comparable to the antiseptic detergent benzyldimethylhexadecylammonium chloride (16-BAC) [160], indicating that bithionol has bacteriolytic activity. Indeed, transmission electron micrographs (TEM) showed that 10× MIC bithionol disrupts MRSA membranes, causing the intracellular formation of mesosome-like structures, abnormal cell divisions, and cell lysis (Fig. 5.1b), which we previously observed when *S. aureus* cells were treated with membrane-active antimicrobials [24].

We also found that bithionol killed stationary-phase MRSA MW2 planktonic and biofilm persisters in a dose-dependent manner, and completely eradicated them at 32 μg/mL (32× MIC) within 2 h and 24 h, respectively (Fig. 5.1c,d). In contrast, MW2 persisters displayed a high level of tolerance to 100× MIC of several conventional antibiotics including daptomycin and linezolid, which were tested for activity against planktonic persisters. Similarly, bithionol killed vancomycin-resistant *S. aureus* (VRSA) strain VRS1 persisters, whereas linezolid and daptomycin exhibited no and nominal activity, respectively (Fig. 5.1e).

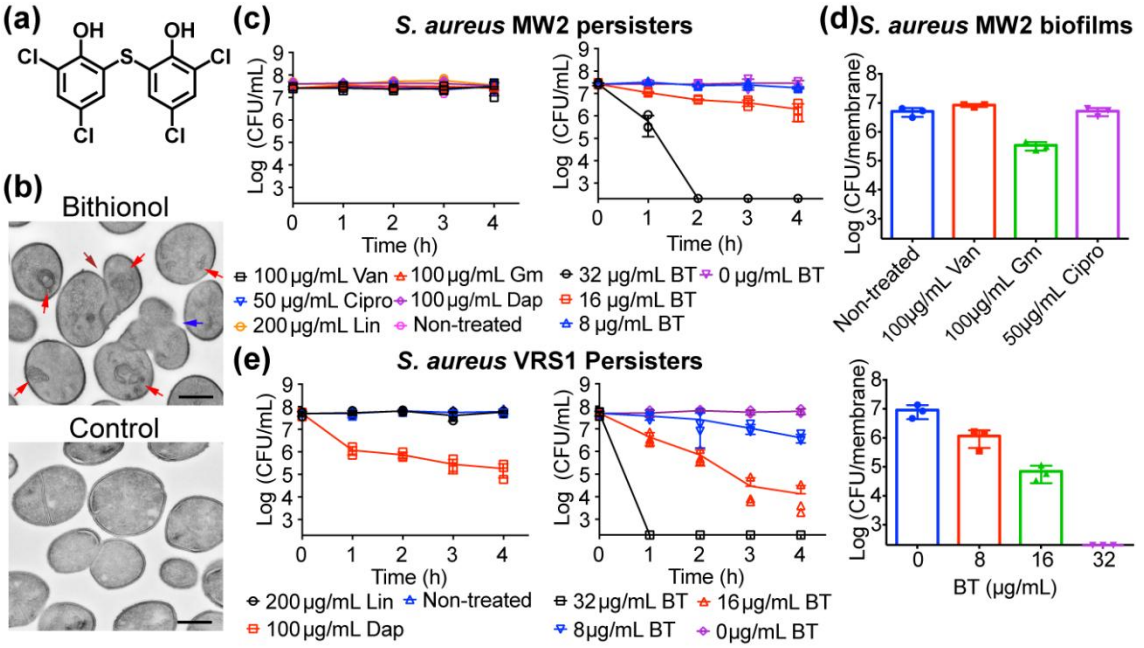

Figure 5.1. Bithionol exhibits bactericidal activity against *S. aureus* persisters. (a) Chemical structures of bithionol. (b) TEM micrographs showing the formation of intracellular mesosome-like structures (red arrows), an abnormal cell division (brown arrow), or cell lysis (blue arrow) in *S. aureus* MW2 treated with 10 × MIC (10 μg/mL) bithionol or 0.1% DMSO (control) for 2 h. Scale bars represent 500 nm. (c, d) Viability of MRSA MW2 stationary-phase (c) or biofilm (d) persister cells treated with 100 × MIC of the conventional antibiotics vancomycin (Van), gentamicin (Gm), ciprofloxacin (Cipro), daptomycin (Dap), linezolid (Lin), or the indicated concentrations of bithionol (BT) for 4 h (c) and 24 h (d), respectively. (e) The viability of *S. aureus* VRS1 persisters treated with 100 × MIC (200 μg/mL) linezolid (Lin), 100 × MIC (100 μg/mL) daptomycin (dap), or the indicated concentrations of bithionol (BT) as a function of time. The data points on the x-axis are below the level of detection (2×10^2 CFU/mL, or 2×10^2 CFU/membrane). Individual data points (n=3 biologically independent samples) are shown; error bars represent means ± s.d.

Bithionol interacts with and disrupts the bacterial mimetic lipid bilayer. We performed all-atom MD simulations of bithionol interacting with simulated bacterial membranes to elucidate a potential mechanism of action. Previously established model of 1,2-dioleoyl-sn-glycero-3-phosphocholine (DOPC)/1,2-dioleoyl-sn-glycero-3-phospho-(1'-rac-glycerol) (DOPG) at a 7:3 ratio [149] was adopted to simulate negatively-charged *S. aureus* membranes. The MD modeling showed that bithionol is initially recruited to the

membrane surface by the binding of polar hydroxyl and chlorine groups to hydrophilic lipid heads (Fig. 5.2a). After several hundred nanoseconds of sustained attachment, bithionol penetrates into the membrane interior, maximizing interactions between nonpolar benzene rings and hydrophobic lipid tails. After penetration, bithionol embeds in the outer leaflet of the lipid bilayer (Fig. 5.2a). The insertion of even a single bithionol molecule causes a substantial local increase in lipid bilayer disorder (Fig. 5.3a,c). These MD simulations demonstrate that the polarity of branch groups and the hydrophobicity of core rings play important roles in membrane attachment and penetration.

We further investigated the effects of bithionol on lipid bilayers using biomembrane-mimicking giant unilamellar vesicles (GUVs) consisting of a single lipid bilayer with a diameter of 10-100 μm. GUVs were constructed using DOPC/DOPG lipids at a 7:3 ratio as in the MD simulations. Lipid aggregates formed on the surfaces of the GUVs exposed to 1 μg/mL bithionol and at 10 μg/mL the GUVs burst (Fig. 5.2c), indicating that bithionol interacts with and disrupts a bacterial mimetic lipid bilayer.

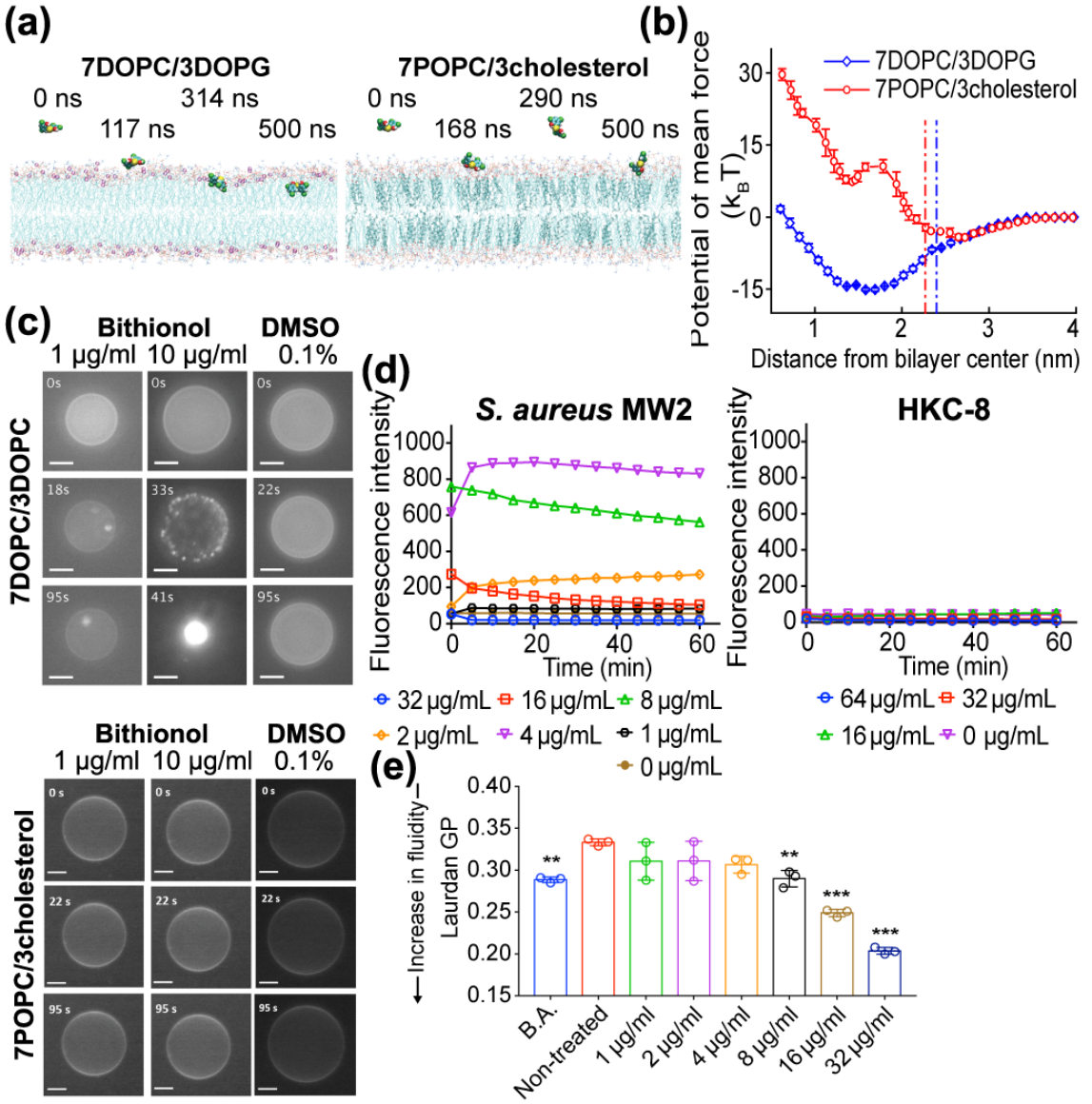

Figure 5.2. Bithionol selectively disrupts bacterial lipid bilayers. (a) Representative configurations of MD simulations of bithionol from left to right: onset, membrane attachment, membrane penetration, and equilibrium interacting with 7DOPC/3DOPG or 7POPC/3cholesterol lipid bilayers. (b) The free energy profiles of bithionol penetrating into the indicated lipid bilayers as a function of the center-of-mass (COM) distance to the bilayer. The dot-dashed blue and red lines mark the surface of bacterial and mammalian membranes, respectively, averaged from the COM locations of phosphate groups in the lipids of the outer leaflets. (c) GUVs consisting of DOPC/DOPG (7:3) or POPC/cholesterol (7:3) labeled with 0.005% Liss Rhod PE were treated with the indicated concentrations of bithionol or 0.1% DMSO (control) and were monitored over time using fluorescence microscopy. Scale bars represent 10 μm. (d) Uptake of SYTOX Green (Ex= 485 nm, Em= 525 nm) by MRSA MW2 persister cells or human renal proximal cells (HKC-8) treated with the indicated concentrations of bithionol. Results are shown as

means; n=3 biologically independent samples. Error bars not shown for clarity. (e) *S. aureus* MW2 membrane fluidity treated with the indicated concentrations of bithionol for 1 h was evaluated based on Laurdan generalized polarization (Laurdan GP). Individual data points (n=3 biologically independent samples) are shown; error bars represent means ± s.d. Statistical differences between control and antibiotic treatment groups were analyzed by one-way ANOVA and post-hoc Dunnett test (**p = 0.01, ***p < 0.0001.)

Bithionol induces rapid membrane permeabilization and an increase in membrane fluidity. Using a SYTOX Green permeability assay, we found that in contrast to daptomycin, bithionol induced dose-dependent membrane permeability in both exponential-phase MRSA MW2 cells and stationary phase MRSA MW2 persisters (Fig. 5.2d). The fluorescence intensity peaked at 4 μg/mL and then decreased at higher concentrations of bithionol (Fig. 5.2d), most likely as a consequence of nucleic acids released form lysed cells [162], consistent with the observation that 10 μg/ml bithionol lyses MRSA persisters (Fig. 5.1b). The dose-dependent effects of bithionol on membrane permeability correlated with its dose-dependent killing kinetics (Figs. 5.1c, 5.2d), suggesting that the bactericidal activity of bithionol results from its membrane-disrupting activity.

Insertion of particular membrane disrupting compounds into lipid bilayers is known to cause dramatic changes in membrane fluidity that disrupts the normal liquid-crystalline phase of the membrane [163-165]. This results in passive permeabilization, loss of membrane protein functions, leakage of cellular components, and bacterial death [166]. We therefore tested whether bithionol alters MRSA MW2 membrane fluidity by utilizing the membrane fluidity-sensitive dye Laurdan [167], which exhibits a fluorescence emission wavelength shift dependent on the amount of adjacent water molecules. Because water molecule penetration into lipid bilayers is in turn determined by lipid packing density and

lipid bilayer fluidity, bacterial membrane fluidity can be quantified using the Laurdan generalized polarization (GP) metric: GP = $(I_{440}-I_{490})/(I_{440}+I_{490})$ ranging from -1 (most fluid and disordered) to +1 (most rigid and ordered) [167]. As shown in Fig. 5.2e, bithionol at concentrations over 8 μg/mL induced a significant decrease in Laurdan GP in *S. aureus* MW2, similar to 50 mM benzyl alcohol (BA), a known membrane fluidizer. These data are consistent with our observation that bithionol concentrations greater than 16 μg/mL exhibited significant killing activity against MRSA MW2 persisters (Fig. 5.1c).

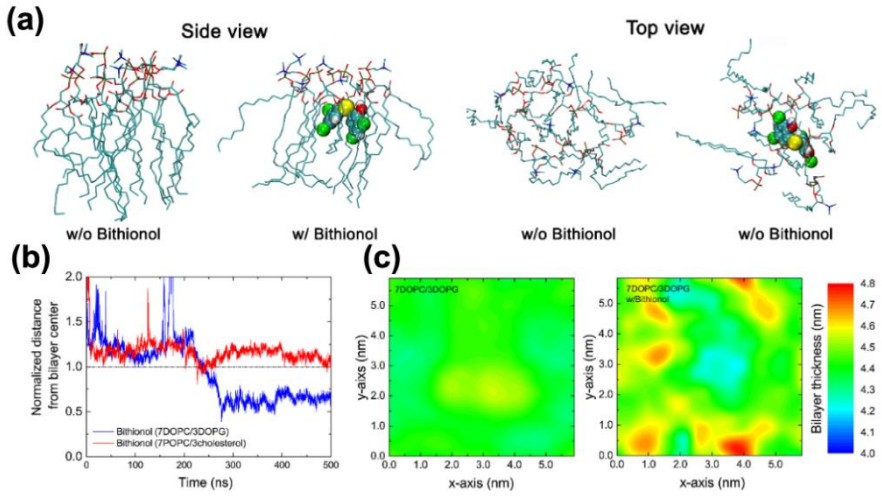

Figure 5.3. (a) Detailed configurations of nearest neighboring lipids around an embedded bithionol molecule. (b) Normalized distances of bithionol from the bilayer centers of the indicated lipid bilayers versus simulation time. The distances from bilayer centers are normalized by half the thickness of the indicated lipid bilayers, respectively. (c) Change in lipid bilayer thickness after one bithionol molecule embeds into the outer leaflet of the bilayer. Bilayer thickness is obtained by time average over 50 ns simulation trajectory at equilibrium.

Bithionol does not penetrate mammalian membranes. We used MD simulations to determine whether bithionol specifically penetrates bacterial compared to mammalian membranes. Mammalian membranes are comprised of phospholipids, sphingolipids, and cholesterol [168], but can be modeled as a simplified bilayer composed of the zwitterionic

lipid 1,2-palmitoyl-oleoyl-sn-glycero-3-phosphocholine (POPC) mixed with cholesterol ranging from 20 to 50 mol % [151, 169]. At a POPC/cholesterol ratio of 7:3, MD simulations showed that bithionol fails to penetrate the simulated mammalian bilayer (Figs. 5.2a,b and 5.3b). Moreover, the energy barrier and transfer energy for bithionol increases with increasing percentages of cholesterol (Fig. 5.4a). These results are consistent with our observation that the presence of cholesterol results in a more ordered alignment of the membrane lipids (Fig. 5.4d) as well as with configurational and thermodynamic analyses [170, 171], which demonstrate that cholesterol condenses the hydrophobic region of the membrane (Fig. 5.4b) and decreases membrane fluidity (Fig. 5.4c).

Consistent with the MD simulations, bithionol did not cause observable effects on GUVs formed with 7POPC/3cholesterol (Fig. 5.2c). Moreover, bithionol exhibited relatively little hemolytic activity against human erythrocytes with an HC_{50} >64 μg/mL [160] and did not induce SYTOX Green membrane permeabilization of HKC-8 human renal proximal cells up to 64 μg/mL (Fig. 5.2d).

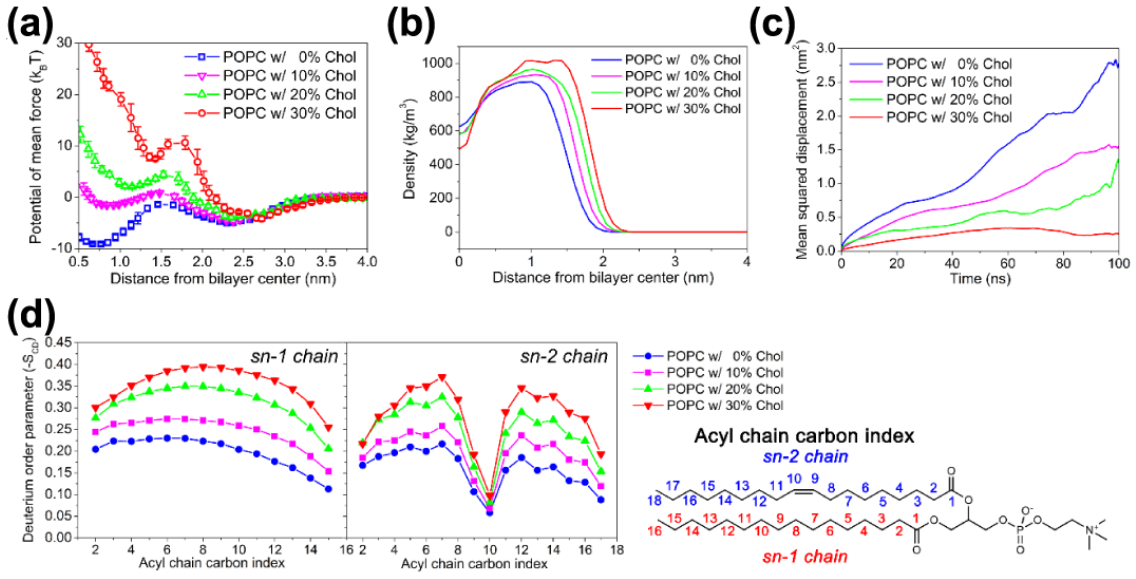

Figure 5.4. The effect of cholesterol in simulated mammalian membranes on bithionol penetration. (a) The free energy profiles of bithionol penetrating into a POPC lipid bilayer with different molar

percentages of cholesterols as a function of the COM distance to the bilayer. (b) Calculated mass density profile of the hydrophobic region (acyl chains) of POPC lipid bilayers containing different molar percentages of cholesterol versus the COM distance to the bilayer. (c) Calculated lateral mean squared displacements (MSD) of POPC lipids over 100 ns simulations at equilibrium for various molar percentages of cholesterol. (d) Calculated deuterium order parameters ($-S_{CD}$) for saturated sn-1 and unsaturated sn-2 acyl chains in POPC lipids with different molar percentages of cholesterols. The deuterium order parameter represents the structural orientation or mobility of lipids in a bilayer, corresponding to the configurational entropy and the physical state (liquid-disordered or solid-ordered phases) of the membrane system. In general, a higher $-S_{CD}$ indicates a higher ordered structure of lipids with decreased membrane fluidity and permeability.

Structure-activity relationships. The MD simulations described above predicted that two key elements for the membrane activity of bithionol are the initial binding to the membrane surface using phenolic hydroxyl groups and membrane perturbation induced by chlorinated benzene (Fig. 5.2a). To further test this proposed mechanism and to obtain additional insights into the effects of functional groups on the potency of bithionol, we conducted structure-activity relationship (SAR) studies using a commercially available bithionol analog, bitin-S, as well as with seven newly synthesized analogs (Table 5.1). The effect of binding affinity on antimicrobial and membrane activity was tested using bitin-S, a sulfoxide derivative of bithionol [172], and the bithionol methoxy analog, BT-OMe (Table 5.1). The polar sulfinyl group of bitin-S provides additional hydrophilic interactions with lipid heads. Bitin-S exhibited decreased antimicrobial activity (MIC 8 μg/mL) and reduced membrane activity (Table 5.1). Reducing polarity by substituting methoxy groups for the two hydroxyl groups (BT-OMe, Table 5.1) resulted in complete nullification of both antimicrobial and membrane activity (Table 5.1), indicating that the phenolic hydroxyl groups are critical for antimicrobial activity.

Table 5.1. Structure-activity relationships for antibiotic activity and membrane activity

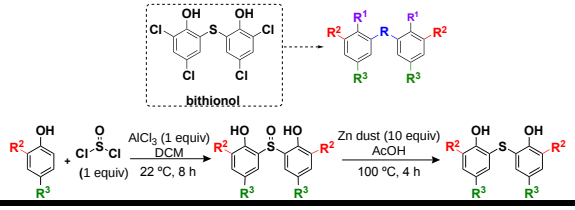

Cmpd	R	R^1	R^2	R^3	MIC	PKC	MP	MFI
Bithionol	S	OH	Cl	Cl	1	32	Yes	Yes
Bitin-S	SO	OH	Cl	Cl	8	>64	Yes	No
BT-OMe	S	OMe	Cl	Cl	>64	>64	No	No
BT-*o*F	S	OH	F	Cl	2	>64	Yes	No
BT-*o*Br	S	OH	Br	Cl	1	32	Yes	Yes
BT-*p*F	S	OH	Cl	F	2	>64	Yes	No
BT-*p*Br	S	OH	Cl	Br	1	32	Yes	Yes
BT-*op*F	S	OH	F	F	8	>64	No	No
BT-*op*Br	S	OH	Br	Br	1	32	Yes	Yes

MIC: minimum inhibitory concentration (μg/ml), PKC: persister killing concentration (μg/ml) required to kill 5 × 10^7 CFU/mL MRSA persister cells below the limit of detection. MP (Membrane permeabilization): determined based on SYTOX Green fluorescence intensity. MFI (Membrane fluidity increase): determined based on Laurdan GP measurement.

To test whether the size and polarization of the inserted molecules can affect the extent of membrane perturbation [24], we substituted alternative halogens for chlorine. Replacement of chlorine with fluorine resulted in reduced membrane and antimicrobial activities as seen with compounds BT-*o*F, BT-*p*F, and BT-o*p*F, whereas substitution with bromine showed similar membrane and antimicrobial activities as bithionol as demonstrated by BT-*o*Br, BT-*p*Br, and BT-*op*Br (Table 5.2). It is likely that the polarity of the C-F bond in the fluoro derivatives may increase the hydrophilicity of the aryl rings, thus decreasing membrane permeability. The bromine derivatives showed increased energy barrier values of 2 – 3 k_BT (Table 5.2), indicating that the larger bromine atoms may cause more membrane perturbation than the smaller chlorine and fluorine atoms, although the bromines may be slightly disadvantageous for initial binding and penetration.

Table 5.2. Characteristic parameters derived from the energy profile of interaction between bithionol or its analogs and the bacterial mimetic lipid bilayer.

Compound	Transfer energy[1] (k_BT)	Energy barrier[2] (k_BT)
Bithionol	-15.44	~0
Bitin-S	-10.51	~0
BT-OMe	6.19	13.52
BT-*o*F	-13.44	~0
BT-*o*Br	-14.76	2.11
BT-*p*F	-7.38	~0
BT-*p*Br	-7.27	2.32
BT-*op*F	-12.94	~0
BT-*op*Br	-10.16	3.07

[1]Transfer energy: the difference between the energies in solution and in the membrane. [2]Energy barrier: the amount of energy required for initial membrane penetration. Transfer energy and energy barrier values were calculated based on MD simulations between a compound and a 7DOPC/3DOPG lipid bilayer.

***In silico* evaluation of membrane selectivity.** We further tested whether membrane selectivity evaluated by MD simulations is consistent with the one determined by cell-based experiments. For compounds to be tested, we chose the membrane active antimicrobials, NH125, CD437, CD437-analog 2, nTZDpa, and nTZDpa-analog 14 that we previously identified [24, 25, 140, 141] because they have different chemical structures and various membrane selectivity (Fig. 5.5). We also added an amphiphilic detergent, benzyldimethylhexadecylammonium chloride (16-BAC) as a positive control, which has the low selectivity index (SI, median hemolytic concentration HC_{50}/MIC) of 12.5 [141]. The free energy profiles of the interaction between these 6 compounds and the bacterial membrane mimetic 7DOPC/3DOPG or the mammalian membrane mimetic 7POPC/3cholesterol lipid bilayers were calculated by all-atom MD simulations. 16-BAC showed lower a free energy profile when interacting with the mammalian than bacterial mimetic membranes (Fig. 5.5), indicating 16-BAC has preference to penetrate mammalian

membrane than bacterial membranes. NH125 and nTZDpa exhibited the similar pattern to 16-BAC, which is consistent with their low selectivity index of 19 and 11.75, respectively (Fig. 5.5). However, CD437 and CD437-analog 2 show lower energy profiles when they interacted with bacterial mimetic membrane compared to mammalian membranes which is consistent with their high SI of >32 (Fig. 5.5). nTZDpa-analog 14 is the most optimized analog among synthesized nTZDpa analogs showing both improved antimicrobial activity and membrane selectivity (Fig. 5.5) [24]. The MD simulations also show that unlike nTZDpa, the penetration of nTZDpa-analog 14 into bacterial membranes is energetically-favorable while its penetration into mammalian membrane is not energetically spontaneous (Fig. 5.5). These results indicate that evaluation of membrane selectivity by MD simulations is strongly consistent with the one by cell-based assays, suggesting MD simulations could be a promising platform to evaluate membrane selectivity of membrane-active agents.

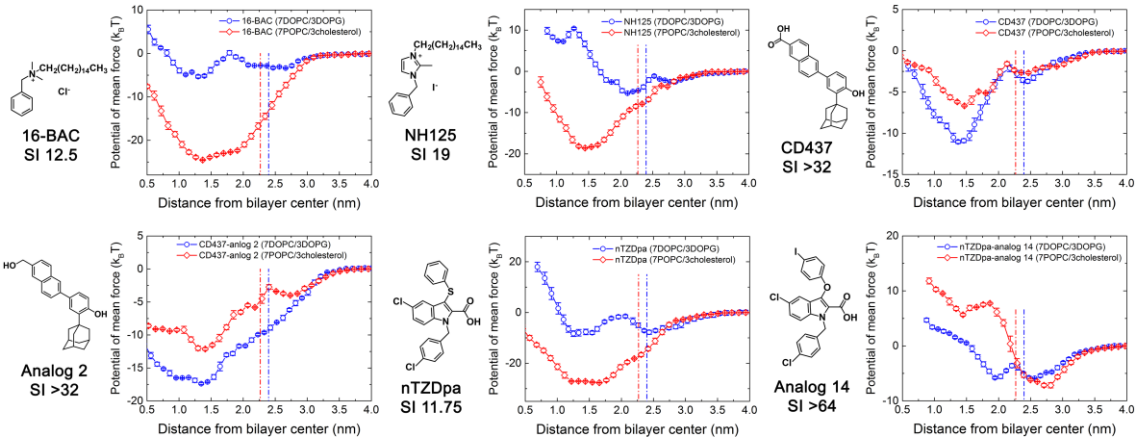

Figure 5.5. The free energy profiles of membrane-active antimicrobials penetrating into the bacterial (blue line) or mammalian (red line) mimetic lipid bilayers as a function of the center-of-mass (COM) distance to the bilayer. SI: selectivity index (HC_{50} against human red blood cells/MIC against *S. aureus* MW2).

5.4 Discussion

Membrane-active agents have attractive properties as antimicrobial agents, including fast killing rates, anti-persister potency, synergism with other antibiotics, and a low probability of resistance selection [136]. Unfortunately, most of these agents also indiscriminately disrupt mammalian membranes. However, bacteria and animals have different membrane lipid compositions, and evolution has taken advantage of these differences as reflected in the production of cationic antimicrobial peptides by animals and plants that specifically target bacterial cells. Gram-positive bacterial membrane lipid bilayers, including those of *S. aureus*, contain approximately 25% anionic phospholipids such as cardiolipin and phosphatidylglycerol. Conversely, mammalian membrane lipid bilayers are composed of zwitterionic (neutral) phospholipids and 20-50% cholesterol [150, 169]. Cationic antimicrobial peptides show a binding preference to negatively-charged bacterial membranes compared to neutrally-charged mammalian membranes. In addition, cholesterol embedded in mammalian membrane lipid bilayers creates a condensing effect that confers membrane rigidity and prevents the penetration of antimicrobial peptides [150].

Consistent with the different compositions of Gram-positive bacterial membranes and mammalian membranes, we found that bithionol penetration into negatively-charged bacterial mimetic lipid bilayers (7DOPC/3DOPG) is energetically favorable, whereas bithionol penetration into cholesterol-rich mammalian mimetic lipid bilayers (7POPC/3cholesterol) is energetically unfavorable (Fig. 5.2a,b). Further, as the proportion of cholesterol increases from 0 to 30%, the penetration of bithionol becomes increasingly unfavorable (Fig. 5.4a), indicating that cholesterol plays a key role in bithionol's membrane selectivity.

Although the biomimetic lipid bilayers used for the MD simulations in this study are simplified and do not reflect all features of complex membrane structures, the simulation model reflect two major factors for the membrane selectivity, such as the presence of negatively charge phospholipids in bacterial membranes and the presence of cholesterol in mammalian membranes. Importantly, the antimicrobial potency and membrane selectivity of various membrane-active agents evaluated by the MD simulations strongly correlate with the ones determined by cell-based experiments [24, 25, 141] (Figs. 5.1c,d, 5.2b, and 5.5). These results demonstrate that the potential and ability of MD modeling to distinguish the antimicrobial potency and membrane selectivity could lead to rationalized design and optimization of membrane-active antibiotics. With the increasing computational capability, the high-effective tool of MD modeling could also be a promising platform for high-throughput drug screening as the *C. elegans* model to accelerate the discovery of a new generation of membrane-active antibiotics.

Most membrane-active antimicrobials have amphipathic structures, including a lipophilic side chain and polar head group [173]. Somewhat surprisingly, bithionol does not share these typical structural characteristics with conventional membrane-active antimicrobials. Instead, MD modeling suggests that the two polarized phenolic hydroxyl groups of bithionol play a major role in the presumed initial binding to phospholipid headgroups via hydrogen bonding. SAR studies showed that a methoxy analog of bithionol nullified bioactivity supporting this proposed mechanism of interaction (Table 5.1-2).

In addition to providing presumed polar interactions with lipid headgroups, the bithionol chlorine moieties also appear to play a key role in lipid bilayer perturbation. Briefly, after attachment, the binding affinity of bithionol is dominated by hydrophobic

interactions between its aromatic rings and the hydrophobic tails of the membrane lipids, which drives the penetration of the chlorinated benzene into the outer leaflet of the lipid bilayer causing lipid bilayer perturbation (Figs. 5.3a,c). Accordingly, the replacement of chlorine with fluorine resulted in a decrease in antimicrobial potency (Table 5.1). Replacement of the chlorines with bromines decreased initial binding to the lipid bilayer (Table 5.2), but increased destabilization of the membrane compared to chlorine and fluorine after penetration. Collectively, the antimicrobial activity of bithionol can be modulated by binding affinity to lipid head groups, penetration depth, and molecule size.

Although daptomycin is regarded to be a membrane-active antibiotic, it does not induce rapid SYTOX Green membrane permeabilization or kill MRSA persisters (Fig. 5.1c), in contrast to bithionol and other membrane-active compounds that we have studied [24, 25, 140, 141]. Importantly, we discovered that bithionol and its analogs and nTZDpa and its analogs that exhibit anti-MRSA persister potency, induce both SYTOX Green membrane permeabilization and an increase in membrane fluidity (Table 5.1). These data are consistent with previous reports which show that insertion of compounds into membrane bilayers can increase membrane disorder and fluidity, which subsequently causes passive membrane permeabilization [163, 164]. Interestingly, we found that the initiation of SYTOX Green membrane permeabilization occurs at a lower concentration of the membrane-active compounds than is required to increase membrane fluidity (Fig. 5.2d,e). Furthermore, some membrane-active agents, such as bitin-S, bithionol fluorine analogs, and nTZDpa-analogs 6 and 11 that induce SYTOX Green membrane permeabilization, do not cause a change in membrane fluidity and do not kill persisters [160]. Bacterial membranes consist of lipid rafts organized into microdomains having

different lipid compositions [174]. Depending on lipid compositions, one domain may be less ordered and more fluid, while another domain may be more ordered and rigid [174]. Because ordered and rigid domains show more resistance to membrane active agents [174], up to a certain threshold concentration, only less ordered domains would be affected by membrane-active compounds, thus making them SYTOX Green permeable. However, this type of localized membrane damage may not be sufficient to cause an overall increase in membrane fluidity. Over the threshold concentration, most membrane domains would be disrupted, and subsequently overall membrane fluidity would increase. It is also possible that some compounds may attack only less ordered and more fluid areas of membranes, which causes SYTOX Green membrane permeability, but not an overall increase in membrane fluidity. In any case, the killing of MRSA persisters is apparently only achieved when the bacterial membrane is sufficiently damaged to show increased membrane fluidity as detected by Laurdan GP.

5.5 Conclusions

In conclusion, we report that the clinically approved anthelmintic bithionol is an effective antimicrobial agent against both multidrug-resistant and -persistent Gram-positive pathogens. Bithionol kills Gram-positive (but not Gram-negative) bacterial cells by disrupting lipid bilayers, while maintaining high selectivity for bacterial compared to mammalian membranes, a consequence of the presence of cholesterol in mammalian membranes. Our analysis reveals the molecular mechanisms for membrane selectivity and we also demonstrate the ability and great potential of *in silico* modeling in aiding the discovery and development of new antibiotics.

Chapter 6

Conclusions and Perspectives

6.1 Concluding remarks

Using multiscale modeling and simulations, we have investigated the packing behaviors of flexible nanomaterials in vesicles and cell membranes. The scientific findings for each chapter are summarized as follows.

In chapter 2, we find that packing of a flexible nanofiber inside a vesicle is governed by the interplay between elastic deformations of the nanofiber and vesicle, and we construct a phase diagram of packing in terms of the normalized nanofiber length and bending stiffness. We observe three distinct types of morphological packing phases (lemon, dumpling, and cherry) in simulations. As the nanofiber length or bending stiffness decreases, the cherry-shaped vesicle tends to transform to an axisymmetric lemon shape or a protruding non-axisymmetric dumpling shape or a non-protruding non-axisymmetric dumpling shape. And increasing pressure difference could cause buckling of the nanofiber within the vesicle.

In chapter 3, our simulations of packing of finite nanorods of four distinct shapes within vesicles show that as the nanorod length increases, the vesicle encapsulating a uniform cylindrical nanorod transforms from an initial sphere to a lemon- or conga drum-like shape with vertical symmetry, and then to a cherry- or bowling pin-like shape with a single long, tubular membrane protrusion and a bulge. Accompanying the vesicle shape

transformation, the axial contact force exerted by the confining vesicle gradually increases to a peak as the nanorod length increases, and then decreases with respect to the nanorod length upon vesicle tubulation. The thicker the nanorod is, the higher the force peak. In the case of a cylindrical nanorod with two widened ends, the axial contact force peak becomes proportional to the size of the nanorod tip and is followed by a sharp, discontinuous drop to a constant upon a discontinuous vesicle tubulation evolving from a conga drum-like shape. For a cone-shaped nanorod, vesicle tubulation occurs at the end of the nanorod with a smaller size. The vesicle encapsulating a screwdriver-shaped nanorod is subjected to two peaks of axial contact force due to the formation of a tubular membrane protrusion enclosing the upper and lower nanorod portions of different diameters.

In chapter 4, MD simulations and theoretical analysis have been performed to explore the packing of flexible sheets in vesicles. We find that the sheet-vesicle size and rigidity ratios govern the packing morphologies of the vesicle-sheet system. Phase diagrams of the packing morphology have been established based on the critical conditions for buckling instability. In comparison to cellular packing of long and stiff one-dimensional materials with tubular membrane protrusions, no membrane protrusion has been observed for a vesicle encapsulating a 2D sheet.

In chapter 5, using all-atom MD simulations, we analyze the free energy profiles of membrane-active antimicrobials penetrating into the bacterial or mammalian mimetic lipid bilayers, and we find that the selectivity of membrane-active agents correlates with their ability to penetrate and embed within different cell membranes. Experiments and simulations show that bithionol kills bacterial cells by disrupting lipid bilayers while maintaining high selectivity for bacterial membranes compared to mammalian membranes,

which is due to the presence of cholesterol in mammalian membranes. We also demonstrate that *in silico* modeling offers great potential in aiding the discovery and development of new membrane-active antimicrobial agents.

6.2 Outlook of future research

It has been shown that a fundamental understanding of cell-nanomaterial interactions is of essential importance to biomedical applications, nanotechnology and drug development. Studies in the current thesis only concern a limited part of this interaction, specifically regarding the packing of nanomaterials with different mechanical and geometrical properties into vesicles and different cell membranes. Knowledge about the interaction modes found in this thesis is a small but necessary step towards understanding specific biological problems. Along the lines of this research, there remain many open questions, a few of which are listed below.

(1) In the study of fiber packing in vesicles, we currently only consider the simplest contact interaction between the nanofiber and vesicle membrane; however, specific nanomaterials will introduce additional interactions, which may lead to varied phenomena and biological implications (i.e., carbon nanotubes cause and silver nanowires [17, 18]). How does the specific interaction influence the packing behavior?

(2) Packing of fibrous nanomaterials in vesicles and vesicular compartments is ubiquitous in biology; for now, we limited our study to a single nanofiber with a length comparable to the size of the vesicles. However, natural cytoskeletal microtubules and actin filaments could be much longer and form bundles or network. How do they pack inside vesicles?

(3) For simplicity, the encapsulated two-dimensional nanomaterials in this thesis are

assumed to have smooth edges; however, previous studies have shown that edge asperities could significantly influence the manner by which membranes interact with nanosheets [26], and it will be worthwhile to include the geometrical effects as well as specific interactions to observe the packing behaviors.

(4) As we demonstrate in chapter 5, bacterial membranes could represent a promising target to develop novel antibiotics; in the meantime, numerous studies have observed that cancer cell membranes usually have quite different lipid compositions (see review [175]). Can we develop or design drugs that selectively target cancer cell membranes?

(5) We investigate nanoagent attachment to and penetration into bacterial mimetic membranes, which are only the first of the steps necessary for nanoagents to disrupt lipid bilayers. Following nanoagent penetration, what intrinsic properties or governing roles will ensure membrane disruption? These are questions that need to be answered for the rational design of novel antibiotics.

(6) Artificial intelligence (AI) has become increasingly popular in solving sophisticated scientific problems that involve multiple physics interactions that are challenging to directly model or require unrealistic computational power. Can AI help accelerate the modeling in chapter 5 and, as a result, help screen, design or optimize synthetic membrane-active agents to combat antibiotic resistance?

Bibliography

[1] Donaldson, K., Aitken, R., Tran, L., Stone, V., Duffin, R., Forrest, G., and Alexander, A. (2006). Carbon nanotubes: A review of their properties in relation to pulmonary toxicology and workplace safety. Toxicol Sci *92*, 5-22.
[2] Kane, A.B., Hurt, R.H., and Gao, H.J. (2018). The asbestos-carbon nanotube analogy: An update. Toxicology and Applied Pharmacology *361*, 68-80.
[3] Zurutuza, A., and Marinelli, C. (2014). Challenges and opportunities in graphene commercialization. Nature Nanotechnology *9*, 730-734.
[4] Novoselov, K.S., Fal'ko, V.I., Colombo, L., Gellert, P.R., Schwab, M.G., and Kim, K. (2012). A roadmap for graphene. Nature *490*, 192-200.
[5] Xu, M.S., Liang, T., Shi, M.M., and Chen, H.Z. (2013). Graphene-Like Two-Dimensional Materials. Chemical reviews *113*, 3766-3798.
[6] Wang, Z., Zhu, W., Qiu, Y., Yi, X., von dem Bussche, A., Kane, A., Gao, H., Koski, K., and Hurt, R. (2016). Biological and environmental interactions of emerging two-dimensional nanomaterials. Chemical Society Reviews *45*, 1750-1780.
[7] Umeda, T., Nakajima, H., and Hotani, H. (1998). Theoretical analysis of shape transformations of liposomes caused by microtubule assembly. Journal of the Physical Society of Japan *67*, 682-688.
[8] Kaneko, T., Itoh, T.J., and Hotani, H. (1998). Morphological transformation of liposomes caused by assembly of encapsulated tubulin and determination of shape by microtubule-associated proteins (MAPs). Journal of Molecular Biology *284*, 1671-1681.
[9] Emsellem, V., Cardoso, O., and Tabeling, P. (1998). Vesicle deformation by microtubules: A phase diagram. Physical Review E *58*, 4807-4810.
[10] Tsai, F.C., and Koenderink, G.H. (2015). Shape control of lipid bilayer membranes by confined actin bundles. Soft Matter *11*, 8834-8847.
[11] Diagouraga, B., Grichine, A., Fertin, A., Wang, J., Khochbin, S., and Sadoul, K. (2014). Motor-driven marginal band coiling promotes cell shape change during platelet activation. J Cell Biol *204*, 177-185.
[12] Liu, A.P., Richmond, D.L., Maibaum, L., Pronk, S., Geissler, P.L., and Fletcher, D.A. (2008). Membrane-induced bundling of actin filaments. Nat Phys *4*, 789-793.
[13] Lim, H.W.G., Huber, G., Torii, Y., Hirata, A., Miller, J., and Sazer, S. (2007). Vesicle-Like Biomechanics Governs Important Aspects of Nuclear Geometry in Fission Yeast. PloS one *2*.
[14] Zheng, L., Schwartz, C., Magidson, V., Khodjakov, A., and Oliferenko, S. (2007). The spindle pole bodies facilitate nuclear envelope division during closed mitosis in fission yeast. Plos Biol *5*, 1530-1542.
[15] Zhu, Q., Zheng, F., Liu, A.P., Qian, J., Fu, C.H., and Lin, Y. (2016). Shape Transformation of the Nuclear Envelope during Closed Mitosis. Biophysical Journal *111*, 2309-2316.
[16] Poland, C.A., Duffin, R., Kinloch, I., Maynard, A., Wallace, W.A., Seaton, A., Stone, V., Brown, S., MacNee, W., and Donaldson, K. (2008). Carbon nanotubes introduced into the abdominal cavity of mice show asbestos-like pathogenicity in a pilot study. Nature nanotechnology *3*, 423.

[17] Zhu, W., von dem Bussche, A., Yi, X., Qiu, Y., Wang, Z., Weston, P., Hurt, R.H., Kane, A.B., and Gao, H. (2016). Nanomechanical mechanism for lipid bilayer damage induced by carbon nanotubes confined in intracellular vesicles. Proceedings of the National Academy of Sciences *113*, 12374-12379.
[18] Lehmann, S.G., Toybou, D., del Real, A.E.P., Arndt, D., Tagmount, A., Viau, M., Safi, M., Pacureanu, A., Cloetens, P., Bohic, S., Salome, M., Castillo-Michel, H., Omana-Sanz, B., Hofmann, A., Vulpe, C., Simonato, J.P., Celle, C., Charlet, L., and Gilbert, B. (2019). Crumpling of silver nanowires by endolysosomes strongly reduces toxicity. Proceedings of the National Academy of Sciences of the United States of America *116*, 14893-14898.
[19] Yue, H., Wei, W., Yue, Z.G., Wang, B., Luo, N.N., Gao, Y.J., Ma, D., Ma, G.H., and Su, Z.G. (2012). The role of the lateral dimension of graphene oxide in the regulation of cellular responses. Biomaterials *33*, 4013-4021.
[20] Hu, W.B., Peng, C., Luo, W.J., Lv, M., Li, X.M., Li, D., Huang, Q., and Fan, C.H. (2010). Graphene-Based Antibacterial Paper. Acs Nano *4*, 4317-4323.
[21] Krishnamoorthy, K., Veerapandian, M., Zhang, L.H., Yun, K., and Kim, S.J. (2012). Antibacterial Efficiency of Graphene Nanosheets against Pathogenic Bacteria via Lipid Peroxidation. J Phys Chem C *116*, 17280-17287.
[22] Liu, S.B., Zeng, T.H., Hofmann, M., Burcombe, E., Wei, J., Jiang, R.R., Kong, J., and Chen, Y. (2011). Antibacterial Activity of Graphite, Graphite Oxide, Graphene Oxide, and Reduced Graphene Oxide: Membrane and Oxidative Stress. Acs Nano *5*, 6971-6980.
[23] Tu, Y.S., Lv, M., Xiu, P., Huynh, T., Zhang, M., Castelli, M., Liu, Z.R., Huang, Q., Fan, C.H., Fang, H.P., and Zhou, R.H. (2013). Destructive extraction of phospholipids from Escherichia coli membranes by graphene nanosheets. Nature Nanotechnology *8*, 594-601.
[24] Kim, W., Steele, A.D., Zhu, W.P., Csatary, E.E., Fricke, N., Dekarske, M.M., Jayamani, E., Pan, W., Kwon, B., Sinitsa, I.F., Rosen, J.L., Conery, A.L., Fuchs, B.B., Vlahovska, P.M., Ausubel, F.M., Gao, H.J., Wuest, W.M., and Mylonakis, E. (2018). Discovery and Optimization of nTZDpa as an Antibiotic Effective Against Bacterial Persisters. Acs Infect Dis *4*, 1540-1545.
[25] Kim, W., Zhu, W.P., Hendricks, G.L., Van Tyne, D., Steele, A.D., Keohane, C.E., Fricke, N., Conery, A.L., Shen, S., Pan, W., Lee, K., Rajamuthiah, R., Fuchs, B.B., Vlahovska, P.M., Wuest, W.M., Gilmore, M.S., Gao, H.J., Ausubel, F.M., and Mylonakis, E. (2018). A new class of synthetic retinoid antibiotics effective against bacterial persisters. Nature *556*, 103-+.
[26] Li, Y., Yuan, H., Von Dem Bussche, A., Creighton, M., Hurt, R.H., Kane, A.B., and Gao, H. (2013). Graphene microsheets enter cells through spontaneous membrane penetration at edge asperities and corner sites. Proceedings of the National Academy of Sciences *110*, 12295-12300.
[27] Akhavan, O., and Ghaderi, E. (2010). Toxicity of Graphene and Graphene Oxide Nanowalls Against Bacteria. Acs Nano *4*, 5731-5736.
[28] Allison, K.R., Brynildsen, M.P., and Collins, J.J. (2011). Metabolite-enabled eradication of bacterial persisters by aminoglycosides. Nature *473*, 216-+.
[29] Conlon, B.P., Nakayasu, E.S., Fleck, L.E., LaFleur, M.D., Isabella, V.M., Coleman, K., Leonard, S.N., Smith, R.D., Adkins, J.N., and Lewis, K. (2013). Activated

ClpP kills persisters and eradicates a chronic biofilm infection. Nature *503*, 365-+.
[30] Davies, J., and Davies, D. (2010). Origins and Evolution of Antibiotic Resistance. Microbiol Mol Biol R *74*, 417-+.
[31] van Meer, G., and de Kroon, A.I.P.M. (2011). Lipid map of the mammalian cell. J Cell Sci *124*, 5-8.
[32] van Meer, G., Voelker, D.R., and Feigenson, G.W. (2008). Membrane lipids: where they are and how they behave. Nat Rev Mol Cell Bio *9*, 112-124.
[33] Roostalu, J., and Surrey, T. (2017). Microtubule nucleation: beyond the template. Nat Rev Mol Cell Bio *18*, 702.
[34] Gardner, M.K., Zanic, M., and Howard, J. (2013). Microtubule catastrophe and rescue. Curr Opin Cell Biol *25*, 14-22.
[35] Pollard, T.D., and Cooper, J.A. (2009). Actin, a central player in cell shape and movement. Science *326*, 1208-1212.
[36] Pinot, M., Chesnel, F., Kubiak, J., Arnal, I., Nedelec, F., and Gueroui, Z. (2009). Effects of confinement on the self-organization of microtubules and motors. Current Biology *19*, 954-960.
[37] Keber, F.C., Loiseau, E., Sanchez, T., DeCamp, S.J., Giomi, L., Bowick, M.J., Marchetti, M.C., Dogic, Z., and Bausch, A.R. (2014). Topology and dynamics of active nematic vesicles. Science *345*, 1135-1139.
[38] Fygenson, D.K., Elbaum, M., Shraiman, B., and Libchaber, A. (1997). Microtubules and vesicles under controlled tension. Physical Review E *55*, 850-859.
[39] Fygenson, D.K., Marko, J.F., and Libchaber, A. (1997). Mechanics of microtubule-based membrane extension. Physical review letters *79*, 4497.
[40] Limozin, L., and Sackmann, E. (2002). Polymorphism of cross-linked actin networks in giant vesicles. Physical review letters *89*, 168103.
[41] Honda, M., Takiguchi, K., Ishikawa, S., and Hotani, H. (1999). Morphogenesis of liposomes encapsulating actin depends on the type of actin-crosslinking. Journal of molecular biology *287*, 293-300.
[42] Mesarec, L., Góźdź, W., Iglič, V.K., Kralj, S., and Iglič, A. (2016). Closed membrane shapes with attached BAR domains subject to external force of actin filaments. Colloids and Surfaces B: Biointerfaces *141*, 132-140.
[43] Góźdź, W. (2005). Influence of spontaneous curvature and microtubules on the conformations of lipid vesicles. The Journal of Physical Chemistry B *109*, 21145-21149.
[44] Cohen, A.E., and Mahadevan, L. (2003). Kinks, rings, and rackets in filamentous structures. Proceedings of the National Academy of Sciences *100*, 12141-12146.
[45] Shi, X., von Dem Bussche, A., Hurt, R.H., Kane, A.B., and Gao, H. (2011). Cell entry of one-dimensional nanomaterials occurs by tip recognition and rotation. Nature nanotechnology *6*, 714.
[46] Yi, X., Shi, X.H., and Gao, H.J. (2014). A Universal Law for Cell Uptake of One-Dimensional Nanomaterials. Nano Letters *14*, 1049-1055.
[47] Cooke, I.R., and Deserno, M. (2005). Solvent-free model for self-assembling fluid bilayer membranes: Stabilization of the fluid phase based on broad attractive tail potentials. J Chem Phys *123*.
[48] Reynwar, B.J., Illya, G., Harmandaris, V.A., Muller, M.M., Kremer, K., and Deserno, M. (2007). Aggregation and vesiculation of membrane proteins by curvature-mediated interactions. Nature *447*, 461-464.

[49] Rawicz, W., Olbrich, K.C., McIntosh, T., Needham, D., and Evans, E. (2000). Effect of chain length and unsaturation on elasticity of lipid bilayers. Biophysical Journal *79*, 328-339.
[50] Evans, E., and Rawicz, W. (1990). Entropy-Driven Tension and Bending Elasticity in Condensed-Fluid Membranes. Physical Review Letters *64*, 2094-2097.
[51] Harmandaris, V.A., and Deserno, M. (2006). A novel method for measuring the bending rigidity of model lipid membranes by simulating tethers. J Chem Phys *125*.
[52] Nose, S. (1984). A Unified Formulation of the Constant Temperature Molecular-Dynamics Methods. J Chem Phys *81*, 511-519.
[53] Hoover, W.G. (1985). Canonical Dynamics - Equilibrium Phase-Space Distributions. Physical Review A *31*, 1695-1697.
[54] Plimpton, S. (1995). Fast parallel algorithms for short-range molecular dynamics. Journal of computational physics *117*, 1-19.
[55] Heinrich, V., Božič, B., Svetina, S., and Žekš, B. (1999). Vesicle deformation by an axial load: from elongated shapes to tethered vesicles. Biophysical journal *76*, 2056-2071.
[56] Powers, T.R., Huber, G., and Goldstein, R.E. (2002). Fluid-membrane tethers: minimal surfaces and elastic boundary layers. Physical Review E *65*, 041901.
[57] Pronk, S., Geissler, P.L., and Fletcher, D.A. (2008). Limits of filopodium stability. Physical review letters *100*, 258102.
[58] Wood, W., and Martin, P. (2002). Structures in focus—filopodia. The international journal of biochemistry & cell biology *34*, 726-730.
[59] Mogilner, A., and Rubinstein, B. (2005). The physics of filopodial protrusion. Biophysical Journal *89*, 782-795.
[60] Atilgan, E., Wirtz, D., and Sun, S.X. (2006). Mechanics and dynamics of actin-driven thin membrane protrusions. Biophysical journal *90*, 65-76.
[61] Gittes, F., Mickey, B., Nettleton, J., and Howard, J. (1993). Flexural rigidity of microtubules and actin filaments measured from thermal fluctuations in shape. The Journal of cell biology *120*, 923-934.
[62] Isambert, H., Venier, P., Maggs, A.C., Fattoum, A., Kassab, R., Pantaloni, D., and Carlier, M.F. (1995). Flexibility of Actin-Filaments Derived from Thermal Fluctuations - Effect of Bound Nucleotide, Phalloidin, and Muscle Regulatory Proteins. Journal of Biological Chemistry *270*, 11437-11444.
[63] Mattila, P.K., and Lappalainen, P. (2008). Filopodia: molecular architecture and cellular functions. Nat Rev Mol Cell Bio *9*, 446.
[64] Ostermeir, K., Alim, K., and Frey, E. (2010). Buckling of stiff polymer rings in weak spherical confinement. Physical Review E *81*.
[65] Fosnaric, M., Iglic, A., Kroll, D.M., and May, S. (2013). Monte Carlo simulations of a polymer confined within a fluid vesicle. Soft Matter *9*, 3976-3984.
[66] Xu, J., Wang, H., Liu, C.C., Yang, Y.M., Chen, T., Wang, Y.W., Wang, F., Liu, X.G., Xing, B.G., and Chen, H.Y. (2010). Mechanical Nanosprings: Induced Coiling and Uncoiling of Ultrathin Au Nanowires. Journal of the American Chemical Society *132*, 11920-11922.
[67] Prashar, A., Bhatia, S., Gigliozzi, D., Martin, T., Duncan, C., Guyard, C., and Terebiznik, M.R. (2013). Filamentous morphology of bacteria delays the timing of phagosome morphogenesis in macrophages. J Cell Biol *203*, 1081-1097.

[68] Miyazaki, M., Chiba, M., Eguchi, H., Ohki, T., and Ishiwata, S. (2015). Cell-sized spherical confinement induces the spontaneous formation of contractile actomyosin rings in vitro. Nat Cell Biol *17*, 480-+.
[69] Machlus, K.R., and Italiano, J.E. (2013). The incredible journey: From megakaryocyte development to platelet formation. J Cell Biol *201*, 785-796.
[70] Daniels, D.R., Marenduzzo, D., and Turner, M.S. (2006). Stall, spiculate, or run away: The fate of fibers growing towards fluctuating membranes. Physical Review Letters *97*.
[71] Meleard, P., Gerbeaud, C., Pott, T., FernandezPuente, L., Bivas, I., Mitov, M.D., Dufourcq, J., and Bothorel, P. (1997). Bending elasticities of model membranes: Influences of temperature and sterol content. Biophysical Journal *72*, 2616-2629.
[72] Zou, G.J., Yi, X., Zhu, W.P., and Gao, H.J. (2018). Packing of flexible nanofibers in vesicles. Extreme Mechanics Letters *19*, 20-26.
[73] Wang, X., Xia, T., Duch, M.C., Ji, Z.X., Zhang, H.Y., Li, R.B., Sun, B.B., Lin, S.J., Meng, H., Liao, Y.P., Wang, M.Y., Song, T.B., Yang, Y., Hersam, M.C., and Nel, A.E. (2012). Pluronic F108 Coating Decreases the Lung Fibrosis Potential of Multiwall Carbon Nanotubes by Reducing Lysosomal Injury. Nano Letters *12*, 3050-3061.
[74] Bozic, B., Svetina, S., and Zeks, B. (1997). Theoretical analysis of the formation of membrane microtubes on axially strained vesicles. Physical Review E *55*, 5834-5842.
[75] Koster, G., Cacciuto, A., Derenyi, I., Frenkel, D., and Dogterom, M. (2005). Force barriers for membrane tube formation. Physical Review Letters *94*.
[76] Lee, H.J., Peterson, E.L., Phillips, R., Klug, W.S., and Wiggins, P.A. (2008). Membrane shape as a reporter for applied forces. Proceedings of the National Academy of Sciences of the United States of America *105*, 19253-19257.
[77] Tian, F.L., Yue, T.T., Dong, W., Yi, X., and Zhang, X.R. (2018). Size-dependent formation of membrane nanotubes: continuum modeling and molecular dynamics simulations. Physical Chemistry Chemical Physics *20*, 3474-3483.
[78] Leduc, C., Campas, O., Zeldovich, K.B., Roux, A., Jolimaitre, P., Bourel-Bonnet, L., Goud, B., Joanny, J.F., Bassereau, P., and Prost, J. (2004). Cooperative extraction of membrane nanotubes by molecular motors. Proceedings of the National Academy of Sciences of the United States of America *101*, 17096-17101.
[79] Leduc, C., Campas, O., Joanny, J.F., Prost, J., and Bassereau, P. (2010). Mechanism of membrane nanotube formation by molecular motors. Bba-Biomembranes *1798*, 1418-1426.
[80] Lipowsky, R. (2013). Spontaneous tubulation of membranes and vesicles reveals membrane tension generated by spontaneous curvature. Faraday Discuss *161*, 305-331.
[81] Wang, C., Xu, C.J., Zeng, H., and Sun, S.H. (2009). Recent Progress in Syntheses and Applications of Dumbbell-like Nanoparticles. Advanced materials *21*, 3045-3052.
[82] Wen, H.Q., Peng, H.Y., Liu, K., Bian, M.H., Xu, Y.J., Dong, L., Yan, X., Xu, W.P., Tao, W., Shen, J.L., Lu, Y., and Qian, H.S. (2017). Sequential Growth of NaYF4:Yb/Er@NaGdF4 Nanodumbbells for Dual-Modality Fluorescence and Magnetic Resonance Imaging. Acs Appl Mater Inter *9*, 9226-9232.
[83] Hou, B.B., Zheng, B., Yang, W.T., Dong, C.H., Wang, H.J., and Chang, J. (2017).

Construction of near infrared light triggered nanodumbbell for cancer photodynamic therapy. J Colloid Interf Sci *494*, 363-372.
[84] Ajima, K., Murakami, T., Mizoguchi, Y., Tsuchida, K., Ichihashi, T., Iijima, S., and Yudasaka, M. (2008). Enhancement of In Vivo Anticancer Effects of Cisplatin by Incorporation Inside Single-Wall Carbon Nanohorns. Acs Nano *2*, 2057-2064.
[85] Zhang, M., Murakami, T., Ajima, K., Tsuchida, K., Sandanayaka, A.S.D., Ito, O., Iijima, S., and Yudasaka, M. (2008). Fabrication of ZnPc/protein nanohorns for double photodynamic and hyperthermic cancer phototherapy. Proceedings of the National Academy of Sciences of the United States of America *105*, 14773-14778.
[86] Miyawaki, J., Yudasaka, M., Azami, T., Kubo, Y., and Iijima, S. (2008). Toxicity of single-walled carbon nanohorns. Acs Nano *2*, 213-226.
[87] Tahara, Y., Nakamura, M., Yang, M., Zhang, M.F., Iijima, S., and Yudasaka, M. (2012). Lysosomal membrane destabilization induced by high accumulation of single-walled carbon nanohorns in murine macrophage RAW 264.7. Biomaterials *33*, 2762-2769.
[88] Yang, M., Zhang, M.F., Tahara, Y., Chechetka, S., Miyako, E., Iijima, S., and Yudasaka, M. (2014). Lysosomal membrane permeabilization: Carbon nanohorn-induced reactive oxygen species generation and toxicity by this neglected mechanism. Toxicology and Applied Pharmacology *280*, 117-126.
[89] Helfrich, W. (1973). Elastic Properties of Lipid Bilayers - Theory and Possible Experiments. Z Naturforsch C *C 28*, 693-703.
[90] Yi, X., Zou, G.J., and Gao, H.J. (2018). Mechanics of cellular packing of nanorods with finite and non-uniform diameters. Nanoscale *10*, 14090-14099.
[91] Yang, Z., Zhang, Y.G., Yang, Y.L.A., Sun, L., Han, D., Li, H., and Wang, C. (2010). Pharmacological and toxicological target organelles and safe use of single-walled carbon nanotubes as drug carriers in treating Alzheimer disease. Nanomed-Nanotechnol *6*, 427-441.
[92] Xue, X., Wang, L.R., Sato, Y., Jiang, Y., Berg, M., Yang, D.S., Nixon, R.A., and Liang, X.J. (2014). Single-Walled Carbon Nanotubes Alleviate Autophagic/Lysosomal Defects in Primary Glia from a Mouse Model of Alzheimer's Disease. Nano Letters *14*, 5110-5117.
[93] Pontes, B., Viana, N.B., Salgado, L.T., Farina, M., Neto, V.M., and Nussenzveig, H.M. (2011). Cell Cytoskeleton and Tether Extraction. Biophysical Journal *101*, 43-52.
[94] Adams, J.C. (2004). Roles of fascin in cell adhesion and motility. Curr Opin Cell Biol *16*, 590-596.
[95] Li, J.J., Han, D., and Zhao, Y.P. (2014). Kinetic behaviour of the cells touching substrate: the interfacial stiffness guides cell spreading. Scientific reports *4*.
[96] Su, Q.P., Du, W.Q., Ji, Q.H., Xue, B.X., Jiang, D., Zhu, Y.Y., Lou, J.Z., Yu, L., and Sun, Y.J. (2016). Vesicle Size Regulates Nanotube Formation in the Cell. Scientific reports *6*.
[97] Derenyi, I., Julicher, F., and Prost, J. (2002). Formation and interaction of membrane tubes. Physical Review Letters *88*.
[98] Castagnetti, S., Bozic, B., and Svetina, S. (2015). Mechanical and molecular basis for the symmetrical division of the fission yeast nuclear envelope. Physical Chemistry Chemical Physics *17*, 15629-15636.
[99] Toya, M., Sato, M., Haselmann, U., Asakawa, K., Brunner, D., Antony, C., and

Toda, T. (2007). gamma-Tubulin complex-mediated anchoring of spindle microtubules to spindle-pole bodies requires Msd1 in fission yeast. Nat Cell Biol *9*, 646-U655.
[100] Reiners, J.J., Caruso, J.A., Mathieu, P., Chelladurai, B., Yin, X.M., and Kessel, D. (2002). Release of cytochrome c and activation of pro-caspase-9 following lysosomal photodamage involves bid cleavage. Cell Death Differ *9*, 934-944.
[101] Mu, Q.X., Su, G.X., Li, L.W., Gilbertson, B.O., Yu, L.H., Zhang, Q., Sun, Y.P., and Yan, B. (2012). Size-Dependent Cell Uptake of Protein-Coated Graphene Oxide Nanosheets. Acs Appl Mater Inter *4*, 2259-2266.
[102] Titov, A.V., Kral, P., and Pearson, R. (2010). Sandwiched Graphene-Membrane Superstructures. Acs Nano *4*, 229-234.
[103] Wang, J.L., Wei, Y.J., Shi, X.H., and Gao, H.J. (2013). Cellular entry of graphene nanosheets: the role of thickness, oxidation and surface adsorption. Rsc Advances *3*, 15776-15782.
[104] Guo, R.H., Mao, J., and Yan, L.T. (2013). Computer simulation of cell entry of graphene nanosheet. Biomaterials *34*, 4296-4301.
[105] Yi, X., and Gao, H.J. (2015). Cell interaction with graphene microsheets: near-orthogonal cutting versus parallel attachment. Nanoscale *7*, 5457-5467.
[106] Stern, S.T., Adiseshaiah, P.P., and Crist, R.M. (2012). Autophagy and lysosomal dysfunction as emerging mechanisms of nanomaterial toxicity. Part Fibre Toxicol *9*.
[107] Chu, Z.Q., Zhang, S.L., Zhang, B.K., Zhang, C.Y., Fang, C.Y., Rehor, I., Cigler, P., Chang, H.C., Lin, G., Liu, R.B., and Li, Q. (2014). Unambiguous observation of shape effects on cellular fate of nanoparticles. Scientific reports *4*.
[108] Creighton, M.A., Zhu, W.P., van Krieken, F., Petteruti, R.A., Gao, H.J., and Hurt, R.H. (2016). Three-Dimensional Graphene-Based Microbarriers for Controlling Release and Reactivity in Colloidal Liquid Phases. Acs Nano *10*, 2268-2276.
[109] Jiang, H.Y., Huber, G., Pelcovits, R.A., and Powers, T.R. (2007). Vesicle shape, molecular tilt, and the suppression of necks. Physical Review E *76*.
[110] Seifert, U., Berndl, K., and Lipowsky, R. (1991). Shape Transformations of Vesicles - Phase-Diagram for Spontaneous-Curvature and Bilayer-Coupling Models. Physical Review A *44*, 1182-1202.
[111] Cerda, E., Chaieb, S., Melo, F., and Mahadevan, L. (1999). Conical dislocations in crumpling. Nature *401*, 46-49.
[112] Cerda, E., and Mahadevan, L. (1998). Conical surfaces and crescent singularities in crumpled sheets. Physical Review Letters *80*, 2358-2361.
[113] Cerda, E., and Mahadevan, L. (2005). Confined developable elastic surfaces: cylinders, cones and the Elastica. P Roy Soc a-Math Phy *461*, 671-700.
[114] Venkataramani, S.C., Witten, T.A., Kramer, E.M., and Geroch, R.P. (2000). Limitations on the smooth confinement of an unstretchable manifold. J Math Phys *41*, 5107-5128.
[115] Freund, L.B. (2000). Substrate curvature due to thin film mismatch strain in the nonlinear deformation range. Journal of the Mechanics and Physics of Solids *48*, 1159-1174.
[116] Witten, T.A. (2007). Stress focusing in elastic sheets. Reviews of Modern Physics *79*, 643-675.
[117] Stavsky, Y., and Friedland, S. (1971). Buckling of Composite Circular Plates under Radial Compression. Acta Mech *11*, 87-+.

[118] Seifert, U. (1991). Adhesion of Vesicles in 2 Dimensions. Physical Review A *43*, 6803-6814.
[119] Vassilev, V.M., Djondjorov, P.A., and Mladenov, I.M. (2008). Cylindrical equilibrium shapes of fluid membranes. J Phys a-Math Theor *41*.
[120] Muller, M.M., Deserno, M., and Guven, J. (2007). Balancing torques in membrane-mediated interactions: Exact results and numerical illustrations. Physical Review E *76*.
[121] Zhongcan, O.Y., and Helfrich, W. (1989). Bending Energy of Vesicle Membranes - General Expressions for the 1st, 2nd, and 3rd Variation of the Shape Energy and Applications to Spheres and Cylinders. Physical Review A *39*, 5280-5288.
[122] Arreaga, G., Capovilla, R., Chryssomalakos, C., and Guven, J. (2002). Area-constrained planar elastica. Physical Review E *65*.
[123] Lautrup, B. (2011). Physics of continuous matter: exotic and everyday phenomena in the macroscopic world (CRC press).
[124] Tang, H.Y., Ye, H.F., Zhang, H.W., and Zheng, Y.G. (2015). Wrapping of nanoparticles by the cell membrane: the role of interactions between the nanoparticles. Soft Matter *11*, 8674-8683.
[125] Gracia, R.S., Bezlyepkina, N., Knorr, R.L., Lipowsky, R., and Dimova, R. (2010). Effect of cholesterol on the rigidity of saturated and unsaturated membranes: fluctuation and electrodeformation analysis of giant vesicles. Soft Matter *6*, 1472-1482.
[126] Daum, G., and Vance, J.E. (1997). Import of lipids into mitochondria. Prog Lipid Res *36*, 103-130.
[127] Kudin, K.N., Scuseria, G.E., and Yakobson, B.I. (2001). C2F, BN, and C nanoshell elasticity from ab initio computations. Physical Review B *64*.
[128] Jiang, J.W., Qi, Z.N., Park, H.S., and Rabczuk, T. (2013). Elastic bending modulus of single-layer molybdenum disulfide (MoS2): finite thickness effect. Nanotechnology *24*.
[129] Cao, C.H., Daly, M., Singh, C.V., Sun, Y., and Filleter, T. (2015). High strength measurement of monolayer graphene oxide. Carbon *81*, 497-504.
[130] Ewers, H., Romer, W., Smith, A.E., Bacia, K., Dmitrieff, S., Chai, W.G., Mancini, R., Kartenbeck, J., Chambon, V., Berland, L., Oppenheim, A., Schwarzmann, G., Feizi, T., Schwille, P., Sens, P., Helenius, A., and Johannes, L. (2010). GM1 structure determines SV40-induced membrane invagination and infection. Nat Cell Biol *12*, 11-U36.
[131] Saric, A., and Cacciuto, A. (2012). Mechanism of Membrane Tube Formation Induced by Adhesive Nanocomponents. Physical Review Letters *109*.
[132] Mao, J., Chen, P.Y., Liang, J.S., Guo, R.H., and Yan, L.T. (2016). Receptor-Mediated Endocytosis of Two-Dimensional Nanomaterials Undergoes Flat Vesiculation and Occurs by Revolution and Self-Rotation. Acs Nano *10*, 1493-1502.
[133] Lee, A.S., de Lencastre, H., Garau, J., Kluytmans, J., Malhotra-Kumar, S., Peschel, A., and Harbarth, S. (2018). Methicillin-resistant Staphylococcus aureus. Nat Rev Dis Primers *4*.
[134] Lewis, K. (2010). Persister Cells. Annu Rev Microbiol *64*, 357-372.
[135] Conlon, B.P., Rowe, S.E., Gandt, A.B., Nuxoll, A.S., Donegan, N.P., Zalis, E.A., Clair, G., Adkins, J.N., Cheung, A.L., and Lewis, K. (2016). Persister formation in Staphylococcus aureus is associated with ATP depletion. Nat Microbiol *1*.

[136] Hurdle, J.G., O'Neill, A.J., Chopra, I., and Lee, R.E. (2011). Targeting bacterial membrane function: an underexploited mechanism for treating persistent infections. Nature Reviews Microbiology *9*, 62-75.
[137] Miller, W.R., Bayer, A.S., and Arias, C.A. (2016). Mechanism of Action and Resistance to Daptomycin in Staphylococcus aureus and Enterococci. Csh Perspect Med *6*.
[138] Sharma, B., Brown, A.V., Matluck, N.E., Hu, L.T., and Lewis, K. (2015). Borrelia burgdorferi, the Causative Agent of Lyme Disease, Forms Drug-Tolerant Persister Cells. Antimicrob Agents Ch *59*, 4616-4624.
[139] Sahukhal, G.S., Pandey, S., and Elasri, M.O. (2017). msaABCR operon is involved in persister cell formation in Staphylococcus aureus. Bmc Microbiol *17*.
[140] Kim, W., Conery, A.L., Rajamuthiah, R., Fuchs, B.B., Ausubel, F.M., and Mylonakis, E. (2015). Identification of an Antimicrobial Agent Effective against Methicillin-Resistant Staphylococcus aureus Persisters Using a Fluorescence-Based Screening Strategy. PloS one *10*.
[141] Kim, W., Fricke, N., Conery, A.L., Fuchs, B.B., Rajamuthiah, R., Jayamani, E., Vlahovska, P.M., Ausubel, F.M., and Mylonakis, E. (2016). NH125 kills methicillin-resistant Staphylococcus aureus persisters by lipid bilayer disruption. Future Med Chem *8*, 257-269.
[142] Keiser, J., and Utzinger, J. (2007). Food-borne trematodiasis: current chemotherapy and advances with artemisinins and synthetic trioxolanes. Trends in Parasitology *23*, 555-562.
[143] Hess, B., Kutzner, C., van der Spoel, D., and Lindahl, E. (2008). GROMACS 4: Algorithms for highly efficient, load-balanced, and scalable molecular simulation. Journal of chemical theory and computation *4*, 435-447.
[144] Malde, A.K., Zuo, L., Breeze, M., Stroet, M., Poger, D., Nair, P.C., Oostenbrink, C., and Mark, A.E. (2011). An Automated Force Field Topology Builder (ATB) and Repository: Version 1.0. Journal of chemical theory and computation *7*, 4026-4037.
[145] Schmid, N., Eichenberger, A.P., Choutko, A., Riniker, S., Winger, M., Mark, A.E., and van Gunsteren, W.F. (2011). Definition and testing of the GROMOS force-field versions 54A7 and 54B7. Eur Biophys J Biophy *40*, 843-856.
[146] Joshi, S., Dewangan, R.P., Yar, M.S., Rawat, D.S., and Pasha, S. (2015). N-terminal aromatic tag induced self assembly of tryptophan-arginine rich ultra short sequences and their potent antibacterial activity. Rsc Advances *5*, 68610-68620.
[147] Lee, M.T., Sun, T.L., Hung, W.C., and Huang, H.W. (2013). Process of inducing pores in membranes by melittin. Proceedings of the National Academy of Sciences of the United States of America *110*, 14243-14248.
[148] Ganewatta, M.S., Chen, Y.P., Wang, J.F., Zhou, J.H., Ebalunode, J., Nagarkatti, M., Decho, A.W., and Tang, C.B. (2014). Bio-inspired resin acid-derived materials as anti-bacterial resistance agents with unexpected activities. Chem Sci *5*, 2011-2016.
[149] Chen, Y.F., Sun, T.L., Sun, Y., and Huang, H.W. (2014). Interaction of Daptomycin with Lipid Bilayers: A Lipid Extracting Effect. Biochemistry-Us *53*, 5384-5392.
[150] Brender, J.R., McHenry, A.J., and Ramamoorthy, A. (2012). Does cholesterol play a role in the bacterial selectivity of antimicrobial peptides? Frontiers in immunology *3*.

[151] Hong, C., Tieleman, D.P., and Wang, Y. (2014). Microsecond Molecular Dynamics Simulations of Lipid Mixing. Langmuir *30*, 11993-12001.
[152] Berger, O., Edholm, O., and Jahnig, F. (1997). Molecular dynamics simulations of a fluid bilayer of dipalmitoylphosphatidylcholine at full hydration, constant pressure, and constant temperature. Biophysical Journal *72*, 2002-2013.
[153] Berendsen, H.J.C., Grigera, J.R., and Straatsma, T.P. (1987). The Missing Term in Effective Pair Potentials. J Phys Chem-Us *91*, 6269-6271.
[154] Essmann, U., Perera, L., Berkowitz, M.L., Darden, T., Lee, H., and Pedersen, L.G. (1995). A Smooth Particle Mesh Ewald Method. J Chem Phys *103*, 8577-8593.
[155] Isralewitz, B., Gao, M., and Schulten, K. (2001). Steered molecular dynamics and mechanical functions of proteins. Curr Opin Struc Biol *11*, 224-230.
[156] Hub, J.S., de Groot, B.L., and van der Spoel, D. (2010). g_wham-A Free Weighted Histogram Analysis Implementation Including Robust Error and Autocorrelation Estimates. Journal of chemical theory and computation *6*, 3713-3720.
[157] Kumar, S., Bouzida, D., Swendsen, R.H., Kollman, P.A., and Rosenberg, J.M. (1992). The Weighted Histogram Analysis Method for Free-Energy Calculations on Biomolecules .1. The Method. Journal of Computational Chemistry *13*, 1011-1021.
[158] Allen, W.J., Lemkul, J.A., and Bevan, D.R. (2009). GridMAT-MD: A Grid-Based Membrane Analysis Tool for Use With Molecular Dynamics. Journal of Computational Chemistry *30*, 1952-1958.
[159] Barr, F.S., Collins, G.F., and Wyatt, L.G. (1965). Potentiation of Antimicrobial Activity of Bithionol. J Pharm Sci-Us *54*, 801-&.
[160] Kim, W., Zou, G., Hari, T.P., Wilt, I.K., Zhu, W., Galle, N., Faizi, H.A., Hendricks, G.L., Tori, K., and Pan, W. (2019). A selective membrane-targeting repurposed antibiotic with activity against persistent methicillin-resistant Staphylococcus aureus. Proceedings of the National Academy of Sciences, 201904700.
[161] Erlandson, A.L., and Lawrence, C.A. (1953). Inactivating Medium for Hexachlorophene (G-11) Types of Compounds and Some Substituted Phenolic Disinfectants. Science *118*, 274-276.
[162] Roth, B.L., Poot, M., Yue, S.T., and Millard, P.J. (1997). Bacterial viability and antibiotic susceptibility testing with SYTOX Green nucleic acid stain. Appl Environ Microb *63*, 2421-2431.
[163] Cartron, M.L., England, S.R., Chiriac, A.I., Josten, M., Turner, R., Rauter, Y., Hurd, A., Sahl, H.G., Jones, S., and Foster, S.J. (2014). Bactericidal Activity of the Human Skin Fatty Acid cis-6-Hexadecanoic Acid on Staphylococcus aureus. Antimicrob Agents Ch *58*, 3599-3609.
[164] Wu, Y.P., Bai, J.R., Zhong, K., Huang, Y.N., Qi, H.Y., Jiang, Y., and Gao, H. (2016). Antibacterial Activity and Membrane-Disruptive Mechanism of 3-p-trans-Coumaroyl-2-hydroxyquinic Acid, a Novel Phenolic Compound from Pine Needles of Cedrus deodara, against Staphylococcus aureus. Molecules *21*.
[165] Saeloh, D., Tipmanee, V., Jim, K.K., Dekker, M.P., Bitter, W., Voravuthikunchai, S.P., Wenzel, M., and Hamoen, L.W. (2018). The novel antibiotic rhodomyrtone traps membrane proteins in vesicles with increased fluidity. Plos Pathog *14*.
[166] Epand, R.M., Walker, C., Epand, R.F., and Magarvey, N.A. (2016). Molecular mechanisms of membrane targeting antibiotics. Bba-Biomembranes *1858*, 980-987.
[167] Parasassi, T., and Gratton, E. (1995). Membrane lipid domains and dynamics as

detected by Laurdan fluorescence. Journal of Fluorescence *5*, 59-69.
[168] Harayama, T., and Riezman, H. (2018). Understanding the diversity of membrane lipid composition. Nat Rev Mol Cell Bio *19*, 281-296.
[169] Deleu, M., Crowet, J.M., Nasir, M.N., and Lins, L. (2014). Complementary biophysical tools to investigate lipid specificity in the interaction between bioactive molecules and the plasma membrane: A review. Bba-Biomembranes *1838*, 3171-3190.
[170] de Meyer, F., and Smit, B. (2009). Effect of cholesterol on the structure of a phospholipid bilayer. Proceedings of the National Academy of Sciences of the United States of America *106*, 3654-3658.
[171] Rog, T., Pasenkiewicz-Gierula, M., Vattulainen, I., and Karttunen, M. (2009). Ordering effects of cholesterol and its analogues. Bba-Biomembranes *1788*, 97-121.
[172] Meshi, T., Yoshikawa, M., and Sato, Y. (1970). Metabolic Fate of Bis(3,5-Dichloro-2-Hydroxyphenyl)-Sulfoxide (Bithionol Sulfoxide). Biochem Pharmacol *19*, 1351-+.
[173] Van Bambeke, F., Mingeot-Leclercq, M.P., Struelens, M.J., and Tulkens, P.M. (2008). The bacterial envelope as a target for novel anti-MRSA antibiotics. Trends Pharmacol Sci *29*, 124-134.
[174] Bramkamp, M., and Lopez, D. (2015). Exploring the Existence of Lipid Rafts in Bacteria. Microbiol Mol Biol R *79*, 81-100.
[175] Perrotti, F., Rosa, C., Cicalini, I., Sacchetta, P., Del Boccio, P., Genovesi, D., and Pieragostino, D. (2016). Advances in Lipidomics for Cancer Biomarkers Discovery. International journal of molecular sciences *17*.